



UNIVERSITÀ DEGLI STUDI DI BARI ALDO MORO

DIPARTIMENTO INTERATENEO DI FISICA "M. MERLIN"

Dottorato di ricerca in FISICA – Ciclo XXXI

Settore Scientifico Disciplinare: FIS/01

Laser micromachining with bursts of ultrashort pulses

Dottorando:

Giuseppe Giannuzzi

Supervisori:

Dott. Antonio Ancona

Prof. Vincenzo Spagnolo

Coordinatore:

Ch.mo Prof. Giuseppe Iaselli

ESAME FINALE 2018

CONTENTS

Introduction.....	- 1 -
Chapter 1	
Laser ablation of metals with ultrashort pulses	- 4 -
1.1 Ultrafast laser interaction with matter	- 4 -
1.2 Two temperature model – TTM.....	- 7 -
1.3 Ablation threshold fluence.....	- 10 -
1.4 Incubation effect	- 11 -
Chapter 2	
Laser ablation with multiple laser pulses	- 15 -
2.1 How to generate bursts of pulses	- 15 -
2.1.1 Burst generation by pulse picking	- 15 -
2.1.2 Burst generation by splitting laser pulses.....	- 16 -
2.2 Laser ablation with double pulses.....	- 18 -
2.3 Laser ablation with bursts of pulses.....	- 24 -
Chapter 3	
Laser induced periodic surface structure	- 32 -
3.1 LIPSS classification.....	- 32 -
3.2 Parameters that influence the LIPSS formation.....	- 34 -
3.2.1 Laser wavelength, λ	- 34 -
3.2.2 Angle of incidence, ϑ	- 35 -
3.2.3 Fluence, F	- 36 -
3.2.4 Number of pulses and/or number of scans, N	- 38 -
3.2.5 Polarization, P	- 41 -
3.2.6 Interpulse time delay, Δt	- 43 -
3.3 Mechanisms of LIPSS formation.....	- 45 -
3.3.1 Interference model.....	- 46 -
3.3.2 Self-organization model	- 47 -
3.4 2D – LIPSS	- 49 -

Chapter 4

TTM with burst of pulses	- 55 -
4.1 Numerical model.....	- 55 -
4.2 Numerical simulations	- 57 -

Chapter 5

Experimental setup and methods	- 62 -
5.1 Laser source	- 62 -
5.1.1 Active Fiber System Sci-Series	- 62 -
5.1.2 Pharos laser.....	- 63 -
5.1.3 Selection of laser pulses	- 64 -
5.2 Burst generator.....	- 65 -
5.2.1 Characterization of the burst generator	- 68 -
5.3 Materials and laser processes set-up.....	- 72 -
5.3.1 Laser ablation threshold	- 73 -
5.3.2 Laser surface texturing	- 73 -
5.3.3 Laser ablation removal rate	- 75 -
5.4 Post-processing analysis equipment	- 75 -
5.4.1 Nikon Eclipse ME600	- 75 -
5.4.2 SEM Zeiss Sigma	- 76 -
5.4.3 Optical profilometer	- 76 -
5.4.4 AFM	- 76 -
5.4.5 XPS.....	- 77 -
5.4.6 Contact Angles measurements	- 77 -

Chapter 6

Influence of burst features on ablation	- 79 -
6.1 Ablation threshold fluence with bursts of pulses.....	- 79 -
6.2 Incubation with bursts.....	- 83 -
6.3 Ablation removal rate with bursts.....	- 86 -

Chapter 7

Influence of burst features on LIPSS.....	- 91 -
7.1 1D LIPSS	- 91 -

7.2	2D-LIPSS	- 100 -
7.3	Wettability.....	- 110 -
7.3.1	WCA: static and dynamic measurements.....	- 113 -
7.3.2	Aging: from hydrophilicity to super-hydrophobicity.....	- 114 -
	Conclusions.....	- 118 -
	Bibliography	- 122 -
	Publications and conferences attendance.....	- 135 -
	Acknowledgements.....	- 137 -

Introduction

Ultrafast lasers, which are pulsed lasers with pulse duration from femtosecond (fs) to picosecond (ps), are playing an increasingly important role in many industrial manufacturing processes. In fact, these lasers enable high-quality material processing for many different materials, achieving manufacturing precision up to the sub-micrometer scale, although at low ablation removal rates.

Due to the industrial demand for high throughput laser process, over the past decades, major efforts have been addressed to the development of ultrafast laser sources with increasing average powers and repetition rates. Nowadays, industrial ultrashort pulsed lasers are commercially available with average powers in the range of 100 W, pulse energies up to 400 μ J and repetition rates up to several MHz [1]. In addition, ultrafast laser sources with average powers of more than 1 kW and/or pulse energies up to the Joule level have been demonstrated on a laboratory scale [2,3].

The increase in laser average power and repetition rate of the ultrafast laser brought to improved throughput and industrial productivity together with the occurrence of some problems. In fact, the expected advantages in terms of higher quality and efficiency were counterbalanced by other drawbacks such as heat accumulation. The latter occurs because pulse after pulse, fractions of laser energy released onto the target in the form of heat lead to irreversible thermal damage, such as cracks or melting, which worsen the quality and precision of the manufacturing process.

Therefore, to overcome the issues related to heat accumulation, some solutions have been proposed to better tailor the heat input onto the material either spatially, through high-speed beam handling technologies or Spatial Light Modulators (SLM), or in the time domain by employing the so-called Burst Mode (BM) processing. The latter consists in using sequences (or bursts) of several ultrashort laser pulses with inter-pulse time delay shorter than 1 μ s [4]. The most interesting studies conducted on BM processing with inter-pulse time delay on the nanosecond scale showed that under some experimental conditions, bursts improved the heat-related issues [5–8].

Nevertheless, the BM processing with inter-pulse time delay on picosecond scale has not been deeply investigated, yet. The research interest in using delays on the ps timescale is justified by the fact that during this timeframe of the laser–matter interaction process, the irradiated material is still far from equilibrium. In other words, the subsequent pulses of the burst interact with a material that has been “excited” by the first pulse and is still in a transient

state, which could in principle give rise to novel and unknown process dynamics. For this reason, it is worth investigating BM processing in the picosecond time domain which has been, actually, the aim of the present PhD work.

In this thesis, three different key studies on BM processing are presented, devoted to the investigation of the burst features influence on the ablation threshold fluence, removal rate and surface texturing.

Prior to the experimental investigation, numerical simulations solving the TTM equations have been performed with single pulses (pointed as normal pulse mode – NPM) and BM aiming to predict the temporal and spatial evolution of the electron and lattice temperature during irradiation of steel targets with a burst of ultrashort pulses.

Throughout the first experiments, the influence of the burst features, i.e. number of pulses in the burst and their time delay, on the ablation threshold fluence has been investigated. This research has involved also the study of incubation, which is a well-known effect observed in NPM processing that is responsible for a reduction of the threshold fluence during multi-pulse laser irradiation. Reduction of the threshold fluence is interesting not only from a scientific point of view but it has also relevant implications in industrial applications since it affects the lifetime of the beam steering optics, which represent a severe problem for exploitation of BM processing or laser sources in general working at extremely high repetition rates.

An investigation on the ablation removal rate follows, which compares results of laser milling with NPM and BM under similar experimental conditions. In BM processing, the influence of the number of pulses in the burst and their time delay on the removal rate has been examined.

As already mentioned, these investigations are relevant to assess the bursts (with picosecond delays) performance on the threshold fluence and removal rate, because most experimental data available on BM processing are limited to the case of bursts of pulses with intra-burst delays in the nanosecond range. The last part of the thesis concerns the surface texturing with bursts of variable numbers of femtosecond laser pulses, time delay between pulses and different polarization states. In particular, the morphology of the laser-induced surface structures produced by different BM processing conditions has been investigated. The interest has been focused on periodic structures known as LIPSS (laser-induced periodic surface structures), highlighting similarities and differences between that generated in BM and NPM. The main implication of such study is the functionalization of surfaces in relation to their frictional, optical and wettability properties. Before performing all these studies, a robust and compact burst generator based on an array of birefringent crystals has been designed and developed. This setup was

flexibly employed with two different laser sources and allowed generating bursts of tuneable number of femtosecond pulses with variable delay in the picoseconds range.

This thesis is organized in seven chapters:

Chapter 1 gives a short insight on laser energy absorption processes, which initiate laser ablation. The ablation threshold fluence is introduced together with the incubation effect. The two-temperature model (TTM) is also presented.

Chapter 2 introduces the bursts of ultrashort laser pulses and the ways of generating them. Moreover, a short review on burst literature is reported, useful for a final comparison with the thesis' results.

Chapter 3 is devoted to the description of the LIPSS and their classification in LSFL and HSFL according to the spatial period or in 1D and 2D-LIPSS based on the number of periodic directions. In detail, the factors influencing the morphology of these structures, such as the laser fluence and wavelength, the angle of incidence and beam polarization, the pulse number and the pulse-to-pulse time delay, are widely discussed. Finally, the potential mechanisms of LIPSS formation are briefly described.

Chapter 4 presents the numerical simulations based on the solution of the two-temperature model, both for the case of a single pulse (NPM) and for a burst with two or four sub-pulses.

Chapter 5 introduces the experimental setup with a detailed description of the bursts generation. The outgoing burst configurations are shown and characterized by an autocorrelator device. Short descriptions of the post-processing analysis equipment are provided together with analysis techniques, e.g. the contact angle measurements.

Chapter 6 presents the results of ablation experiments on stainless steel with bursts of sub-pulses with pulse duration of 750 fs and 238 fs, respectively. The burst features range from 1.5 ps to 24 ps in time delay and from 2 to 32 in number of sub-pulses. From experiments, the ablation threshold fluences and the material removal rate are evaluated for each burst configuration and compared among them.

Chapter 7 shows the influence of the number, time delay and state of polarization of the sub-pulses inside the burst on the laser-induced surface structure morphology on stainless steel targets. In particular, the study is focused mainly on the 1D and 2D LSFL. Finally, the wettability behaviour of some structures is discussed.

Chapter 1

Laser ablation of metals with ultrashort pulses

During last decade, short laser pulses in the micro and nanosecond range of pulse duration have been supplanted by ultrashort pico- and femtosecond laser pulses due to several advantages for material structuring as high quality and precision in material processing [9,10].

By definition, laser ablation denotes the macroscopic removal of material from the condensed matter upon intense laser irradiation. The ablation process occurs when laser fluence (energy density on the target surface) exceeds a characterized threshold fluence. The fluence is expressed by the ratio between the pulse energy E_p and the irradiated area on the surface [11]:

$$F = \frac{2 E_p}{\pi w^2}$$

where w is the spot dimension on the target surface. Below the threshold fluence no noticeable surface removal is observed. This threshold value depends on several factors, like pulse duration, number of pulses, repetition rate and target. In this chapter, interaction between ultrafast laser pulses and metal targets will be explained in more details. The description will focus on metals because stainless steel AISI 301/304 have been studied experimentally in this thesis.

1.1 Ultrafast laser interaction with matter

For material ablation, it's necessary to take into account the laser beam properties, the optical properties of the materials, such as reflectivity and absorption coefficient, and thermal properties as heat diffusion coefficient. Hence, when the laser radiation impinges the target surface, a portion is reflected due to the discontinuity in the real index of refraction at the interface between two mediums and the rest is transmitted into the material. Moreover, the reflected portion depends on the angle of incidence and the polarization of the light [12]. The ablation mechanism by ultrashort laser pulses involve the following steps (Fig. 1). First of all, the laser pulse energy is absorbed by electrons in the material. The laser therefore induces a transient nonequilibrium between the electron gas and the lattice. Then, the electronic

energy is transferred to the lattice until thermal equilibrium between the electron and lattice temperatures is reached. This transfer time is known as electron-phonon relaxation time, τ_{ep} , and it is typically on the order of picoseconds. The heat energy transferred to the lattice was used for its melting or vaporization.

Several studies have shown that other processes are involved in material removal, such as spallation, phase explosion, fragmentation, Coulomb explosion [13,14].

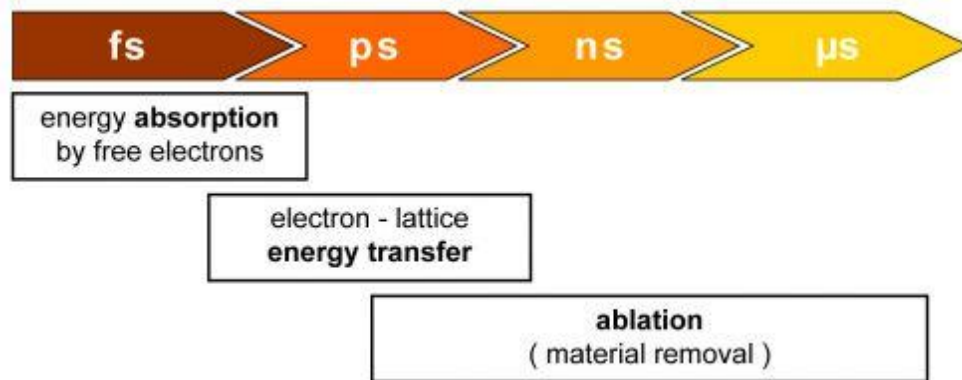


Fig. 1 Timescales of ultrashort pulse interaction with metals. [9]

Ablation process starts from the target's electronic system made of free electrons in the conduction band. Through linear absorption of the laser energy, the electrons that partially fulfil the conduction band absorb the laser photon energy moving toward unoccupied higher energy levels, with a growth of their kinetic energy. In detail, the conduction electrons mainly absorb the laser energy through inverse Bremsstrahlung.

For femtosecond laser pulses, the pulse width is so short that the electrons are excited instantaneously and thermalize by electron-electron collisions on a timescale of ~ 100 fs, reaching very high temperatures due to the low heat capacity of electrons. In this time lapse, lattice remains "cold". Successively, the lattice receives energy from the hot electronic system by means of electron-phonon coupling. The transient non-equilibrium lasts as long as two systems, electron and lattice, reach the same temperature.

Fig. 2 reports the excitation and relaxation processes in laser-irradiated metal. The modelling of the laser-matter interaction takes into account the electron and lattice temperatures. Such model is called two-temperature model (TTM).

The laser-induced excitation disturbs the electronic system into a non-equilibrium distribution which thermalized in the range of several tens of femtoseconds [15]. Such thermalisation brings electrons to a new Fermi

distribution characterized by a higher temperature. Finally, the following relaxation process conducts the electrons in thermodynamic equilibrium with lattice.

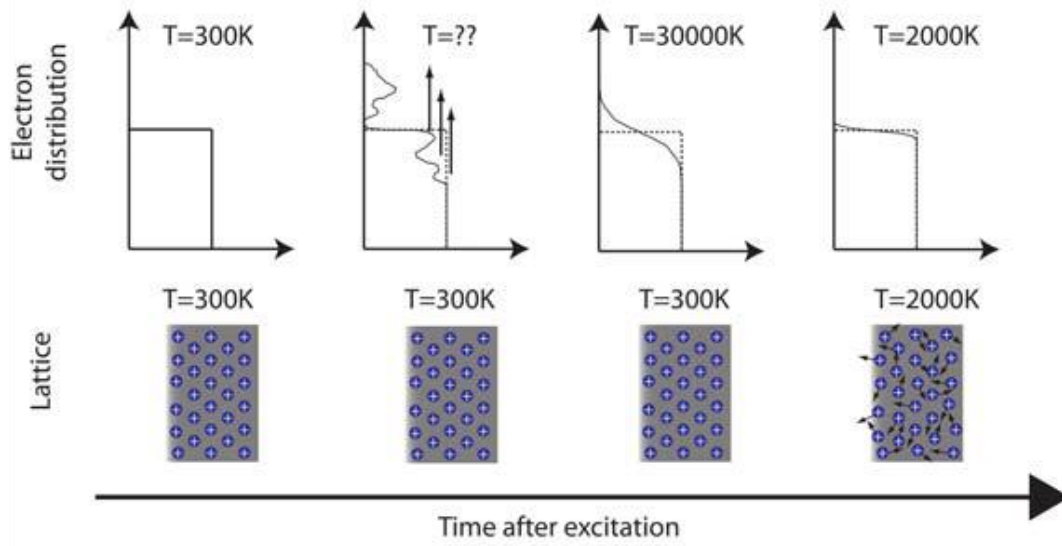


Fig. 2 Evolution of the energy transfer after laser excitation of the electronic system. The electrons in condition of nonequilibrium thermalized in a new Fermi distribution at higher temperature. The relaxation process with the lattice bring the two subsystems in equilibrium at the same temperature. [16]

Next to linear absorption, mechanisms like multiphoton absorption, i.e. simultaneous absorption of multiple photons by an electron, can be neglected in metals [17]. Therefore, multiphoton absorption is not taken into account for metals.

The change of free carrier density strongly affects both thermal and optical properties of irradiated materials and consequently laser absorption is influenced. The latter is related to the linear absorption (α) as well as the reflectivity (R), which are expressed in terms of refractive index (n) and extinction coefficient (k), by Eqs:

$$1.2 \quad R = \frac{(n-1)^2 + k^2}{(n+1)^2 + k^2}$$

$$1.3 \quad \alpha = 2 \frac{\omega}{c} k$$

with c the velocity of light in vacuum and ω the laser frequency. The refractive index and the extinction coefficient constitute the so-called complex refractive index (\hat{n}) which depends on the complex dielectric function (ϵ), according to equation:

$$1.4 \quad \hat{n} = n + ik = \sqrt{\epsilon}$$

equivalent to Eqs:

$$1.5 \quad n^2 = \frac{1}{2} \left[\sqrt{Re(\epsilon)^2 + Im(\epsilon)^2} + Re(\epsilon) \right]$$

$$1.6 \quad k^2 = \frac{1}{2} \left[\sqrt{Re(\epsilon)^2 + Im(\epsilon)^2} - Re(\epsilon) \right]$$

The extinction coefficient is responsible of the attenuation (absorption) of incident radiation with depth into the bulk material. Finally, the complex dielectric function is expressed by:

$$1.7 \quad \epsilon(\omega) = \epsilon_1(\omega) + i\epsilon_2(\omega) = 1 - \frac{\omega_p^2}{\omega^2 + i\omega v_e}$$

with

$$1.8 \quad \omega_p = \left(\frac{n_e e^2}{\epsilon_0 m_e} \right)^{1/2}$$

In equivalent way, the real and imaginary part of the complex dielectric function are expressed by:

$$1.9 \quad \epsilon_1(\omega) = Re(\epsilon) = 1 - \frac{\omega_p^2}{\omega^2 + v_e^2}$$

$$1.10 \quad \epsilon_2(\omega) = Im(\epsilon) = \frac{\omega_p^2 v_e}{\omega(\omega^2 + v_e^2)}$$

where ω_p the plasma frequency and v_e the electron collision frequency.

1.2 Two temperature model – TTM

When the target is irradiated with ultrashort laser pulses, the electron system absorbs the laser energy increasing its temperature. Then, the electrons transfer energy to the ions through scattering phenomena. The two mechanisms of energy transfer, i.e. from laser to electrons and from electrons to ions, involve two different temporal scales driven by the electron cooling time (τ_e) and electron-phonon relaxation time (τ_{ep}), respectively. In fact, the electron cooling time is around hundred femtoseconds while the electron-phonon relaxation time corresponds to several picoseconds. Though the electron-phonon coupling time may be comparable with the electron-electron collision time of few femtoseconds [18], the energy transfer from the excited electron system to the ion system happens in longer time.

The different masses between the light electron and the heavy ion (mass ratio of $m_e/m_{ion} \leq 1/2000$) plays a key role during scattering bringing a large transfer of momentum of the electron and a small energy transfer.

The electron system and lattice one can be described by T_e and T_l temperatures, respectively. The energy exchange between electrons and the lattice can be expressed by the equation:

$$1.11 \quad C_l \frac{\partial T_l}{\partial t} = -C_e \frac{\partial T_e}{\partial t} = G(T_e - T_l)$$

Where C_e and C_l are the electron and lattice heat capacity and G is the electron-phonon coupling factor, which represents the energy exchange rate between the two subsystems. An example of temporal evolution of the electron and lattice temperatures upon ultrashort pulse irradiation on metal, is shown in Fig. 3, in case of 1 ps pulses impinging on copper.

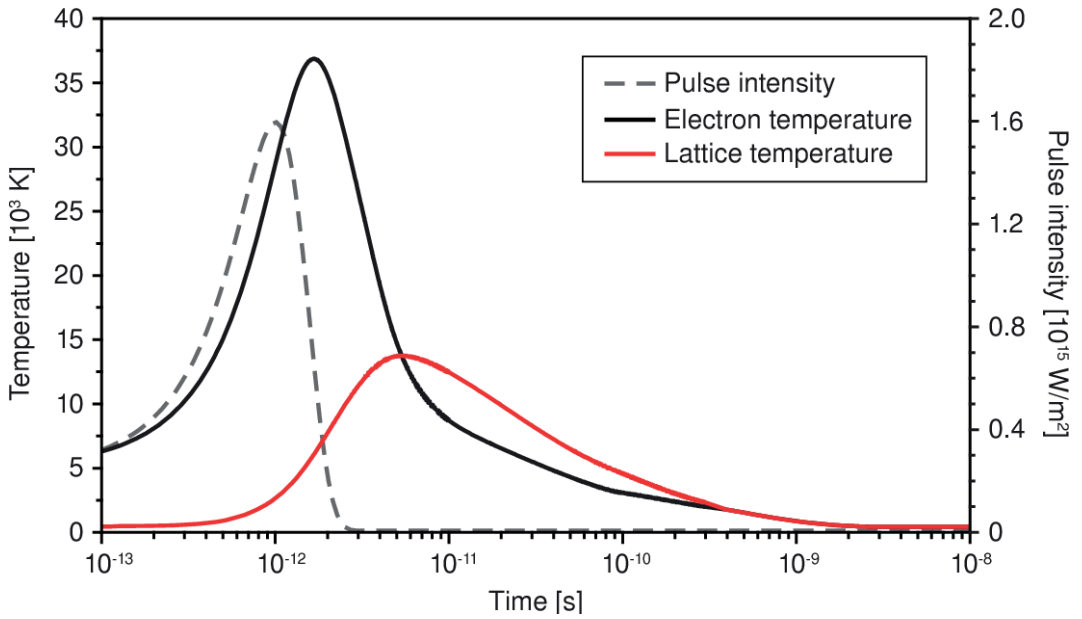


Fig. 3 Simulated electron and lattice temperature evolution in copper given by Two Temperature-Model. The dashed line represents the temporal profile of the pulse intensity with pulse duration of 1 ps. [19]

This plot has been evaluated by means of the so-called Two-temperature model, TTM, development by Anisimov in 1974 [20]. Each system, i.e. electrons and lattice, is studied separately and the temperature evolution in time (along the only optical axis direction z) is described by the following equations:

$$1.12 \quad C_e \frac{\partial T_e}{\partial t} = \frac{\partial}{\partial z} \left(k_e \frac{\partial T_e}{\partial z} \right) - G(T_e - T_l) + Q$$

$$1.13 \quad C_l \frac{\partial T_l}{\partial t} = \frac{\partial}{\partial z} \left(k_l \frac{\partial T_l}{\partial z} \right) + G(T_e - T_l)$$

where k_e and k_l are the thermal conductivities for each system which take into account the process of energy transport from the hot surface layer into

the bulk material. The first term in the right member of the Eqs. 1.12 and 1.13 represents the thermal diffusion for individual system, due to the heat conduction. The following term takes into account the electron-phonon coupling which describes how fast the lattice heats up. Q provides the heat source, i.e. the laser energy absorbed from electrons. In case of metals, the source term is given by Equation 1.14, which takes into consideration only the linear absorption process expressed by α .

$$1.14 \quad Q = \alpha I(z, t)$$

where:

$$1.15 \quad I(z, t) = (1 - R) I_{las}(t) \exp(-\alpha z)$$

This latter equation is the Lambert-Beer law related to the attenuation of laser beam intensity I_{las} while the light is travelling in depth, along the z-direction. The pulse laser intensity is supposed with temporal Gaussian profile regarding to the centre of spatial Gaussian beam.

The absorption coefficient can be replaced from the expression $\alpha = 1/\delta$, where δ represents the optical penetration depth, namely a thickness wherein the absorbed laser energy decays to $1/e$ of its initial value at the surface. Other absorption mechanisms (i.e. multiphoton absorption) can be neglected for metals. No source term is included in the lattice equation because it receives energy only from electron system, as described before.

By solving the TTM equations, the following solution of the lattice temperature is found:

$$1.16 \quad T_l \approx \frac{F_a}{c_l} \frac{1}{l^2 - \delta^2} \left[l \times \exp\left(-\frac{z}{l}\right) - \delta \times \exp\left(-\frac{z}{\delta}\right) \right]$$

where $F_a = I_0 A \tau_a$ is the absorbed laser fluence, that depends on the absorptivity A and the ablation duration τ_a . $l = (D\tau_a)^{1/2}$ is the effective penetration depth where D represents the electron thermal diffusivity. Depending on whether the optical penetration depth prevails or not on the effective penetration depth, it is possible to simplify the previous lattice temperature equation in:

$$1.17 \quad T_l \approx \frac{F_a}{c_l \delta} \exp\left(-\frac{z}{\delta}\right), \text{ if } \delta \gg l$$

$$1.18 \quad T_l \approx \frac{F_a}{c_l l} \exp\left(-\frac{z}{l}\right), \text{ if } \delta \ll l$$

By considering that significant evaporation can be obtained if the energy stored in the lattice is much higher than the latent heat of evaporation, it is possible to assume that significant material removal is reached once evaporation is ignited. This condition occurs for $C_l T_l \geq \rho \Omega$, where $C_l T_l$ represents the energy absorbed by the lattice while $\rho \Omega$ the latent heat of

evaporation, with ρ the density of the material and Ω the latent heat of evaporation per unity of mass. By substituting the significant evaporation and ablation condition in Eqs.1.17-1.18, the ablation depth as a function of the laser fluence can be estimated by:

$$1.19 \quad L \approx \delta \ln \left(\frac{F_a}{F_{th}^\delta} \right), \text{ if } \delta \gg l$$

$$1.20 \quad L \approx l \ln \left(\frac{F_a}{F_{th}^l} \right), \text{ if } \delta \ll l$$

Where F_{th}^δ is the ablation threshold fluence, i.e. the lowest value of the laser fluence necessary to damage the target surface in a permanent way. The two equations represent two different ablation regimes due to irradiation by ultrashort laser pulses, the gentle regime and the strong regime. The gentle regime, also called optical ablation regime, is characterized by an ablation depth per pulse comparable with the optical penetration depth. When the laser fluence exceeds the value of F_{th}^l , the strong ablation regime is established and the effective penetration depth determines the ablation depth per pulse. Gentle or strong ablation regimes depend on both the heat penetration depth and the optical penetration depth. When the condition $\delta \gg l$ is verified, the ablation process evolves slowly and very precise processing occurs thanks to the absence of molten material, therefore, the amount of the amount of heat transferred in the bulk material is negligible. On the contrary, when the heat penetration depth is much higher than the optical penetration depth at high laser fluence, strong ablation is established because the heat diffusion lets energy to reach deep layers of the irradiated target.

Higher ablation depths can be obtained in this regime at the expense of the ablation quality (surface roughness, molten material).

1.3 Ablation threshold fluence

The minimum energy density amount which is able to generate a permanent damage on irradiated surface represents the ablation threshold fluence, F_{th} . Its value depends on material and laser parameters.

When the laser energy density hitting the sample grows, different types of permanent damage and/or surface morphologies can be visible.

Ultrafast pulses with low energy can remove heterogeneous surface layers, such as oxide layers, cleaning the surface rather than induces craters or surface damages. This cleaning may involve a change of the optical property (absorptivity or reflectivity) of the irradiated surface. Increasing the pulses energy, a first laser-induced damage on the target surface is represented by the ripples formation. In general, these ripples are organized in well periodic patterns, called laser-induced periodic surface structures (LIPSS). The LIPSS

origin and their features will be discussed extensively in a dedicated chapter. Moreover, smooth surfaces can be due to material melting and subsequent re-solidification. This damage results more evident when using pulses with longer temporal durations, like e.g. nanosecond or longer pulses. Finally, for high fluence, irregular morphologies are observed due to the ejection of vaporized material. If a pulse having gaussian spatial distribution is considered, due to its intensity profile, annular damage regions surrounding the ablation crater can be recognized.

Different methods have been presented in literature to estimate the threshold fluence. Jee et al. [21] proposed a statistical approach because the ablation process with long (10 ns) laser pulses exhibits a strong stochastic behaviour. The presence of defects on the sample surface may indeed influence the damage threshold. Another method is based on the ablation depth regression technique. From the ablation depth trend as a function of the laser fluence, it is also possible to evaluate the ablation threshold by fitting the experimental data. Samad et al. [22] introduced a geometrical method, called diagonal scan technique. This is based on the measurements of the ablation profile of a scan line obtained on the target surface by moving the beam laser simultaneously on longitudinal and transversal direction. The method proposed by Liu et al [23] is widely used and it is based on the assumption that the ablated region by a Gaussian beam depends on the laser fluence. In detail, the estimation of the ablated region is given by the measurement of the ablated crater diameter. Several studies have been carried out on the threshold fluence to understand which parameters can influence its value. The number of impinging pulses represents one of these, whose influence on F_{th} is described in the next section.

1.4 Incubation effect

Irradiation with multiple pulses has been found to reduce the threshold fluence for material ablation. This effect, which has been reported on a wide variety of materials, is known as incubation. Byskov-Nielsen et al. [24] carried out ablation studies on a tungsten target, irradiated with 200 fs-pulses at 800 nm wavelength. The number of pulses from 1 to 1000 was selected from a train of pulses, with repetition rate in the range 10 – 1000 Hz by a mechanical shutter. They observed that the ablation fluence decreases as the number of impinging pulses rises until 100. For higher amounts of pulses, it remained almost constant, as reported in Fig. 4.

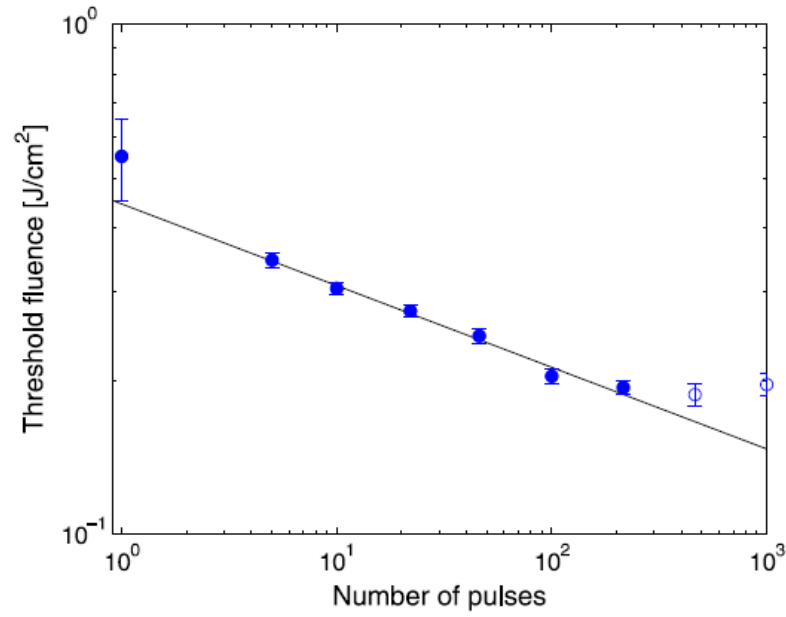


Fig. 4 Threshold fluence versus the number of the impinging pulses on a tungsten target. The filled data points are used for the fit line. [24]

The authors evaluated the threshold fluence by fitting the experimental data of the crater diameters versus the laser fluence. Considering the Gaussian shaped intensity profile of Fig. 5, Mannion at al. [11] showed that 100 pulses were able to induce a larger damage with respect to 5 pulses of same pulse energy.

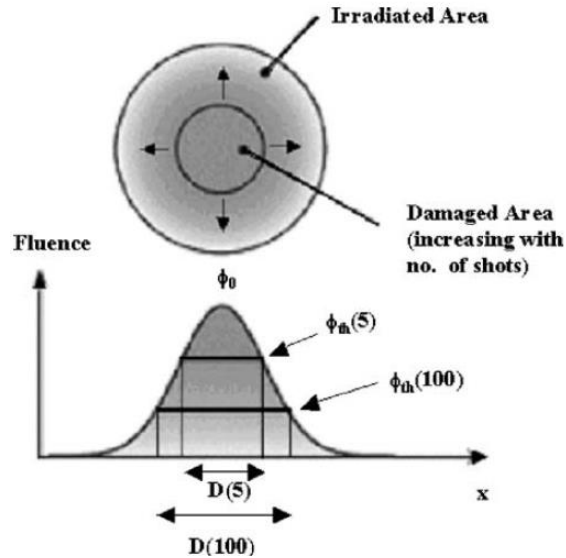


Fig. 5 Sketch of the increasing dimension of the damage area, as a consequence of the incubation effect. While $N = 5$ pulses can generate a permanent damage on the sample surface only at high fluence, with $N = 100$

incident pulses a lower fluence for the damage onset is found, and a larger damage is correspondingly created. [11]

Incubation is often ascribed to a damage accumulation mechanism, which is considered to be responsible for the lowering of the damage threshold pulse after pulse. The first pulses generate local defect, whose number increases pulse after pulse. These defects improve the laser absorption and therefore an increasing of their number leads to a higher absorption. Nonetheless, the physics of such an effect is not completely understood, yet. Sun et al. [25] have introduced an incubation model based on two physical mechanisms, i.e. increase of the energy deposition per pulse (absorption) and a decrease in the critical energy needed to damage the material during multi-pulse irradiation. For metals, Jee et al. [21] proposed the first phenomenological model to explain the trend of ablation threshold as a function of the number of applied pulses by introducing a power law, where an incubation coefficient S describes the strength of incubation effect, as stated in Eq.:

$$1.21 \quad F_{th}(N) = F_{th}(1) \cdot N^{(S-1)}$$

Here, $F_{th}(N)$ is the threshold fluence for N pulses while $F_{th}(1)$ is the threshold fluence for a single shot. When $S = 1$ incubation is absent and the ablation threshold does not change, irrespective of the number of pulses. On the contrary, when threshold reduction is observed, the incubation coefficient gets lower ($0 < S < 1$) and incubation effect becomes stronger. Laser hardening can be obtained for $S > 1$ that means an increase of the threshold fluence with the number of pulses. The Jee model was found to be valid not only for metals [11,21] but for semiconductors [26] and dielectrics [27–29] and for each material a peculiar value of S was obtained. Moreover, Jee applied short pulses in metal ablation. His model was extended also for femtosecond pulses by Neuenschwander et al. [30] for iron and copper ablation. They excluded mechanisms of thermal stress and plastic deformation, proposed by Jee and they hypothesized that incubation is originated by an increase of surface roughness, which enhances the absorption of the following laser pulses.

Nonetheless, the incubation model in Eq. 1.21 predicts that the ablation threshold is zero for an infinite number of laser pulses, which is clearly a not physically plausible situation. In fact, Fig. 4 shows that the threshold fluence reaches a saturation when the number of applied pulses is above 500.

Di Niso et al. [31] found that, owing to incubation, the threshold fluence of steel significantly reduces with the number of impinging pulses N , but no further decrease is observed for $N > 1000$ [31]. In order to describe this behaviour, a new incubation model was proposed:

$$1.22 \quad F_{th}(N) = F_{th}(\infty) + \Delta F_{th}(1) \cdot N^{(S^*-1)}$$

where a constant threshold at infinite number of pulses $F_{th}(\infty)$ was introduced to take account of the saturation effect at high number of pulses. Here, $\Delta F_{th}(1)$ represents the complementary value to be added to $F_{th}(\infty)$ for obtaining the single-shot ablation threshold, while S^* is the modified incubation coefficient. Di Niso et al. proved that the modified model fitted the experimental data better than the previous incubation model. Actually, a constant offset to describe saturation of incubation for high number of pulses was originally proposed in case of dielectrics by Ashkenasi et al. In their work incubation was ascribed to the formation of colour centers and to the consequent absorption enhancement [32]. The change of the damage threshold $\Delta F_{th} = F_{th}(N) - F_{th}(N-1)$ experienced by consecutive pulses was considered proportional to $F_{th}(N-1)$. The following equation was used to describe the dependency of threshold fluence on the number of pulses:

$$1.23 \quad F_{th}(N) = F_{th}(\infty) + [F_{th}(1) - F_{th}(\infty)] \cdot \exp[-k(N-1)]$$

Here, the empirical parameter k was introduced to indicate the strength of defects accumulation, which was responsible for the absorption increase and fluence threshold reduction.

Sun et al. [25] explicitly introduced in the incubation model the absorption coefficient α and its change due to multi-pulse irradiation:

$$1.24 \quad F_{th}(N) = \frac{F_{th}(1) - [-F_{th}(\infty)(1 + \frac{\Delta\alpha}{\alpha_0})][1 - e^{-\gamma F(r)(N-1)}]}{(1 + \frac{\Delta\alpha}{\alpha_0})F_{th}(1)[1 - e^{-\beta F(r)(N-1)}]}$$

In their model, α_0 is the initial absorption coefficient, $\Delta\alpha$ is defined as the difference between the maximum absorption coefficient α_{\max} and α_0 , γ is a coefficient introduced to describe the pulse induced change of the material, β is a material dependent parameter, describing the efficiency with which a pulse of a given fluence changes the absorption coefficient towards its maximum value, and $F(r)$ is the coordinate dependent fluence. As in Eq. 1.21, $F_{th}(1)$ is the threshold fluence for a single shot while a constant offset $F_{th}(\infty)$ is introduced to describe saturation of threshold fluence at high number of pulses.

Chapter 2

Laser ablation with multiple laser pulses

Most of the ultrafast laser-based industrial processes use repetition rates in the kHz and MHz regime which correspond to delay time between consecutive pulses in the range from a millisecond to a few microseconds. In this time interval, the residual heat generated on the target by the first pulse is completely diffused into the bulk. Also, the plume induced by laser ablation is vanished when the following pulse hits the target surface.

In this chapter, I will summarize the state-of-the-art on laser ablation by multiple laser pulses with delay time between consecutive pulses shorter than 1 microsecond. These pulse-sequences are so-called bursts of pulses [4,33]. In this thesis, the use of bursts will be indicated as burst mode (BM). The influence of the burst features, such as delay time between pulses and number of pulses inside the burst, on the laser-matter interaction will be highlighted. In detail, the influence of the delay time in case of bursts with only two pulses, indicated as double pulses, will be addressed. First, a brief introduction on how to generate bursts is reported.

2.1 How to generate bursts of pulses

Time delays between pulses in the burst lower than 1 microsecond correspond to intra-burst repetition rates higher than 1 MHz.

Bursts can be generated through two methods, *pulses picking* from the laser oscillator or *splitting laser pulses* into sub-pulses. In the following, a short description was referred for each method.

2.1.1 Burst generation by pulse picking

Bursts can be created by using an acousto-optic modulator (AOM) or any other electro-optical device enabling to pick train of laser pulses from the ultrafast laser oscillator that is usually working at extremely high repetition rates of hundreds of MHz. Then, the picked pulses are amplified inside the ultrafast laser source. The pulse picker selects a number n of pulses out of N pulses exiting from the laser oscillator. Fig. 6 shows the burst generation made of four picked pulses every six pulses coming out from the oscillator

working at a repetition rate f . Hence, the intra-burst repetition rate is the one of the laser oscillator while the burst repetition rate is lower, e.g. $f_{burst} = f/6$ for the case shown in Fig. 6. Since the maximum number of pulses that can be selected every N pulses, is $N - 1$ [4], with this method the intra-burst time delay is limited by the laser oscillator repetition rate.

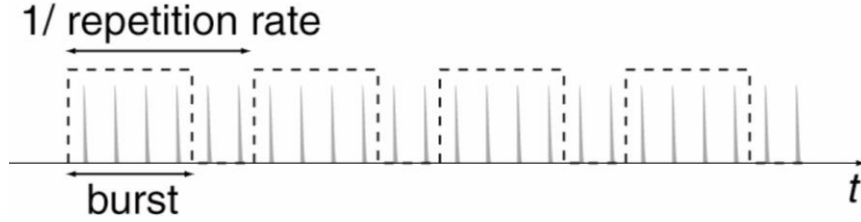


Fig. 6 Bursts of 4 pulses (inside dashed-lines) with intra-burst repetition rate equals to laser repetition rate. [4]

2.1.2 Burst generation by splitting laser pulses

Bursts can be generated by splitting each laser pulse, like e.g. using polarizing beam splitter cubes. A Michelson interferometer based on a polarizing cube allows to generate double pulses, or, in other words, bursts with two sub-pulses. The delay between the two sub-pulses Δt depends on the difference in optical path Δl between the two arms of the interferometer, according to the relation $\Delta t = \Delta l/c$, with c the speed of light. Hence, by simply changing the arm's length, it is possible to tune the time delay. Moreover, to obtain sub-pulses of same energy it is necessary to use appropriately polarized laser beams so that to obtain beam splitting 50:50. With this method, it is possible to generate bursts with multiple sub-pulses using a cascade of Michelson interferometers as shown in Fig. 7 [34]. If m interferometers are used, each pristine laser pulse can be split in a burst of maximum 2^m sub-pulses. To obtain burst with equally delayed sub-pulses, the length of subsequent delay lines (Δl) should be doubled which requires a big space.

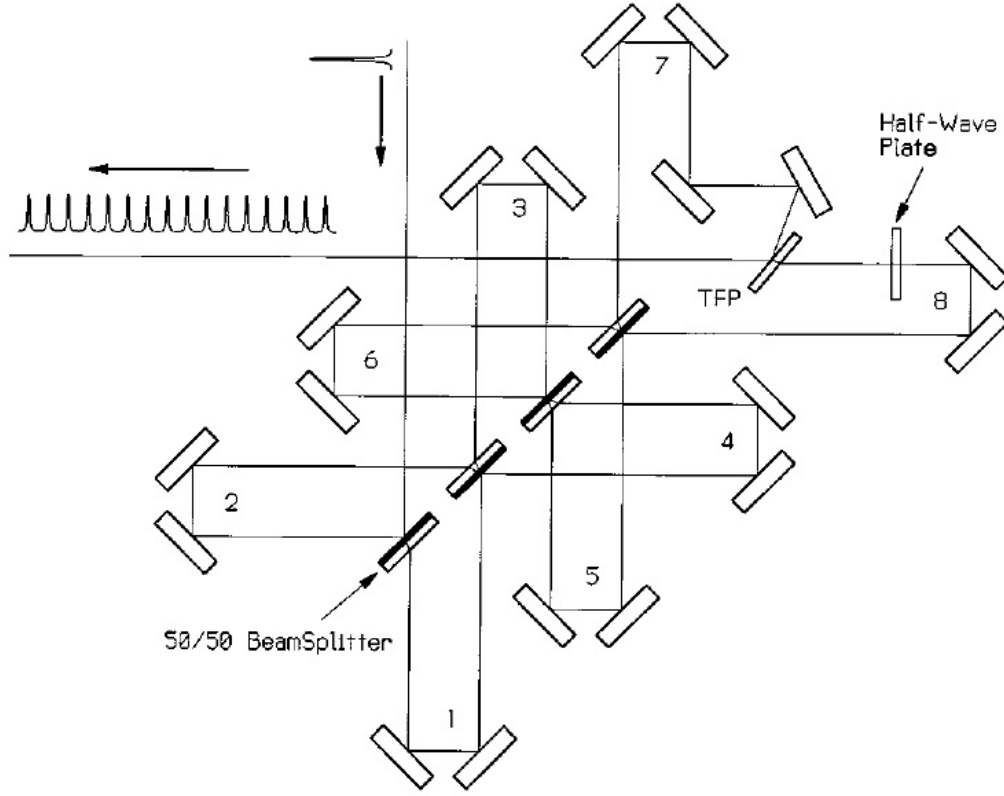


Fig. 7 Set-up of the burst generator based on Michelson-interferometers. The pristine laser can be split up to 16 sub-pulses with intra-burst time delay defined by the interferometer arm's lengths. [34]

Another possibility for bursts generation, is to use birefringent crystals which optical axis is on the polished surface [35,36]. When a linearly polarized laser pulse arrives on the crystal with its polarization oriented along the bisector between ordinary and extraordinary axes of the crystal, two sub-pulses are originated with same energy and orthogonal polarization. Indeed, the polarization of each sub-pulse is parallel to one of the two axes of the crystal, as shown in Fig. 8. The time delay between the two sub-pulses is proportional to the difference between the two refractive indexes (Δn) and to the crystal thickness (l):

$$2.1 \quad \Delta t = \frac{l}{c} \Delta n$$

As for the polarizing cubes, to obtain burst with multiple sub-pulses, a cascade of birefringent crystals is requested (Fig. 8). So that, with m crystals, burst of maximum 2^m sub-pulses are generated. In order to have bursts with constant intra-burst delay, it is necessary that the thickness of each crystal is the double of the preceding one. In addition, to keep the same energy for all sub-pulses, the crystal's axes should be oriented in such a way to be always at the bisector of the incident pulses polarizations.

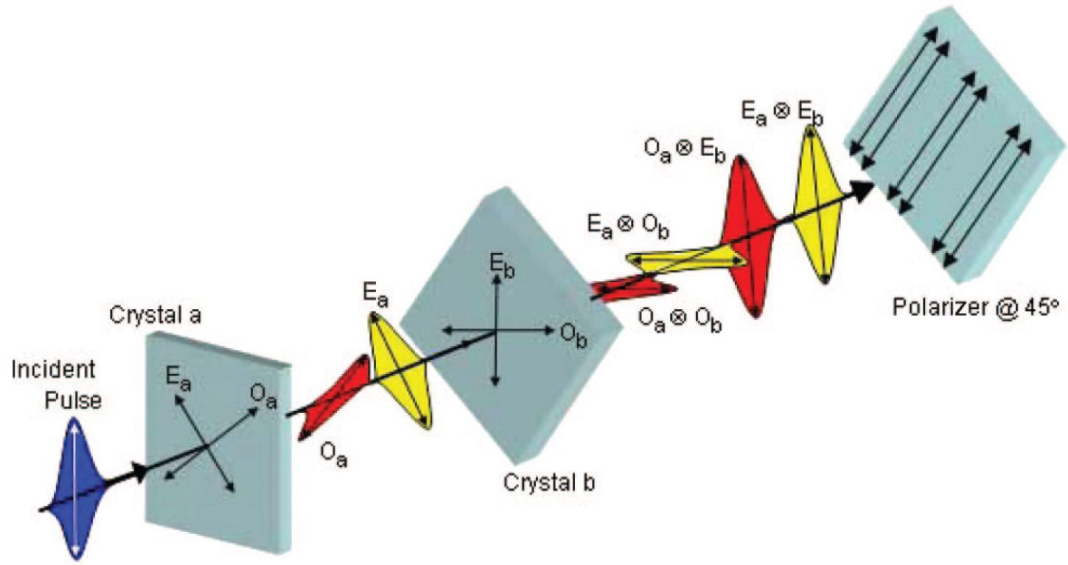


Fig. 8 Generation of a burst with four sub-pulses by means of two birefringent crystals. The pristine laser pulse impinges on the *Crystal a* with linear polarization along the bisector between ordinary and extraordinary axes. The two output sub-pulses assume polarization parallel to the orientation of the axis traversed and their temporal delay results proportional to the crystal thickness. Each sub-pulse impinges on *Crystal b* (of double thickness) along the bisector of the crystal axis, therefore it generates other sub-pulses. The final result is a burst which consists of four equally time delayed sub-pulses with orthogonal polarizations and same sub-pulse energy. [35]

In bursts generated by pulse splitting, the intra-burst repetition rate is independent from the laser source. This gives more flexibility compared to the pulse picking method. Moreover, the typical sizes of the set-ups with Michelson-interferometers are greater than the birefringent crystals to produce intra-burst time delays in the femto and/or picoseconds range. Nevertheless, the damage threshold of the optical crystals dictates the limit of the impinging maximum pulses energy, and thereby also the maximum sub-pulses energy outcoming from the burst generator as a function of the pulse splitting.

2.2 Laser ablation with double pulses

Several works have been focused on the influence of the time delay between sub-pulses on the laser ablation with double pulses. For these studies, the burst generation based on Michelson interferometer has been widely used since it provides double pulses with tuneable delay.

Semerok et al. [37] conducted experiments with double pulses of same energy to generate craters on copper. For the investigated pulse duration (50 fs, 160 fs, 675 fs and 2 ps) at 800 nm of wavelength, they found that for delay time shorter than 1 ps, the craters were twice deeper than the ones obtained with single pulses of equal energy while for delays longer than 10 ps, double pulses and single pulses ablated craters of the same depth, as shown in Fig. 9. The authors ascribed this trend to reheating of the plume for delays longer than 10 ps, as observed also by Axente et al. [38].

Analogue results on copper were obtained by Noel et al. [39] for double pulses of 100 fs (squared points in Fig. 10). The latter were theoretically reproduced by Povarnitsyn et al. [40] using a hydrodynamic model of the ablation plume to evaluate the crater depth obtained for different delays between double pulses, as reported in Fig. 10 (triangular points).

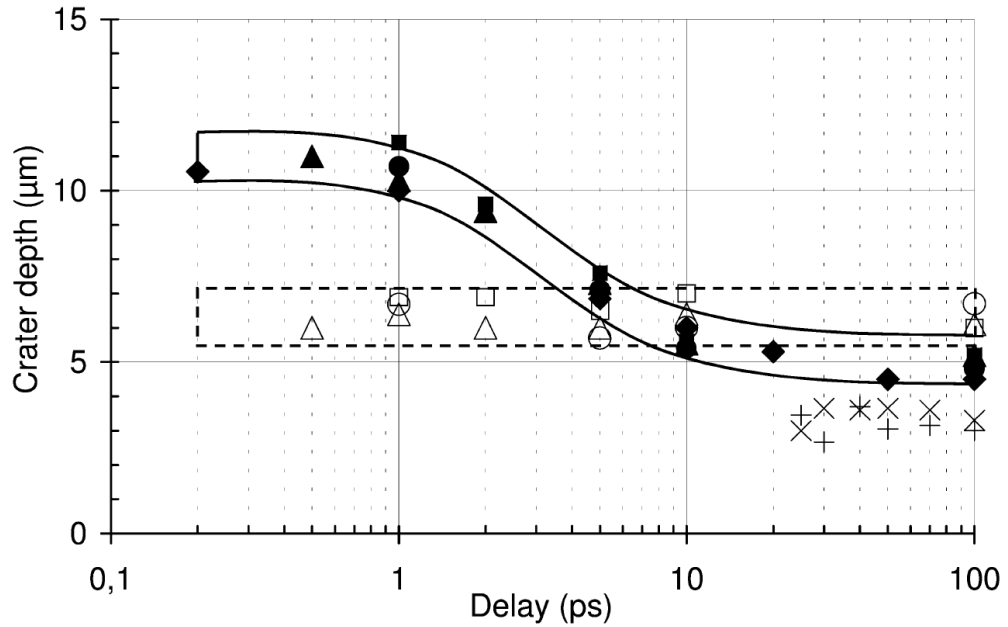


Fig. 9 Crater depths as a function of delay between double pulses. Data obtained with pulse durations of 50 fs (\blacklozenge), 160 fs (\blacktriangle), 675 fs (\blacksquare) and 2 ps (\bullet) are indicated by filled symbols and empty symbols for double pulse ($2 \times 20 \mu\text{J}$) and single pulse ($20 \mu\text{J}$) ablations, respectively. Crater depths obtained with 10 ps pulses are represented by (+) for single pulses and by (x) for double pulses. [37]

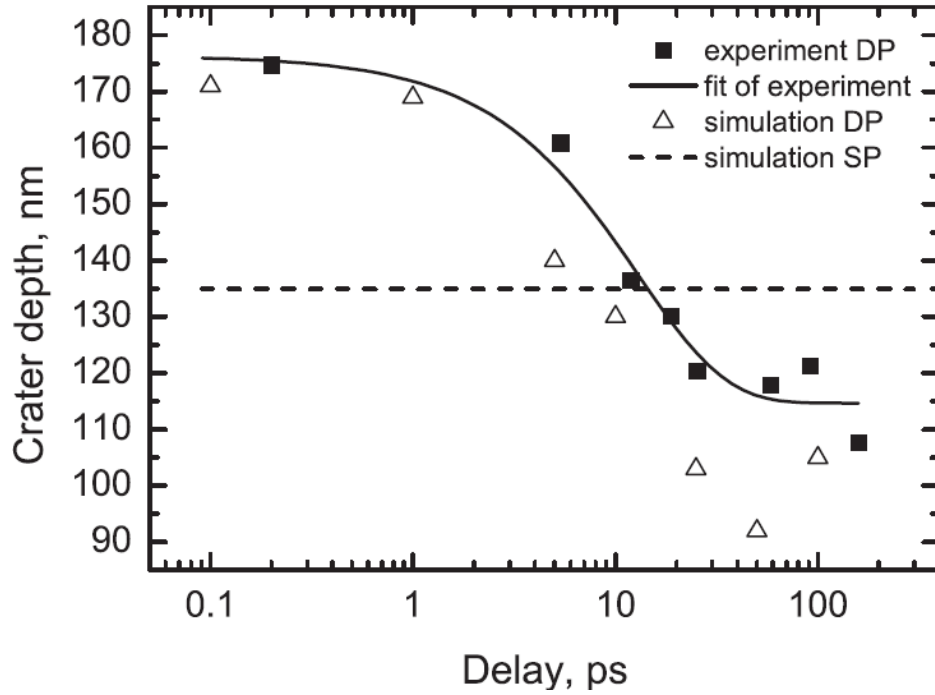


Fig. 10 Crater depth as a function of the delay between the double pulses for experimental points [39] and those simulated by Povarnitsyn [40]. Solid line fits of experimental data while dash line represents the crater depth in SP simulation.

The explanation is better clarified in a subsequent study of the same authors [41] conducted on aluminium. They studied the evolution of the shock wave (SW) generated during the ablation process and followed by a rarefaction wave (RW). In particular, they calculated the ions temperature (Fig. 11a-b) and pressure distribution (Fig. 11c-d) after irradiation with single and double 100 fs pulse.

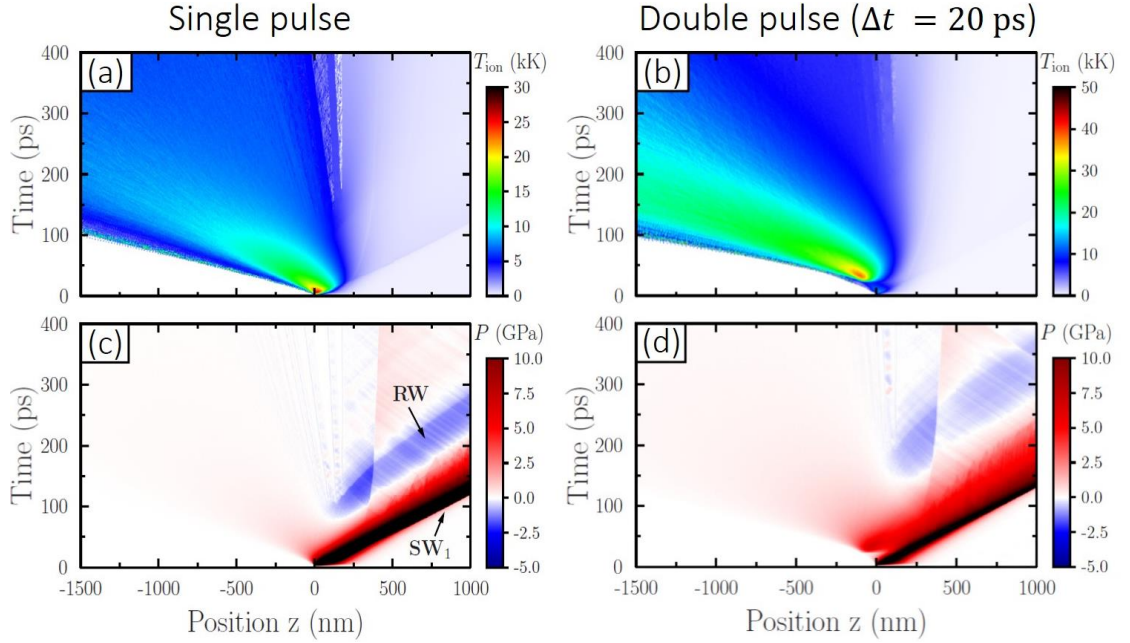


Fig. 11 Contour plot of the ion temperature upon irradiation of aluminium target with (a) single pulse of 4 J/cm² and (b) double pulse of 2 J/cm² delayed of 20 ps. The relative pressure graphs are reported in case of (c) single pulse and (d) double pulse. The ‘zero’ position ($z = 0$ nm) corresponds at the sample surface while the positive axis is oriented into the bulk material. [41]

The authors highlighted a different ablation dynamic of the double pulse compared to the single pulse case when the delay between pulses was greater than 10 ps. In this case, the shock wave generated by the second pulse suppressed the rarefaction wave of the first pulse bringing to a reduction of the ablation depth. Moreover, Fig. 11d shows that the second pulse absorption was localized at a position $0 \leq z \leq 100$ nm above the target surface thus determining an increase of the temperature in the plume (Fig. 11b). This reheating of plasma is known as plasma shielding effect. It becomes stronger for delays larger than 20 ps preventing the second pulse to reach the target.

A further study on laser ablation in aluminium by double pulse has been conducted by Mildner et al. [42] using laser-induced breakdown spectroscopy (LIBS) analysis. They considered a wide range of delays between the two pulses, from 100 fs to 2 ns. Four ablation regimes were identified according to the time separation between pulses. For delays shorter than 1 ps (regime I), the second pulse induces only a delayed energy deposition into electron system and a retarded electron-phonon coupling. For delays from 1 to 10 ps (regime II), the second pulse arrives on the target when the electron-lattice thermal equilibrium is not reached yet, and the melting

temperature of the lattice can be exceeded. In the regime III, i.e. for delays up to 100 ps, the first pulse generates a liquid phase in the bulk and a hot and dense plasma plume above the surface. Despite the liquid phase can absorb more laser energy because its reflectivity is lower than the solid state, the plasma shields/reflects the second incoming laser pulse. For delays longer than 100 ps (regime IV), the plasma is expanded, therefore its outer shell becomes transparent to the second pulse that reaches the inner regions of the plume, reheating it. A graphic representation of the IV regime, from a recent work of Pangovski et al. [43], is reported in Fig. 12 where the expansion of the shock and rarefaction (recoil) waves are represented, before the arrival of the subsequent pulse after nanoseconds time delay.

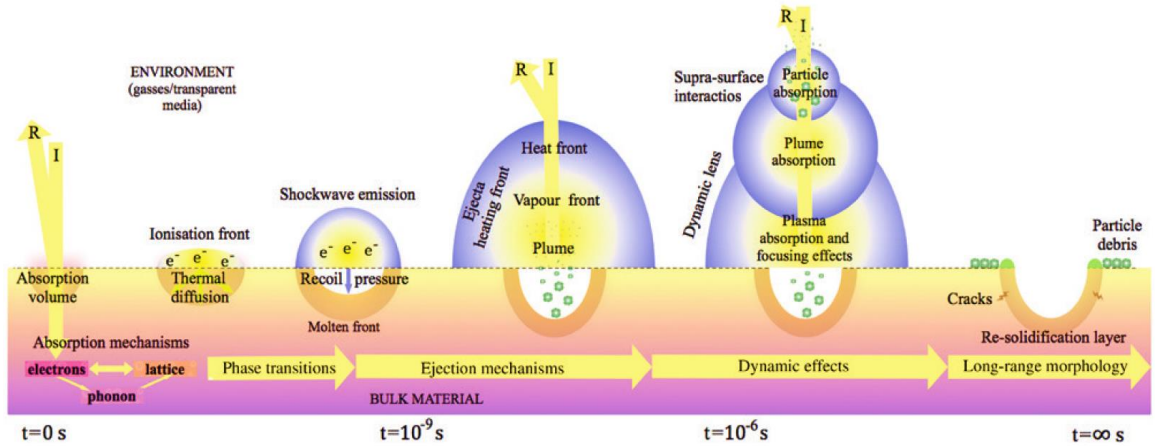


Fig. 12 Timescales of interaction mechanisms between subsequent pulses. [43]

The explanation based on the four regimes is in agreement with experimental results from Semerok [37] and simulations from Povarnitsyn [40,41].

Recently, Schille et al. [5] presented an experimental study on the ablation efficiency of stainless steel target with ultrashort double-pulses with variable time delays. The obtained results demonstrated that double-pulse processing reduced the ablation threshold fluence with respect to the single pulse case identifying three different ablation regimes (Fig. 13a). On the other hand, the removal efficiency (evaluated by dividing the ablated volume per pulse by the pulse energy) improved using double pulse instead of single pulse only for time delay shorter than 1 ps or longer than 10 ns (Fig. 13b). Further, the higher removal efficiency was achieved when double-pulse processing using femtosecond pulses instead of picosecond pulses, comparing the experiments with 700 fs and 10 ps in pulse duration.

Similar trends of the removal efficiency by double pulse were obtained by Sailer et al. [6] on stainless steel for pulse durations of 0.9 and 20 ps and by

Neuenschwander et al. [7] for 10 ps pulses. The latter proposed the existence of an optimum value of the pulse fluence which maximizes the removal efficiency.

In the works [5–7] some bursts configurations shown removal efficiency higher than NPM. In particular, Fig. 13b shows higher removal rate for double pulse delayed of 10 ps and 18 ps and pulse energy higher of 4 μJ , while Fig. 14 [6] for time delay of 13.4 ns and pulse energy lower of 0.3 μJ .

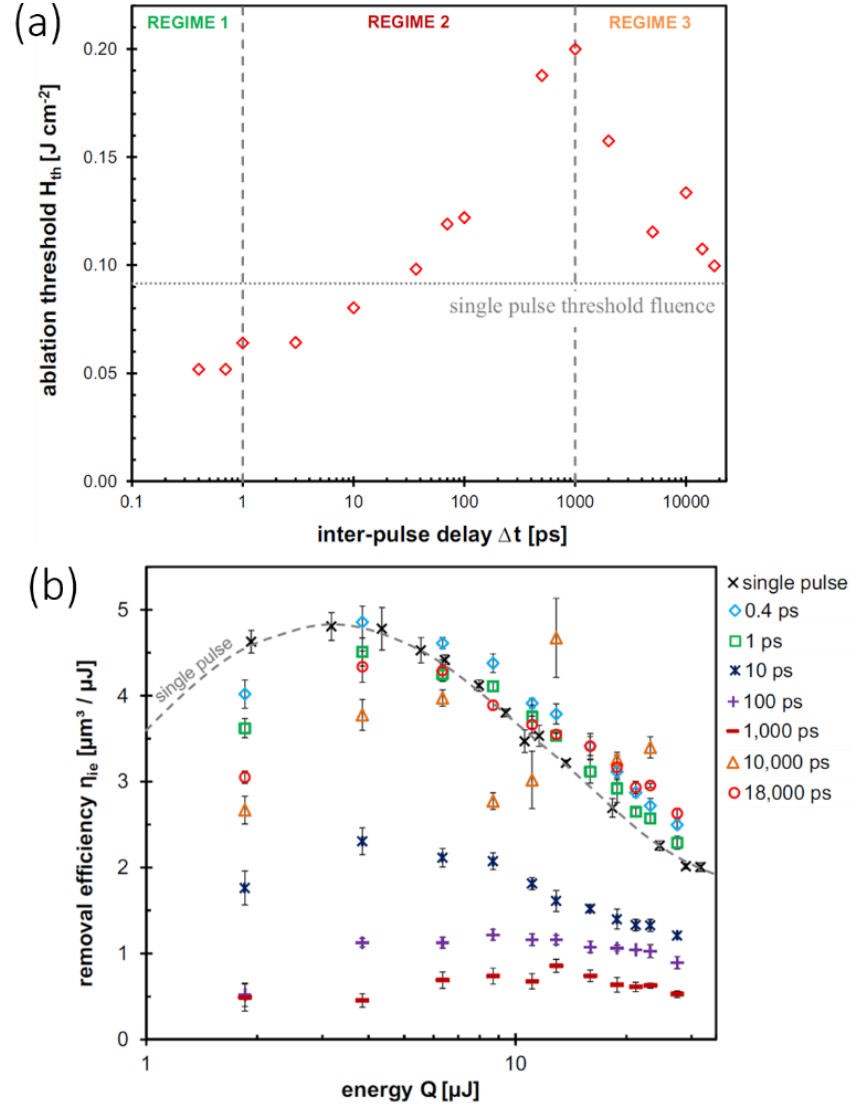


Fig. 13 Ablation threshold fluence as a function of the time delay between double-pulse (200 fs in pulse length) which is varied in the range 0.4 - 18000 ps. The single pulse is reported as a reference (horizontal line). Three characteristic ablation regimes are distinct (dashed lines). (b) Removal efficiency versus pulse energy for inter-pulse delay in the range 0.4 – 18000 ps. The dashed line represents the single-pulse case (NPM). The

experimental data are related to ablation process of craters on stainless steel with 50 double-pulse or single-pulse at repetition rate of 200 kHz. [5]

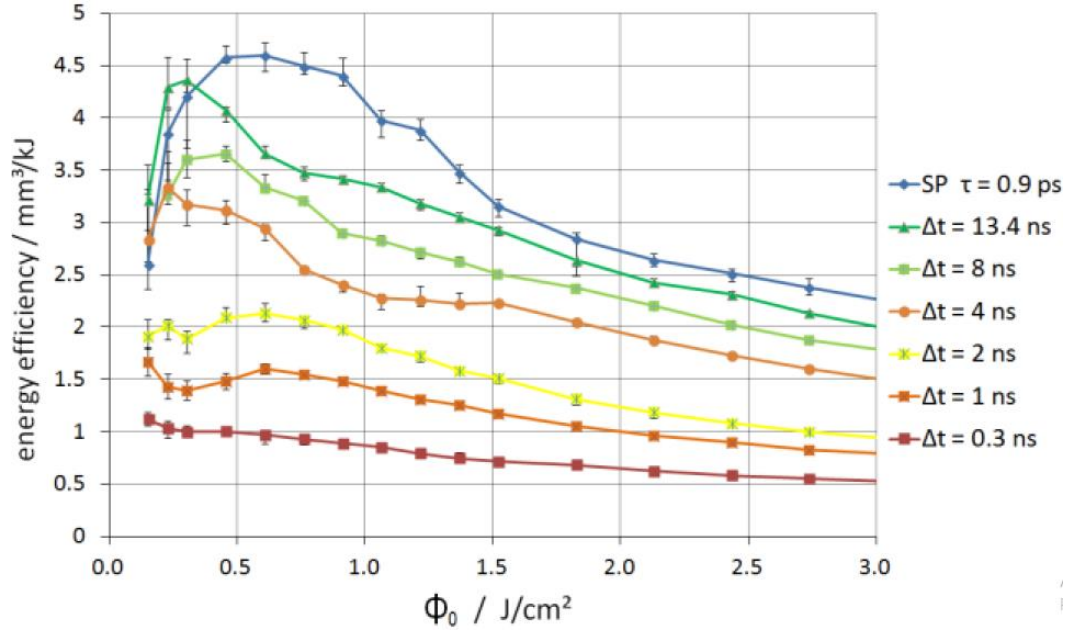


Fig. 14 Energy efficiency for the ablation of stainless steel as a function of the laser fluence of the individual pulses. Trends for different time delay in the range 0.3 – 13.4 ns are reported. The pulse duration is 0.9 ps while the repetition rate is 400 kHz for double pulse and 800 kHz for single pulse. [6]

2.3 Laser ablation with bursts of pulses

The advantages expected from using BM in laser ablation manufacturing processes are the reduction of the heat load and the thermal induced stress and damage to the material while using relatively high laser average powers and repetition rates. Indeed, the BM based on pulse splitting, represents a useful way to work simultaneously with high-average laser power and low fluence per sub-pulse because the peak intensity of each sub-pulse is lower than the pristine pulse.

The unwanted effect of the heat accumulation increases the target temperature with a widening of the heat affected zone (HAZ) leading to irreversible thermal damage, such as cracks or melting, with consequent worsening of the ablation quality and precision of the manufacturing process [31,44].

In the last years, several investigations have been performed by other researchers to achieve a deep knowledge of the laser-matter interaction mechanisms during BM processing. Advantages in the use of burst mode

processing were underlined in the theoretical work of Kerse et al. [45]. They proved that an ablation-cooled material removal was possible in burst mode under appropriate conditions. The principle was that the ablated material moved away the thermal energy reducing the average temperature of the target. It known that after the target irradiation the heat diffused from the processing region into the bulk of the target. For ablation cooling, the time delay between consecutive pulses must be reduced in order to avoid the heat conduction into the bulk. In detail, it was necessary that the time delay was lower than τ_0 , the thermal relaxation time, inversely proportional to thermal diffusivity of the material (Fig. 15).

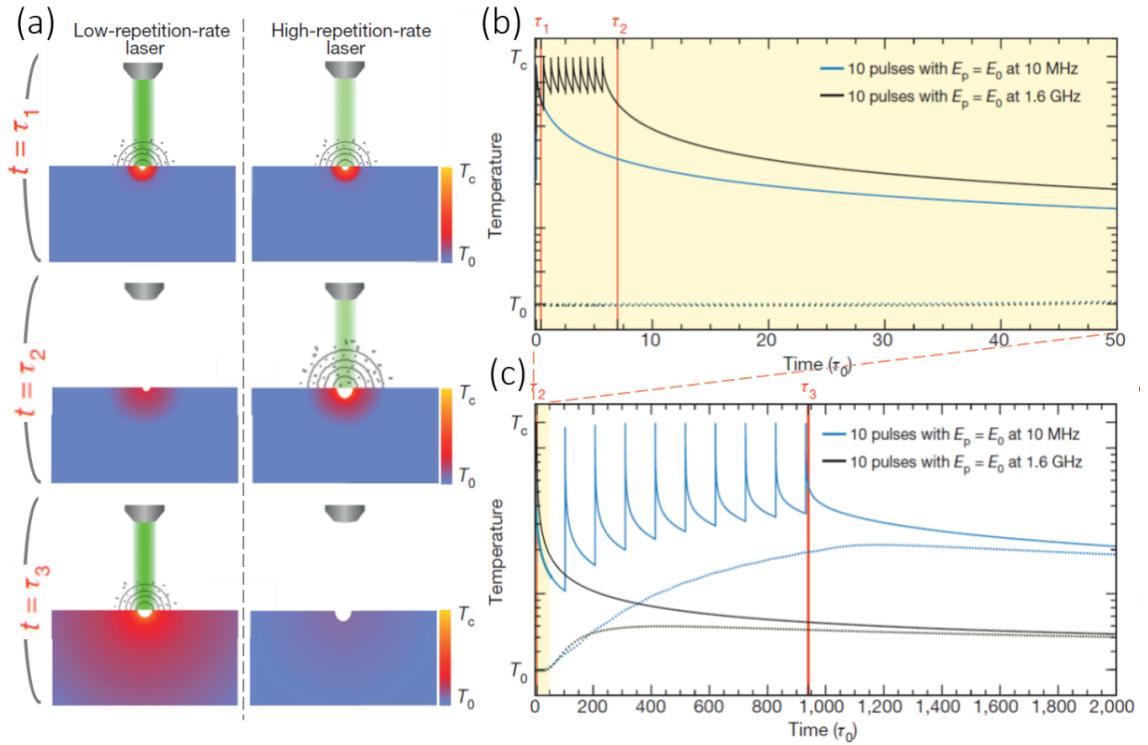


Fig. 15 Representation of the ablation process by burst of 10 pulses in case of low (left column) and high (right column) intra-burst repetition rate, 10 MHz and 1.6 GHz respectively. For both the columns, traditional ablation on the left and ablation-cooled on the right, diagrams of the temperature profile are shown for three instants: $t = \tau_1$ is before the arrival of the second pulse in the burst at high repetition rate; $t = \tau_2$ is shortly after the arrival of the last pulse in the burst at high repetition rate; $t = \tau_3$ is shortly after the arrival of the last pulse in the burst at low repetition rate. (b) and (c) show the evolution of the simulated temperature upon the burst irradiation on the surface (solid lines) and below the surface (dotted lines). The time scale is normalized with respect to τ_0 , the thermal relaxation time. T_c is the critical value of the temperature beyond which ablation occurs. [45]

Fig. 15b-c show that increasing the repetition rate from 10 MHz to 1.6 GHz reduced the temperature of the surrounding irradiated regions because less laser energy is lost to heat diffusion. Moreover, the authors found from their simulation that the ablation efficiency remains constant if the pulses energy is reduced and, at the same time, the number of pulses inside the burst is increased. In this respect, the shielding effect by ablation-induced plasma will prevent efficient ablation if the repetition rate is increased at constant energy [44].

Several studies have been conducted on burst mode laser ablation with time delay between pulses inside burst long enough to reasonably hypothesize a negligible plasma shielding. Hu et al. [33] focused their study on burst with intra-burst delay of 20 ns, long enough to avoid plasma shielding. On copper target, using burst of 5 pulses with pulse duration of 10 ps and intra-burst time delay of 20 ns, the ablation depth per pulse increases in nonlinear way from the first to the fifth pulse. This trend was ascribed to heating effect, or energy accumulation between pulses. In fact, when the second pulse of the burst impinges on the sample 20 ns after the previous one, it finds the electrons and lattice at the surface in thermal equilibrium at already about 1000 K allowing a larger ablation depth with respect the first pulse.

Using bursts of 10 ps pulses ($\lambda = 1064$ nm) with same intra-burst time delay of 20 ns, Knappe et al. [8] proved that it was possible to increase the ablation rate (amount of ablated volume per minute) with respect to the single pulse case. The ablation rate was evaluated after laser milling of squared areas of 2×2 mm². The same average power was used for burst mode and single pulse in order to investigate the effect of the energy distribution among pulses. The results showed that splitting the pristine pulse energy in groups of pulses (burst) allowed scaling the ablation rate of several material, like stainless steel (Fig. 16), silicon and tungsten. Moreover, it was found that the higher the number of pulses in the burst, the higher was the ablation rate. Nevertheless, the authors suggested that a maximum useful number of pulses exists beyond which heat accumulation is detrimental to the ablation rate.

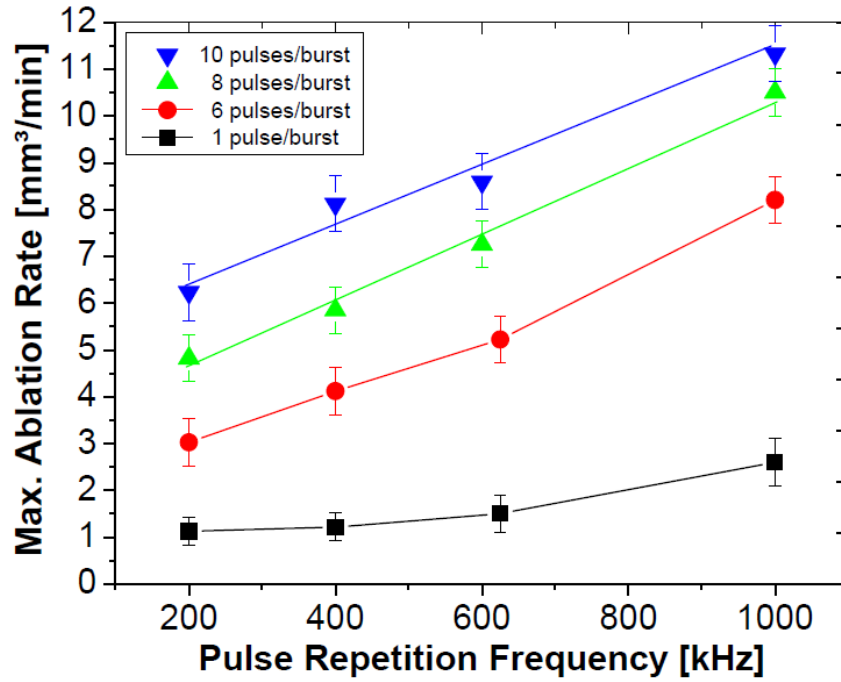


Fig. 16 Maximum ablation rate versus the pulse repetition rate for stainless steel target. The black point (1 pulse/burst) represent the case of pristine pulses of 10 ps which are split in sub-pulses delayed of 20 ns. The average power is kept constant at 50W. [8]

For intra-burst delay shorter than 20 ns, Förster et al. [46] found that the shielding effect cannot be neglected. They studied the ablation of copper by bursts of two and three laser pulses with 532 nm wavelength, 10 ps pulse duration and 12.2 ns of intra-burst delay using shadowgraphic experiments to investigate ablation mechanisms and dynamics. The results revealed that the second pulse was shielded by the material ablated by the first pulse in agreement with previous studies with double pulses, while the third pulse of same energy with respect to the previous ones, induced further ablation (as shown in Fig. 13). The shadowgraphic pictures of the ablation process, with exposure times of 10 ns, showed that several nanoseconds after the second pulse, an intense light emission was observed above the dense cloud. It was ascribed to absorption of the second pulse by the ablative cloud that induced heating of the plasma followed by radiative emission. Then, an increase of pressure caused a re-deposition on the target of part of the material contained in the ablation cloud. However, the third pulse induced a second ablation cloud as reported in Fig. 17, 40 ns after the first pulse. The cloud resulted larger than the previous one thus explaining why the material ablated with bursts of three pulses was larger than the single pulse. The authors ascribed this result to a reduction of the ablation threshold, so-called incubation,

together with altered optical properties of the surface such as higher absorptivity.

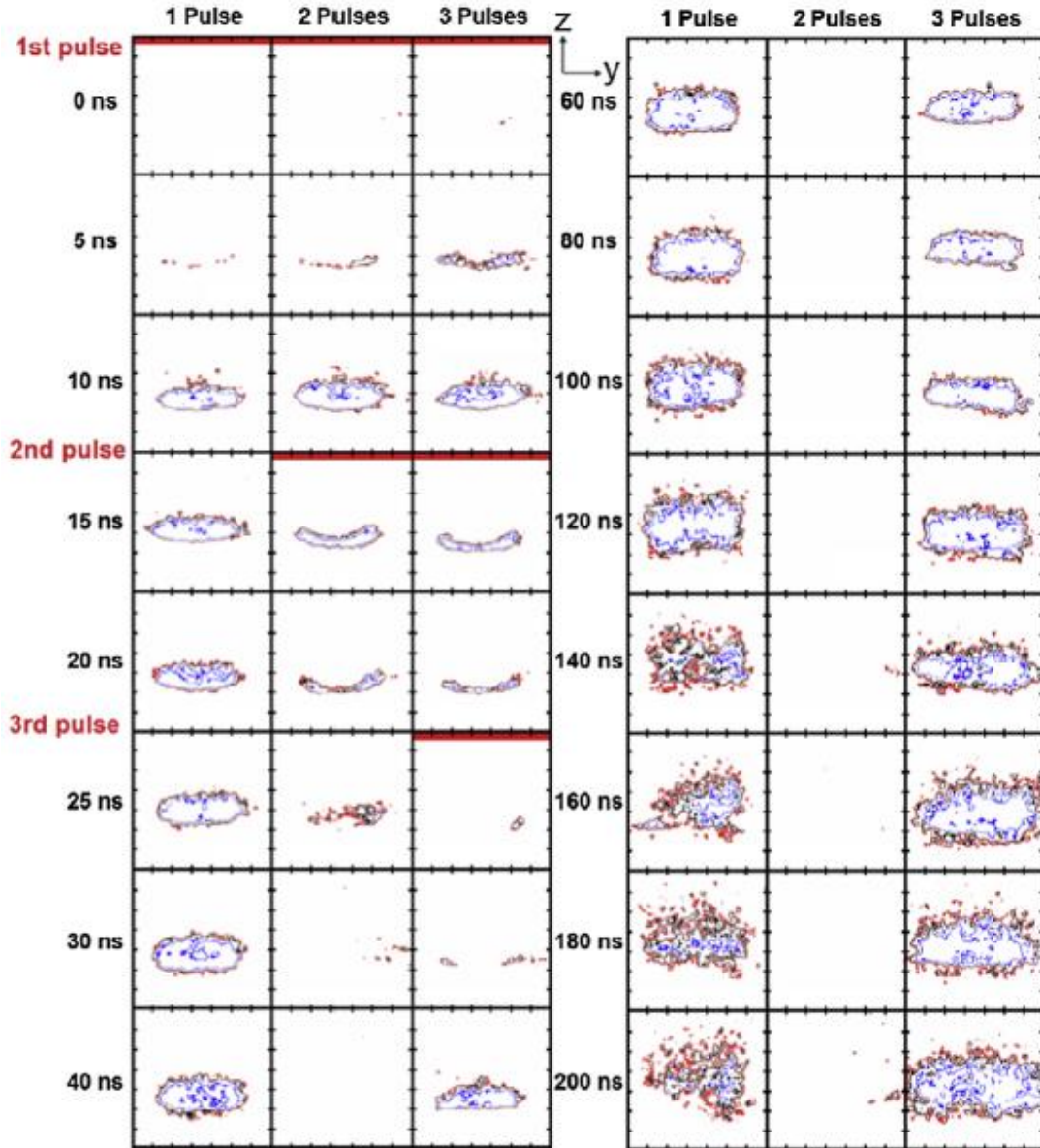


Fig. 17 Processed shadow photographs of single pulse and of burst with two and three pulses to highlight the contours of the ablation clouds. The intra-burst delay among the pulses is 12.2 ns. The red lines indicate the time of applying a second pulse and a third pulse, respectively while the tick marks along the frames correspond to 10 μm in length. [46]

Similar results with bursts of three pulses with delay of 12.2 ns were achieved by Neuenschwander et al. [7] on copper, as shown in Fig. 18a. This plot reports the specific removal rate (as the authors named the removal

efficiency) as a function of the pulse fluence for different burst configurations with fixed time delay (12 ns) between pulses. The specific removal rate was evaluated from milling process of squared areas. From Fig. 18a, bursts with 3 and 8 pulses produced a higher removal rate than single pulses at the optimum value of the pulse fluence. On the other hand, same experiments on stainless steel showed different results (Fig. 18b). In this case, the removal rate with single pulses at optimum fluence was always greater than the burst mode. Nevertheless, for pulse fluences above this optimum value, the removal rate of single pulse decreased because a part of the energy was wasted in heat accumulation and the burst mode resulted more efficient. This was more evident with the increase of the number of pulses in the burst, as shown in Fig. 18b.

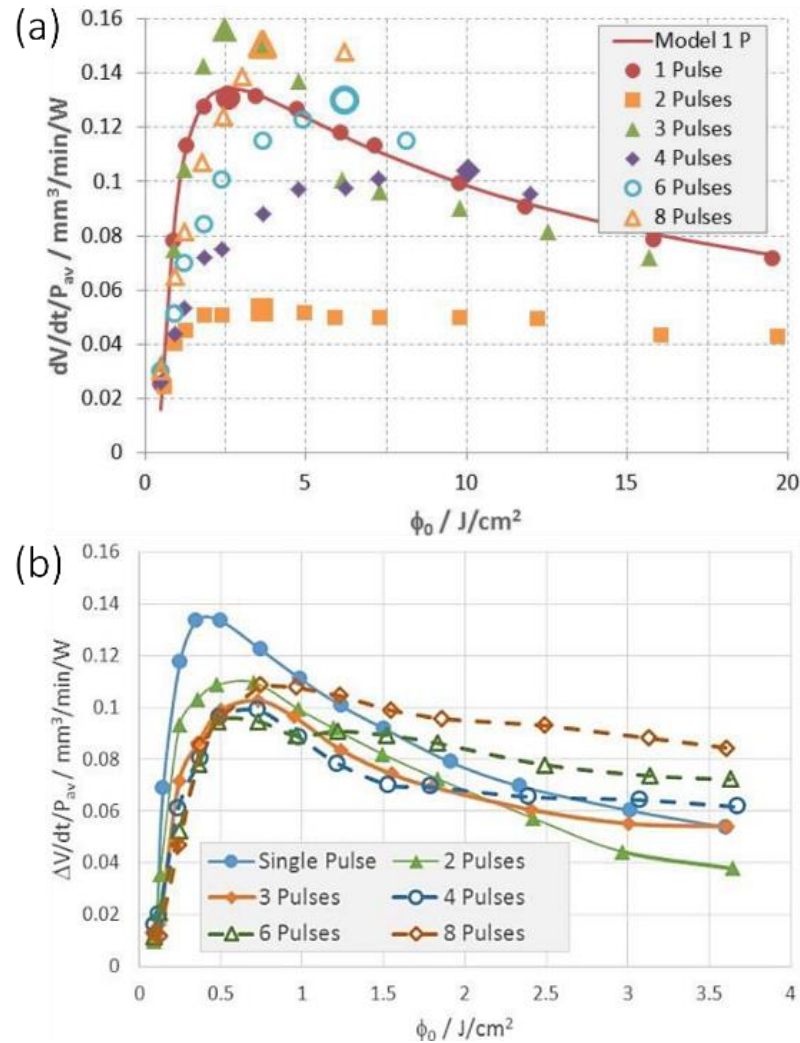


Fig. 18 Specific removal rate for burst with fixed time delay at 12 ns and variable number of pulses from 1 to 8 pulses for (a) copper and (b) stainless steel. The laser wavelength is 1064 nm, the pulse duration is 10 ps and the burst repetition rate is 200 kHz. [7]

A theoretically study on the ablation process with bursts of 100 femtosecond laser pulses with shorter time delays was presented by Zhang et al. [47]. The two-temperature model was used to simulate the irradiation of a thin gold film with 10 bursts. The phase changes, such as melting and evaporation, were considered and integrated in the model. Fig. 19a-b show the simulated evolution of the lattice temperature in case of bursts with three pulses delayed by 100 ps. The work investigated the effects of the time delay in the range 50 ps – 10 ns and of the number of pulses per burst, from 1 to 15, on the phase change. The simulation results showed that pulse splitting reduces the maximum lattice temperature (Fig. 19c) while slightly increases the melting depth (Fig. 19d). Similar trends were obtained by increasing the time delay between pulses inside the burst. Here, a reduction of the maximum temperature and increment of the melting depth for pulse fluence greater than 0.026 J/cm² was found. Thus, they concluded that a higher number of pulses per burst was preferable to obtain deeper melting depth and lower temperature.

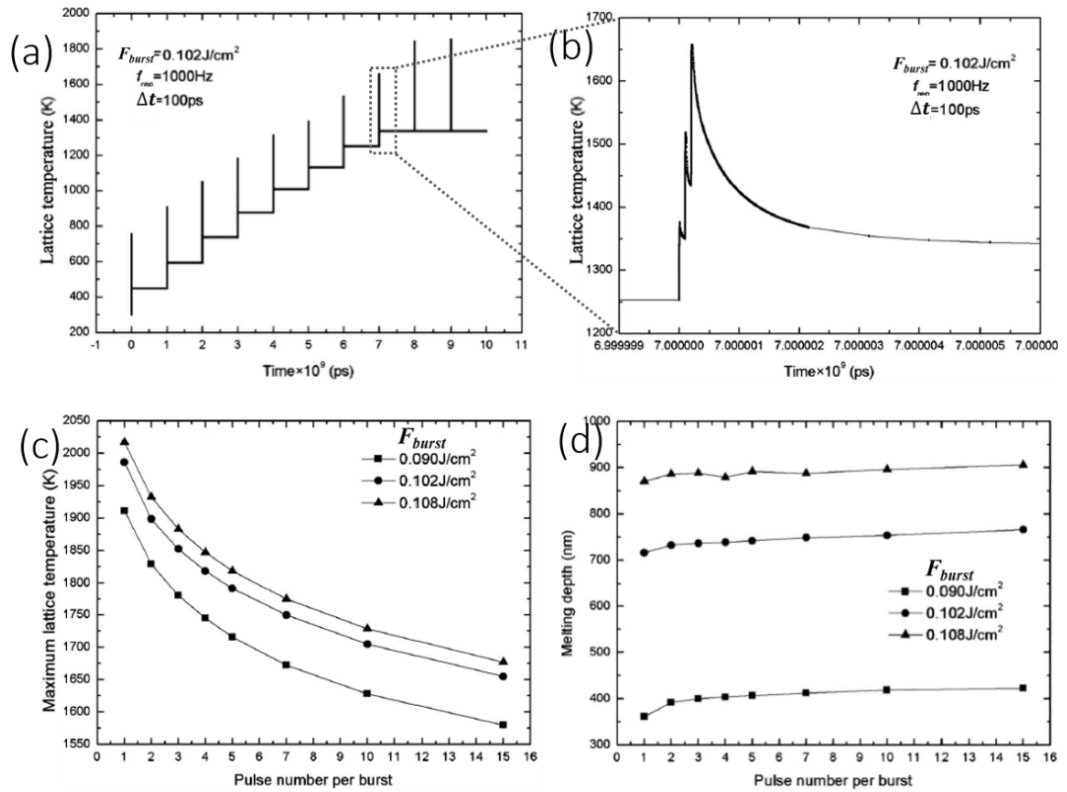


Fig. 19 (a) Evolution of the surface lattice temperature of a thin gold film caused by 10 bursts made of three 100 fs pulses with time delay of 100 ps. (b) Zoomed view of the 8th burst. (c) Effect of the number of pulses inside the burst on the maximum lattice temperature while the burst total fluence (F_{burst}) is fixed at values of 0.090, 0.102 and 0.108 J/cm². The bursts number, the intra-burst delay and burst repetition rate are fixed at 10, 100

ps and 10 kHz, respectively. (d) Plot of the melting depth as a function of the number of pulses per burst, in the same condition of (c). [47]

Chapter 3

Laser induced periodic surface structure

Surface functionalization by laser micromachining has gained considerable attention in the last decades and the femtosecond laser use dominates these processes. Chemical, tribological, optical properties of surfaces can be tailored by laser texturing finding application in several fields, from automotive and aerospace to biomedical devices. Some properties derive from the surface structures of different shapes and sizes artificially created by the laser texturing process. Structures with dimensions of the same size or bigger than the focused beam spot can be fabricated by direct laser ablation [48]. Therefore, the size of these features is typically from a few micrometres to tens of micrometres. Using ultrashort laser pulses, it is also possible to induce sub-micrometric surface structures, thus smaller than the focal spot. Such structures are called LIPSSs, laser-induced periodic surface structures [49] which have attracted much interest from the scientific community in the last years.

In this chapter, a brief review on the physical mechanisms that are believed to be behind the formation of the LIPSS will be given, together with a classification of the LIPSS according to their size and orientation and a discussion on which process parameters influence their morphology.

3.1 LIPSS classification

LIPSSs were observed for the first time in 1965 by Birnbaum et al. [50] on germanium samples in the form of a regular system of parallel straight lines with period of approximately $2 \cdot 10^{-4}$ cm, using a ruby laser. These first LIPSSs were characterized by a single direction of periodicity orthogonal to the surface undulation (succession of crests and troughs). Such periodic structures will be labelled as one dimensional LIPSS (1D-LIPSS). In general, LIPSS appear as periodic ripples or as periodic surface corrugations. Their surface can be smooth or covered with nanostructures/nanoparticles when they are induced by femtosecond pulses [51]. According to the spatial periodicity Λ , fs-LIPSS or FLIPSS are classified into low spatial frequency LIPSS (LSFL), with Λ slightly lower than the laser wavelength ($\lambda/2 \leq \Lambda \leq \lambda$), and high spatial frequency LIPSS (HSFL) for lower spatial periodicity

($\Lambda < \lambda/2$), as shown in Fig. 20 [49]. A further classification for the LSFL concerns their orientation which can be perpendicular (\perp) or parallel (\parallel) to the electric field polarization vector of the laser beam. LSFL are usually oriented perpendicular for materials with strong absorption such as semiconductors and metals. While for dielectrics, LSFL are typically oriented parallel to the laser beam polarization (Fig. 20b). The HSFL manifest in two different forms as regard the depth-to-period aspect ratio $A = \Delta z / \Lambda_{\text{HSFL}}$, with Δz the ripples depth, in deep ($A > 1$) and shallow ($A < 1$) HSFL.

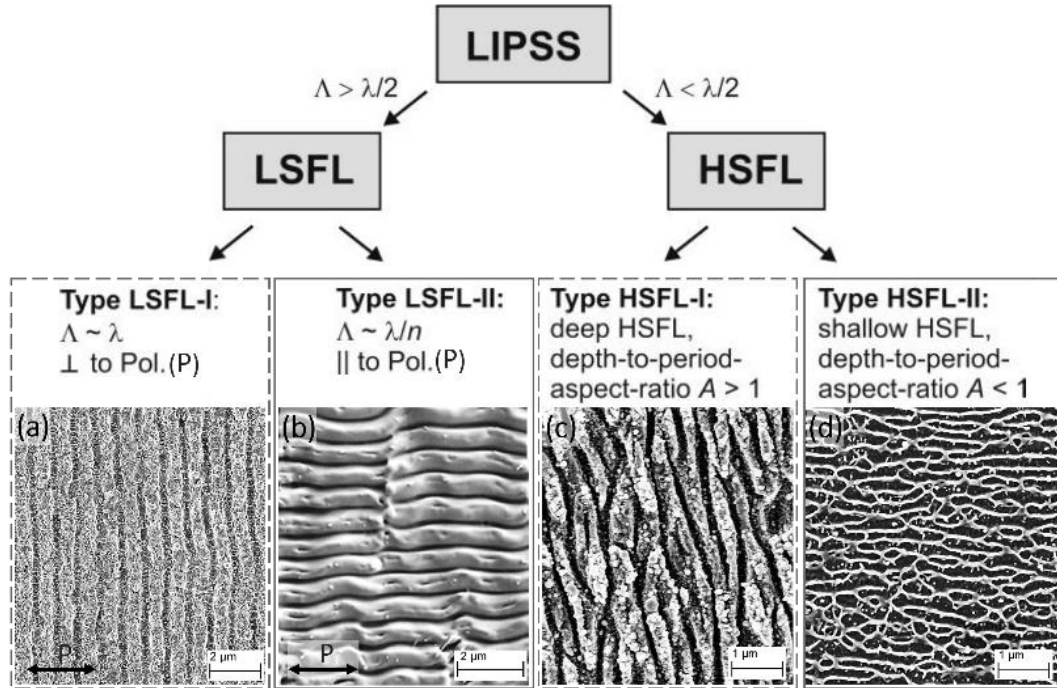


Fig. 20 Classification of the fs-laser-induced periodic surface structures [49]. (a, c, d) SEM images of produced LIPSSs on stainless steel using a 1030-nm fs-laser source under different experimental conditions. (b) SEM image of LIPSS induced on fused silica by 10 laser pulses with pulse duration of 40-fs and central wavelength of 800 nm [52]. The double arrow indicates the polarization on the laser beam.

The polarization of the laser beam not only affects the LIPSS orientation but also their periodicity. This has been verified for non-normal incidence of the laser beam onto the target surface and using two different linearly polarized light, p- and s-polarization, i.e. with polarization direction lying in the plane of incidence or perpendicular, respectively.

The largest number of theoretical and experimental studies on LIPSS have focused on the generation of one-dimensional periodic structure (1D-LIPSS).

Nevertheless, an increasing number of works on two-dimensional periodic structure (2D-LIPSS), characterized by more directions of periodicity in submicron regime, proves the ceaseless research interest for new functional surfaces, bio-inspired to nature [53]. In fact, the generation of structures with novel morphologies with more than one axis of symmetry could in principle enable novel surface functionalities. However, before moving to the 2D-LIPSS, it is important to highlight which process parameters have a bearing or vary the morphology of 1D-LIPSS.

3.2 Parameters that influence the LIPSS formation

The LIPSS topology is affected by irradiation parameters, such as laser wavelength, angle of incident, polarization, number of pulses and laser fluence, by environmental conditions, like pressure and by material properties, as permittivity, temperature and surface roughness. Changes of these parameters produce LIPSS of different morphology (i.e. smooth or with nano-protrusions), period, ripple depth, orientation or profile.

It has been highlighted that a fine control of process parameters like fluence, pulse overlapping, number of scans, etc., determine movements of the surface material with the consequence to vary the structure morphology. In the following, the influence of each process parameter will be discussed.

3.2.1 Laser wavelength, λ

LSFL periodicity has been found to be proportional to the laser wavelength, λ , as shown in Fig. 21 for stainless steel target. It has been estimated by [54] that:

$$3.1 \quad \Lambda_{\text{LSFL}} = \frac{\lambda}{\text{Re}(\eta)}$$

where $\text{Re}(\eta)$ is the real part of the effective refractive index of the metal-dielectric interface. This equation comes from the surface plasmon polaritons (SPP) model which represents one of the first physical models trying to explain the formation of the LIPSS. This model will be discussed in detail in the following section. This relation has been further proved by Li et al [55] that varied the ripples periodicity from about 300 to 1600 nm (see Fig. 21) by tuning the laser wavelength from 400 to 2200 nm using an optical parametric amplifier (OPA).

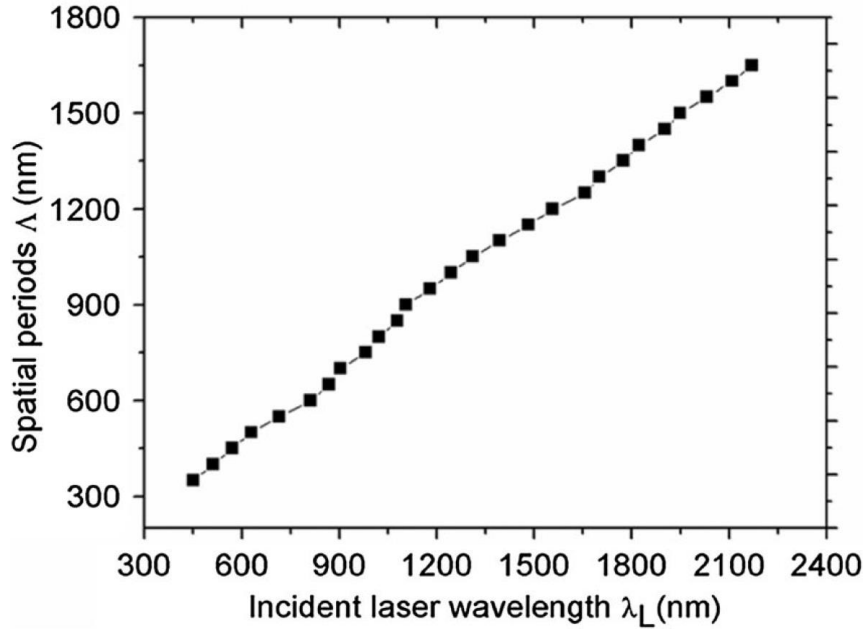


Fig. 21 Spatial period of the LSFL on stainless steel (316L) target as a function of the incident wavelength. [55]

3.2.2 Angle of incidence, ϑ

The ripples periodicity changes also with the angle of incidence of the laser beam with respect to the target surface. This relationship was theoretically predicted by Bonch-Bruевич et al. [54] for both p- and s- polarized light based on the concept of interference between incident laser pulses and SPP. The estimated periodicities as a function of the incident angle of the laser beam ϑ with respect to the normal direction at the target surface are:

$$3.2 \quad \Lambda_{p\text{-polarization}} = \frac{\lambda}{\text{Re}(\eta) \pm \sin\vartheta}$$

$$3.3 \quad \Lambda_{s\text{-polarization}} = \frac{\lambda}{(\text{Re}(\eta)^2 - \sin^2\vartheta)^{1/2}}$$

For strong absorbing and plasmonic materials ($\text{Re}(\epsilon) \ll -1$) the previous equations are simplified into:

$$3.4 \quad \Lambda_{p\text{-polarization}} \sim \frac{\lambda}{1 \pm \sin\vartheta}$$

$$3.5 \quad \Lambda_{s\text{-polarization}} \sim \frac{\lambda}{\cos\vartheta}$$

as theoretically predicted in the Sipe theory [56]. Experimental results have been reported in several studies [49,57]. Nurnberger et al. [57] tuned the spatial period of the ripples produced on stainless steel targets from ~500 nm to 4000 nm by changing the incidence angle from 0° to 70° using p-polarized

light. Their results are shown in Fig. 22, where the solid lines correspond to the theoretical values estimated by Eqs. 3.1 and 3.2. A good agreement with the experimental data was noticed.

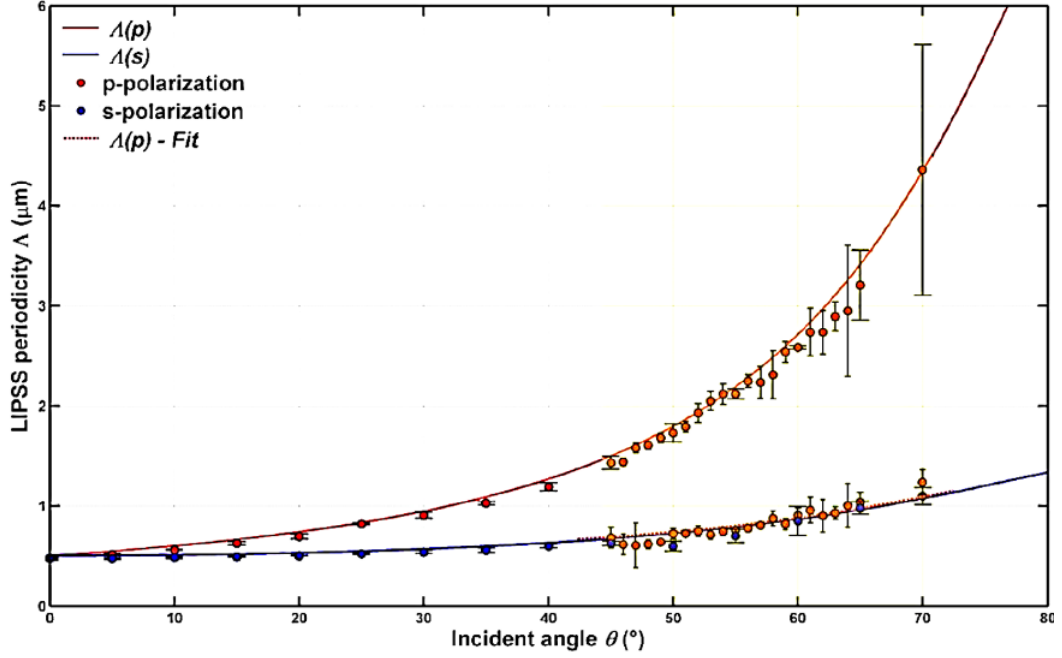


Fig. 22 Angular dependence of the LIPSS period by nanosecond p- and s-polarized laser pulses ($\lambda=532$ nm) on stainless steel. [57]

It was further found that getting away from normal incidence conditions ($\vartheta = 0^\circ$), the ripples profile becomes asymmetric. In particular, each ripple exhibited different slopes at the leading and at the trailing edges. Such an asymmetric profile makes the ripples resemble that of a blazed grating [58].

3.2.3 Fluence, F

LIPSS formation occurs in a certain laser fluence range close to the material damage threshold. When the laser fluence is above that range, the LIPSS are completely cancelled due to the stronger ablative regime. The effect of fluence on LIPSS spacing at normal incidence was investigated for different materials. Bonse et al [59], for example, investigated the LIPSS formation on titanium surface by fs-laser pulses irradiation. They observed that LIPSS periodicity increased with increasing fluence for a given number of pulses (Fig. 25). The LIPSS were characterized by a period always shorter than the laser wavelength ($\Lambda/\lambda < 1$). At low fluence, only HSFL parallel to the radiation electric field were observed, while at higher fluence LSFL appeared which were oriented perpendicularly to the beam polarization. Therefore, it

was concluded that the fluence plays a key role in the formation of the LIPSS type and their spacing.

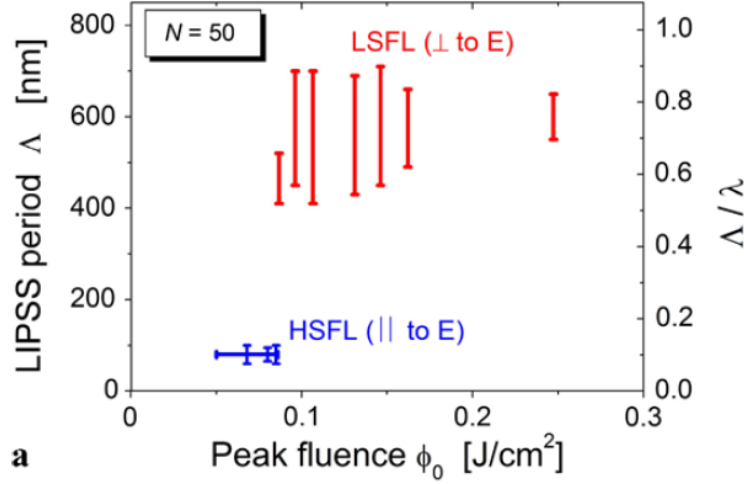


Fig. 23 LIPSS spatial period as a function of the peak laser fluence for 50 laser pulses per spot. The target material is titanium irradiated by a fs-laser pulses at 800 nm in wavelength. [59]

Okamuro et al. [60] studied the dependency of LSFL formation on fluence for Al, Au, Cu, Mo, Ti, Pt and W targets irradiated with fs-laser pulses. For all the investigated metals, it was found that the periodicity increased with increasing fluence (Fig. 24), although the range of laser fluence in which the structures are formed differs from metal to metal. Such an increase of the LIPSS period with the laser fluence was in agreement with the theoretical model proposed by Sakabe et al. [61] for the fluence range $F_{10nm} < F_{laser} < F_M$, where F_{10nm} is the fluence value ablating a 10 nm thick layer while F_M represents the upper limit of fluence at which the periodic structures are formed. According to this model, the LIPSS period corresponds to the wavelengths of the induced surface plasma waves λ_{SP} , estimated by the following equation:

$$3.6 \quad \frac{\lambda_{SP}}{\lambda_{laser}} = \left[1 + \left(\frac{\omega_p^2}{\omega_{laser}^2} - 2 \right)^{-1} \right]^{-1/2}$$

where ω_p is the plasma wave (plasmon) expressed by ($\omega_p = \sqrt{4\pi e^2 n_{es}/m}$), e and m are the electron charge and mass, and n_{es} is the surface electron density which is related to the laser fluence, $n_{es} \propto \sqrt{F_{laser}}$.

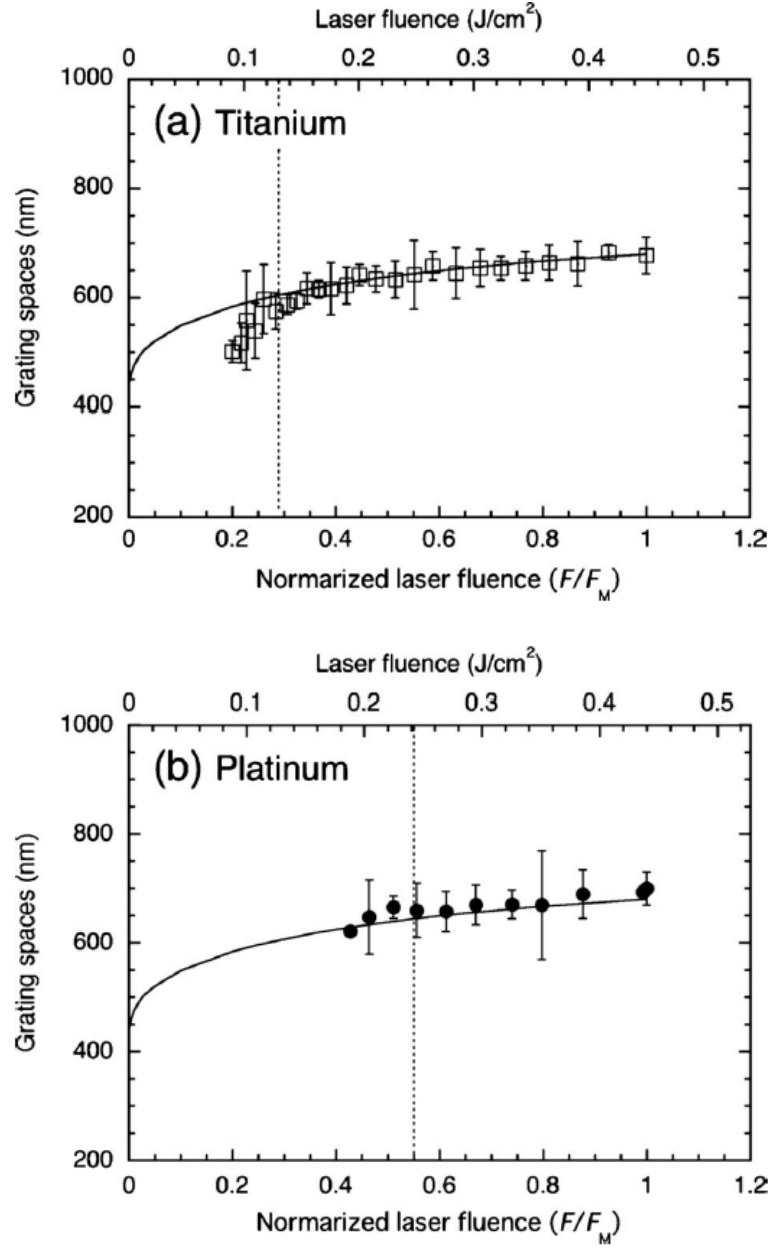


Fig. 24 Grating spaces of the periodic structure induced by fs-laser pulses on (a) titanium and (b) platinum, as a function of the laser fluence. Laser fluence is normalized by the upper limit of the laser fluence F_M still producing periodic structures. Solid lines represent the evaluated period by Sakabe's model (Eq. 3.6). Dotted lines show the laser fluence for the ablation rate of 10 nm/pulse. [60]

3.2.4 Number of pulses and/or number of scans, N

Fig. 25 shows the dependence of the LIPSS period observed in the central area of the irradiated spot on the target surface as a function of number of laser pulses for a fixed peak fluence of $F = 0.16 \text{ J/cm}^2$ [59] on titanium

surface. The LSFL period decreases from 750 ± 50 nm to 520 ± 50 nm passing from $N = 1$ to $N = 1000$ number of pulses impinging on the same spot (point processing mode) as plotted in Fig. 25, for ripples created in a central area of $50 \times 50 \mu\text{m}^2$. This trend has been also confirmed by other works [62–64]. Hence, the number of pulses impinging on the same spot can be considered as another key parameter affecting the LIPSS morphology.

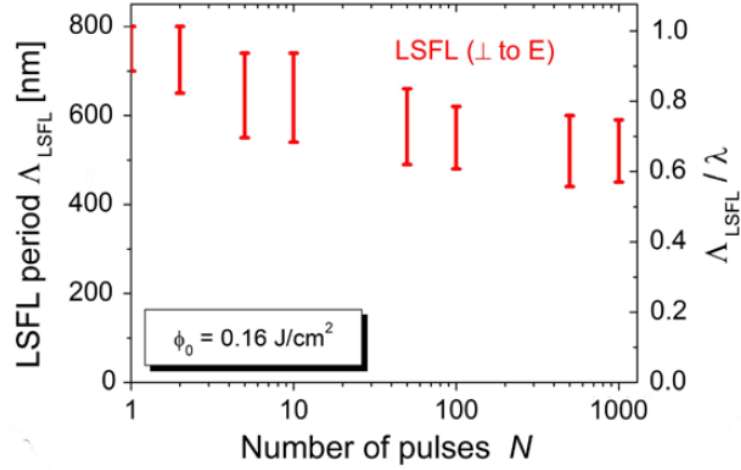


Fig. 25 LIPSS spatial period as a function of the number of laser pulses per spot at fixed peak laser fluence of 0.16 J/cm^2 . The target material is titanium irradiated by fs-laser pulses at 800 nm in wavelength. [59]

Even more relevant is the combination of number of pulses and laser fluence as reported by Hermens et al. [65] and shown in Fig. 26.

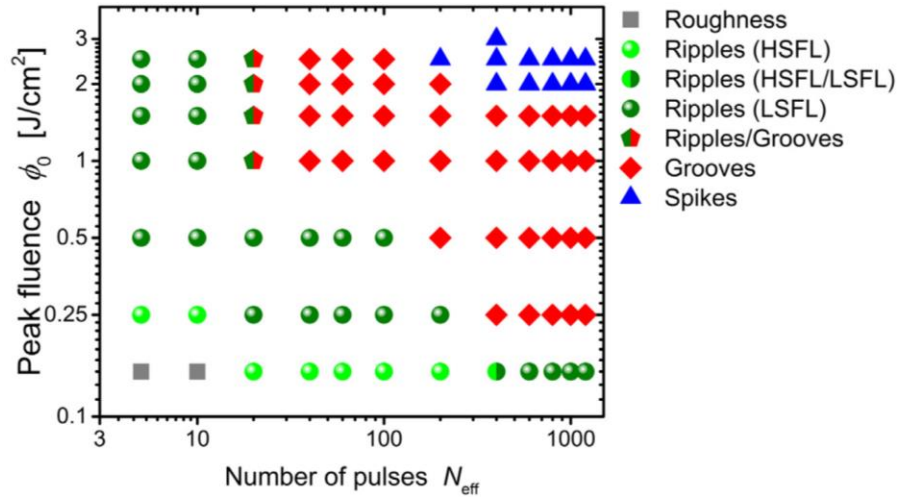


Fig. 26 Map of the surface morphologies induced on steel surface by fs-laser pulses irradiation along scanning lines operating at different number of pulses and peak laser fluence. Processing conditions: $\lambda = 790 \text{ nm}$, $\tau = 30 \text{ fs}$, $f = 1 \text{ kHz}$. [65].

Here, the experimental study addresses LIPSS induced on steel surfaces by fs-laser pulses over large areas, by means of the laser beam scanning along lines (scanning mode). N_{eff} represents the effective number of laser pulses per spot (this quantity will be better explained in chapter 5). It can be noticed that the combination of number of pulses and laser fluence influences the type of induced structures. For very low number of pulses and laser fluence only an increase of the surface roughness was observed, while spikes were found at higher values of fluence and pulses. Between these two irradiation conditions, LIPSS were generated. It is clear that the formation of LIPSS (both HSFL and LSFL) at higher fluence requires a lower pulse number. In addition, the coexistence of more structures, such as HSFL and LSFL, is possible. In other words, the transition from HSFL to LSFL is not sharp and under specific irradiation conditions both are visible.

Several works report the formation of HSFL from LSFL when increasing the number of pulses [66,67]. In [66], a transition was observed from LSFL with spatial period of 630 nm generated by irradiating a stainless steel target with $N = 100$ pulses ($\tau = 164$ fs, $\lambda = 780$ nm) to HSFL with spatial period of about 310 nm, when the number of pulses was increased to $N = 250$, with same pulse energy of 1 mJ. The induced HSFL were characterized by an orientation parallel to the LSFL (i.e. orthogonal to laser beam polarization). Anyway, both LSFL and HSFL appeared together between 250 and 500 pulses, as reported in Fig. 27. Here, at the laser fluence of 0.07 J/cm^2 (Fig. 27a) a change of the ripple period from ~ 560 to ~ 280 nm was observed in the transition from 300 to 500 pulses. Periodic nanostructures appeared on top of the LSFL. Hence, it suggested that HSFL result from the splitting of the already formed LSFL since they had only half of the spatial period of the former LSFL, as shown in the area highlighted in Fig. 27b. This phenomenon extended to the whole surface after 500 pulses at $F = 0.07 \text{ J/cm}^2$ and it was observed only for laser fluences in the range $0.07\text{--}0.13 \text{ J/cm}^2$.

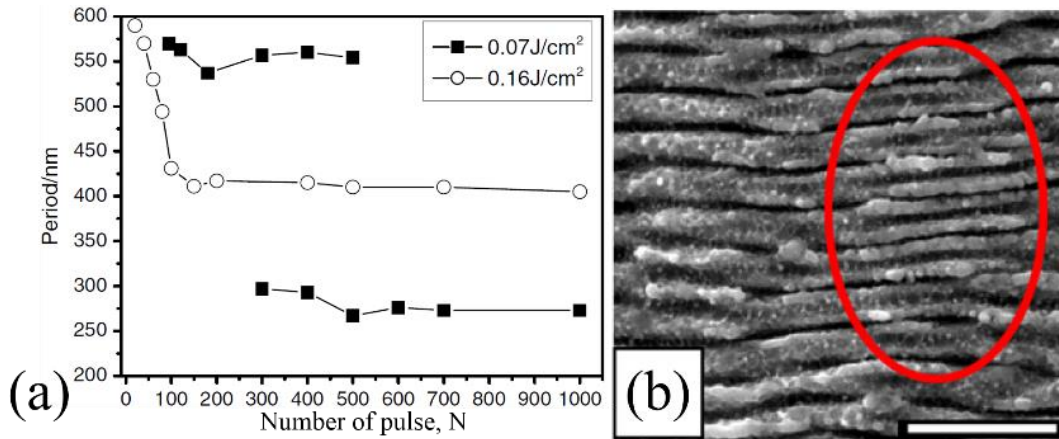


Fig. 27 (a) Ripple period as a function of the number of pulses N , on stainless steel surface irradiated in point processing mode by laser pulses at a central wavelength of 800 nm, pulse duration of 50 fs and pulse energy of 3.5 mJ. (b) SEM image of the surface morphology generated at fluence of 0.07 J/cm^2 with $N = 400$ pulses. The red line highlights the area where the HSFL are visible. The scale bar is $2 \mu\text{m}$. [66]

The number of pulses per spot in scanning mode can be varied by changing the scanning line speed or the laser repetition rate. An increase of the number of scans (or number of loops) has indeed the same effect of a higher number of pulses, as reported by Guan et al. [68] for a Mg alloy.

3.2.5 Polarization, P

As stated previously, the polarization of the laser beam determines the LIPSS orientation and it assumes great relevance when the laser beam impacts the sample surface in non-orthogonal incidence. Nevertheless, for low value of fluence, Romer et al. [69] observed that ripples emerged first along the grain boundaries on the steel surface. Moreover, the ripples orientation changed from grain to grain. Subsequent works have proved the influence of crystal orientation on the formation of LIPSS [57,70]. Therefore, it was suggested that the LIPSS orientation depends also on the orientation of crystalline grains and may change for each individual grain because grain boundaries do not allow the SPP propagation among adjacent grains.

However, the key role of the beam polarization on the LSFL formation was recently remarked by Skoulas et al. [53], who used cylindrical vortex (CV) femtosecond laser beam generated by an s-waveplate, which transforms a linearly polarized Gaussian beam in a CV beam with radial/azimuthal polarization (Fig. 28). They demonstrated that for a radial and azimuthal polarization, the LSFL strictly oriented orthogonally to the orientation of the local (linear) polarization direction of the CV laser beam.

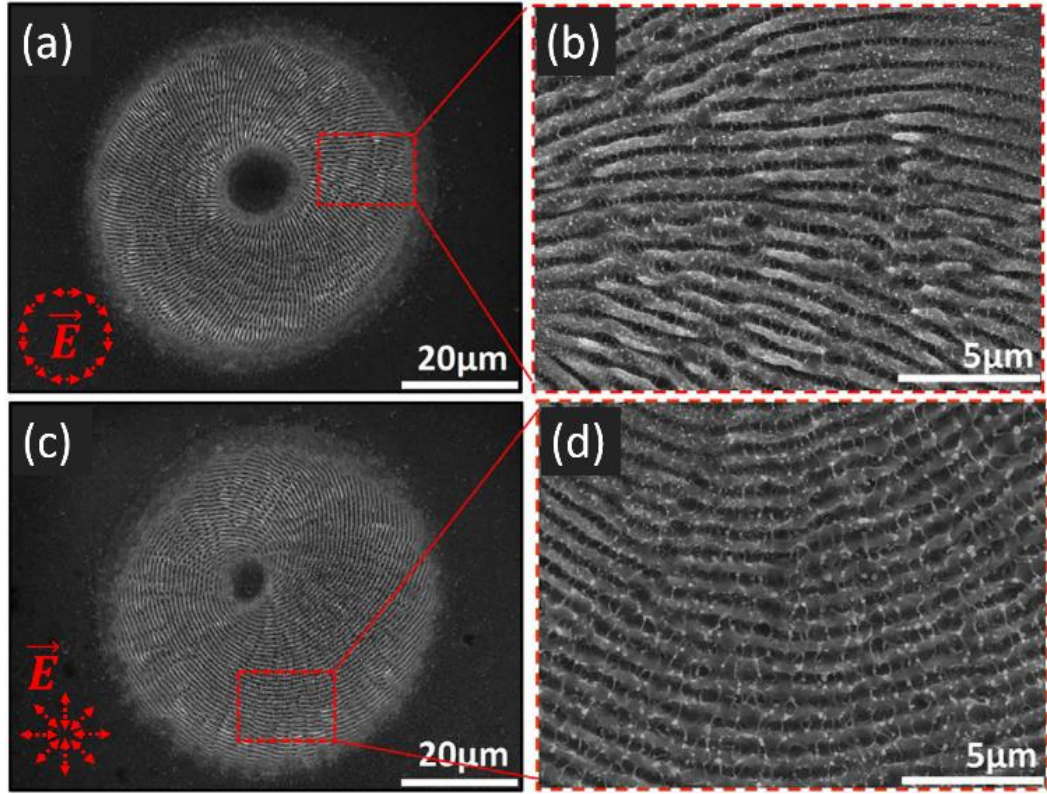


Fig. 28 SEM images of LIPSS generated on Ni surfaces upon irradiation with azimuthal (a-b) and radial (c-d) polarization beam, using 100 pulses with $F = 0.24 \text{ J/cm}^2$. [53]

The effect of polarization was also studied by Gregorcic et al. [71]. They first fabricated LIPSS on a surface and then re-irradiated that area with pulses of 30 ps (FWHM) and repetition rate of 50 kHz by rotating the polarization of 45° or 90° . A corresponding rotation of the ripples was found. After few pulses, the pristine LIPSS were erased and new LIPSS with orientation defined by the polarization of the last pulses were formed. Hence, it is possible to rotate the prior LIPSS direction by irradiating with linear polarized pulses along the desired direction. Hashida et al. [72] demonstrated that it is possible to control the LIPSS orientation on titanium surface, using a double-pulse beam with time delay of 0 ps. The polarizations of the two pulses were orthogonal with fluences F_1 and F_2 . The LIPSS orientations varied from 0° to -45° as the laser fluences ratio F_2/F_1 passed from 0 to 1, as shown in Fig. 29. It was found that the alignment of the LIPSS generated by the two perpendicularly polarized pulses is determined by the following relation:

$$3.7 \quad \vartheta = \tan^{-1} \left(\frac{F_2^2}{F_1^2} \right) = \tan^{-1} \left(\frac{E_2^4}{E_1^4} \right)$$

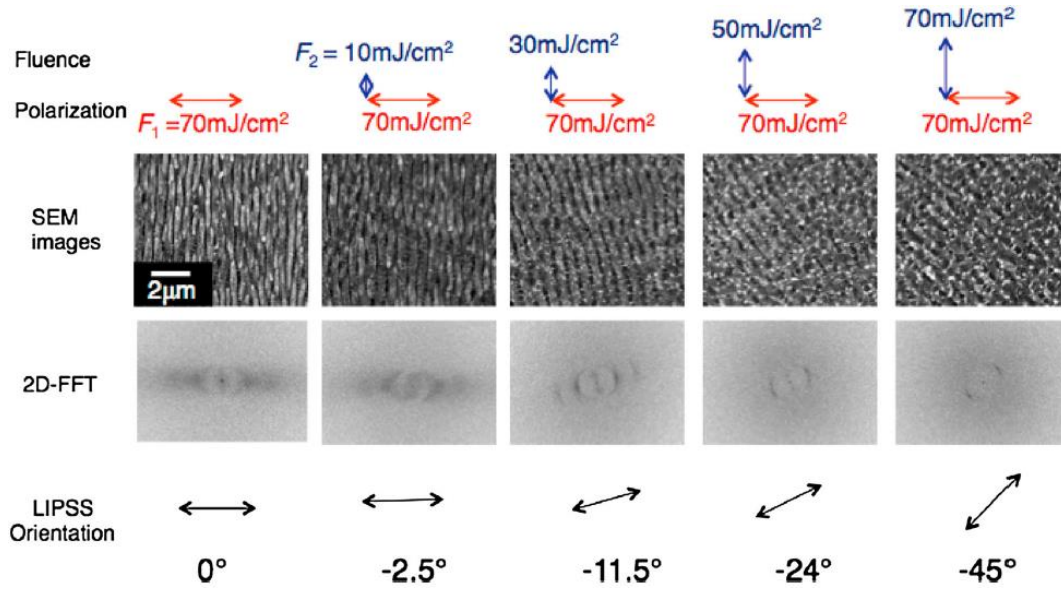


Fig. 29 Dependence of the LIPSS orientation as a function of the laser fluence of the pulse F_2 for fixed fluence of $F_1 = 70 \text{ mJ/cm}^2$. The two pulses ($\lambda = 805 \text{ nm}$, $\tau = 40 \text{ fs}$) have orthogonal polarization and time delay of 0 fs . [72]

The main difference between the last two works is the time delay Δt between the two pulses with different linear polarizations. In Hashida's work it is on the millisecond time scale while in Gregorcic's one the two pulses arrived on the target at 0 fs delay. In other word, with $\Delta t = 0 \text{ fs}$ both pulses are involved in the LIPSS formation at the same moment, while in the other case each pulse acts independently. This indicates that the couple of parameters polarization – interpulse time delay in multi pulse irradiation, has a crucial influence the LIPSS morphology.

3.2.6 Interpulse time delay, Δt

The time delay between consecutive pulses is a relevant physical parameter because during ultrafast laser pulse – matter interaction different phenomena occur at different timescales. For instance, in case of metals, if a subsequent laser pulse hits the target after several hundred nanoseconds from the first pulse, the resulting periodic structure morphology is expected to be given by the simple superposition of the surface modifications produced by each independent pulse [71]. On the other hand, if the time delay between pulses is in the picosecond range, considering that the temporal and spatial evolution of the electron/lattice temperatures are typically on the same timescale [73], the subsequent pulse finds the material still in a transient state. Therefore, the dynamic of formation of the periodic structures is influenced by both pulses at the same time. As a result, different LIPSS may arise depending on the

pulse sequence. Hence, a promising approach to control the LIPSS morphology relies on tailoring the laser energy transfer to the material in the time domain.

Recent studies [72,74,75] on irradiation with double fs-pulses have investigated the influence of time delay up to hundreds of picosecond on the LIPSS formation. Fraggelakis et al. [75] showed the combined effect of interpulse ps-delay and sequence order of cross-polarized double pulses on the final LIPSS morphology. They found that ripples orientation is mostly influenced by the polarization of the second pulse as shown in Fig. 30.

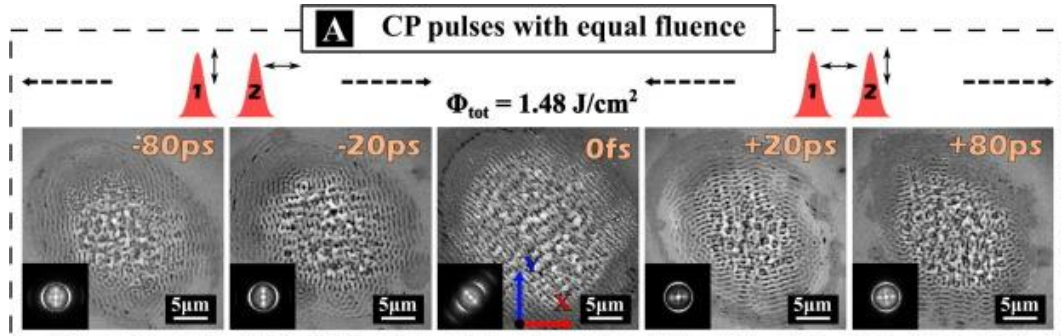


Fig. 30 SEM images of silicon surface after irradiation of double pulses with picosecond time delay. The two pulses have orthogonal linear polarization, called crossed polarized pulses (CP) and equal fluence. [75]

Nevertheless, the strongest imprint of the last pulses was only worth for pulses with equal fluence. The authors investigated also the case with non-equal fluence between the two pulses finding that the most predominant ripples were induced by the pulse with higher fluence, independently of the delay. The latter result highlights how the laser fluence of each pulse has a greater impact than that of the order of arrival of the individual pulses. With regard to the LIPSS morphology, the spatial period on silicon [76] and fused silica [77] decreased with the time delay (in the range from 0 to 40 ps) between the two pulses with equal fluence and polarization. In addition, for fused silica it was observed that also the ripples depth decreased with the time delay [77].

However, while few works have been conducted to investigate the influence on the LIPSS formation and morphology of double pulses, the use of burst with high number of pulses with picosecond delays has not been extensively explored, yet.

Besides the abovementioned parameters, other studies have been reported in literature that addressed the influence of the pulse duration and the ambient pressure on the LIPSS morphology. Nivas et al. [78] showed an increase of

the LIPSS period on silicon by changing the environmental pressure from atmospheric to high vacuum conditions. However, producing LIPSS in controlled atmosphere is uninteresting at industrial level.

3.3 Mechanisms of LIPSS formation

The first hypothesis on the LIPSS formation was proposed by Birnbaum [50] who attributed their formation to a diffraction effect and suggested that the maxima of the electric field intensity removed greater material from the surface forming ripples.

The first real theory on the ripples origin was formulated by Sipe et al. [56] that introduced the term LIPSS in literature. They proposed that the LIPSSs were originated by the interference between the incident laser beam and the scattered electromagnetic waves (SEW) at surface defects (nano-roughness). This phenomenon leads to inhomogeneous absorption of the radiation by the electronic system and consequently to a modulated energy deposition to the lattice system of the material [49]. In particular, the ripples oriented perpendicular to the laser polarization (especially in metals and semiconductors) have been attributed to the excitation of surface plasmon polaritons (SPP) while those parallel to the laser polarization have been ascribed to specific non-propagating electromagnetic modes, the so-called Radiation Remnants (RR) [56].

The Sipe' theory was subsequently combined with a Drude model [79,80] to take into account the optical response of the quasi-free conduction band electrons of the laser excited solids. The improved theory predicted the LIPSS features as a function of the irradiation parameters (wavelength, angle of incidence, polarization direction and laser incident wave vector) and surface parameters (dielectric permittivity and surface roughness). Nevertheless, this theory cannot predict LIPSS with period much smaller than the laser wavelength ($\Lambda < \lambda/2$), which are only observed for femtosecond laser processing. Hence, even though the Sipe-Drude' theory well justified the LSFL, other possible mechanisms have been introduced to explain HSFL. The debate of origin and formation of LIPSS is still ongoing and future investigations are needed to reach a broad LIPSS' theory.

Anyway, second-harmonic generation [80,81] and self-organization [82,83] were proposed as possible mechanisms to explain HSFL.

In the following part, two of the physical mechanisms of LIPSS formation, extensively treated in literature will be briefly described: the interference model and the self-organization model.

3.3.1 Interference model

The basis of this model lies into the modulation of the electron temperature on the irradiated surface. This spatial modulation of the electron heating along the surface is attributed to interaction of the incident laser beam with the surface-scattered electromagnetic wave (SEW). Considering a metallic surface with a small roughness $z \ll \lambda$ and a wave incident at normal direction, with amplitude E_0 , the scattered fields are created due to the surface roughness. The interference between the scattered fields and the incident or refracted field leads to inhomogeneous intensity distribution above and below the surface. A feedback mechanism is triggered, because the inhomogeneous intensity distributions increase the roughness, which in turn increases the SEW. So that, periodic inhomogeneities can grow where the scattered fields, seeded by initial random roughness, are stronger [56,84]. In case of metal-dielectric or metal-air interface, the involved SEW are the excited surface plasmons, called surface plasmon-polariton (SPP) waves. These involve the charge motion in the metal (surface plasmon) and electromagnetic waves in the dielectric or air (polariton) as shown in Fig. 31.

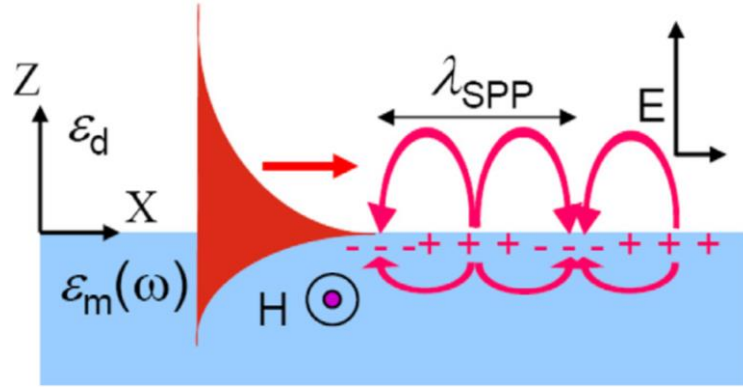


Fig. 31 Schematic representation of the intensity distribution of the electromagnetic field components of a SPP supported by a metal–dielectric interface. [85,86]

The periodicity Λ of the interference pattern is linked to the laser wavelength and the incident angle:

$$3.8 \quad \Lambda = \frac{\lambda}{\text{Re}\left(\sqrt{\frac{\epsilon_m \epsilon_d}{\epsilon_m + \epsilon_d}}\right) \pm \sin \vartheta}$$

and in case metal-air interface ($\epsilon_m = \epsilon$, $\epsilon_d = 1$):

$$3.9 \quad \Lambda = \frac{\lambda}{\text{Re}\left(\sqrt{\frac{\epsilon}{1 + \epsilon}}\right) \pm \sin \vartheta} \approx \lambda \frac{k^2 - n^2 - 1}{k^2 - n^2} \quad (\vartheta=0)$$

where $\epsilon = \sqrt{n + ik}$ is the wavelength-dependent dielectric constant of the material with n the refractive index and k the extinction coefficient. The negative and positive signs correspond to forward and backward scattering, respectively. The spatial period defined by the equation 3.9 corresponds to the electromagnetic field modulation at the interface metal-air. Assuming a periodic absorption of laser energy due to the abovementioned interference conditions, Eq. 3.9 also represents an evaluation of the LIPSS periodicity. Moreover, during the laser irradiation, the optical properties of the material vary. Therefore, for a good agreement between theoretical predictions and experimental data, it is necessary not to neglect those changes during the laser-matter interaction [87]. The Drude model [79,80] takes into account the temporal variations of the optical properties.

However, this model explains the LIPSS formation, their period and orientation only under certain irradiation conditions. The amplitude of the incident electric fields E_0 must be comparable with that of the plasmons E_p , otherwise for $E_0 \gg E_p$, the visibility Γ :

$$3.10 \quad \lim_{\frac{E_p}{E_0} \rightarrow 0} \Gamma = \lim_{\frac{E_p}{E_0} \rightarrow 0} \frac{E_0 E_p}{E_0^2 + E_p^2} = 0$$

tends to zero.

Another condition required by this model to predict ripples formation is related to the frequency and momentum of the incident photons that excite the SPP. In order for a photon to couple with a surface plasmon, the wave vector must increase by:

$$3.11 \quad \Delta k = k_{SP} - k_{ph}$$

where k_{ph} , the x component of the wave vector of the photon, is smaller than the wave vector of the surface plasmon k_{SP} . Hence, the excitation in case of normal incidence is allowed only if other mechanisms are taken into account, such as the surface roughness which can be thought as superposition of many gratings of different periodicities. This allows to match the photon and SPP wave vectors [88,89].

Limitations and contradictions between this model and experimental observations have been highlighted in literature [49].

3.3.2 Self-organization model

In the self-organization model, hydrodynamics takes into account the strong thermodynamic instabilities during the relaxation frame subsequent to laser irradiation. Compared to the previous model, the material surface takes part on the LIPSS formation. A schematic representation of the two models is reported in Fig. 32.

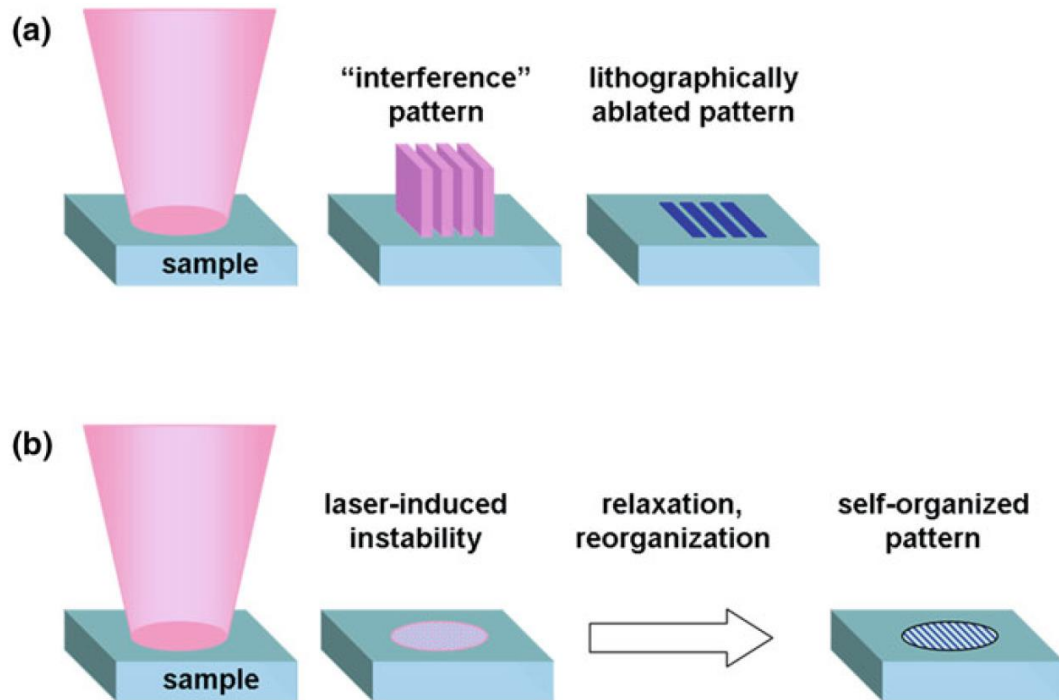


Fig. 32 LIPSS formation according (a) the interference model and (b) the self-organization model. In the first model, the spatially modulated energy deposition ("interference" pattern) induces modulated ablation. In the second model, the femtosecond laser beam induces a high degree of instability at the surface which leads to formation of self-organized patterns during the surface relaxation. [90]

Key concept of hydrodynamic theories is the ripples formation by melting flow generated as a consequent of the irradiated sample surface by laser pulses. This means that the timescale to solidify the molten surface layer is in nanoseconds [91]. Several instability mechanisms have been purposed to induce surface pattern. Here, we mention without going into details the Marangoni instability supported by Tsibidis et al. [92], the recoil-force driven instability by Gurevich et al. [93], the Rayleigh-Taylor instability proved by Birkhoff et al. [94] and the evaporation driven instability treated by Varlamova et al. [90].

Anyhow, each mechanism needs to be triggered by an initial perturbation that provides the seed for the instability.

It is important to underline that the initial perturbations affect locally the lattice temperature. Therefore, these local temperature perturbations of the electron system, which directly couples with photons, may not appear in the lattice system.

In one of the most recent works on self-organization, Sedao et al. [83] ascribed the LIPSS formation to electromagnetic and hydrodynamic mechanisms. The light self-arrangement due to the initial surface nano-roughness, leads to near-field enhancement on roughness centres and to coherent superposition of scattered waves with incident light inducing high periodic energy modulation. Due to thermomechanical conditions, the roughness centres (i.e. nanovoids, nanocavities) are driven to auto-arrangement in periodic structures (LIPSS).

3.4 2D – LIPSS

It is commonly believed that the macroscopic properties of a surface are determined by their micro- and nano- surface structures, which for LIPSS are represented by their aspect ratio, periodicity and symmetry. Therefore, the 2D-LIPSS with more than one symmetry and more periodic directions, represent a significant breakthrough towards the objective of functionalizing a surface through its structuring [53]. Nevertheless, the 2D-LIPSS generation results tricky and the process parameter window remains rather narrow.

In the last years, only few works have been published on 2D-LIPSS. Liu et al. [95] have studied an efficient way to transform the 1D-LIPSS in 2D sub-wavelength structures. Nano-squares and nano-rectangles were fabricated on ZnO crystals by using two-step direct femtosecond laser writing (DFLW) method. First, the nanograting along X axis was induced by laser irradiation with linear polarization along the Y scan direction. Then, the second nanograting along Y axis was fabricated rotating the laser polarization direction by 90°. The final 2D grating (Fig. 33) had an average width less than 40 nm.

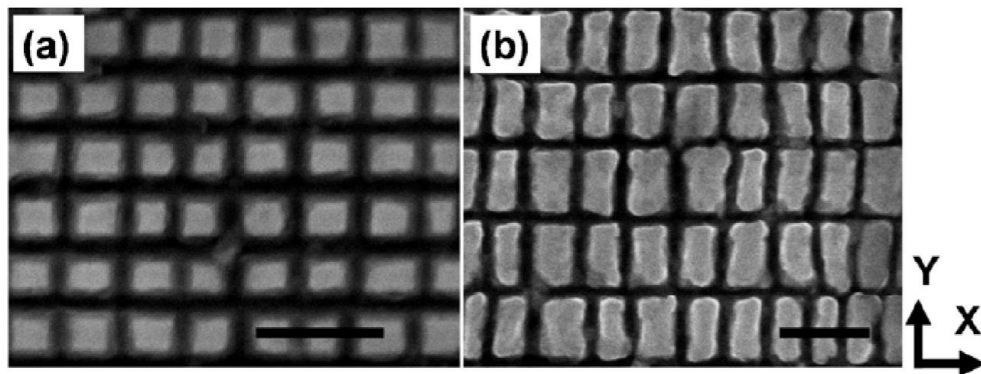


Fig. 33 SEM images of nano-squares (a) and nano-rectangles (b) induced on ZnO with dimensions of $150 \times 150 \text{ nm}^2$ and $150 \times 250 \text{ nm}^2$, respectively. 'X' and 'Y' represent the laser writing directions. The scale bars are 300 nm. The laser parameters were: $\lambda = 800 \text{ nm}$; $\tau = 50 \text{ fs}$; $f = 1 \text{ kHz}$. [95]

Sub-micron squared structures on the same crystal were fabricated by Huang et al. [96] in single step by using a different technique which allowed to employ alternately two linearly polarized laser beams with orthogonal polarizations for spots irradiation on the sample surface (Fig. 34). The ability to generate submicron squared structures by the TBAA (two-beam alternate ablation) technique originates from the spatial and temporal non-interference between the two orthogonally polarized beams. In other words, the effects of the two beams are isolated from each other, so that each beam with specific polarization induces own ripples without influencing the ones induced by the other beam (no rotation of ripples' orientation). Moreover, the alternate irradiation was performed at time intervals equal to or larger than 1 ms, so that when the laser pulses hit the surface, the latter was already at the equilibrium state.

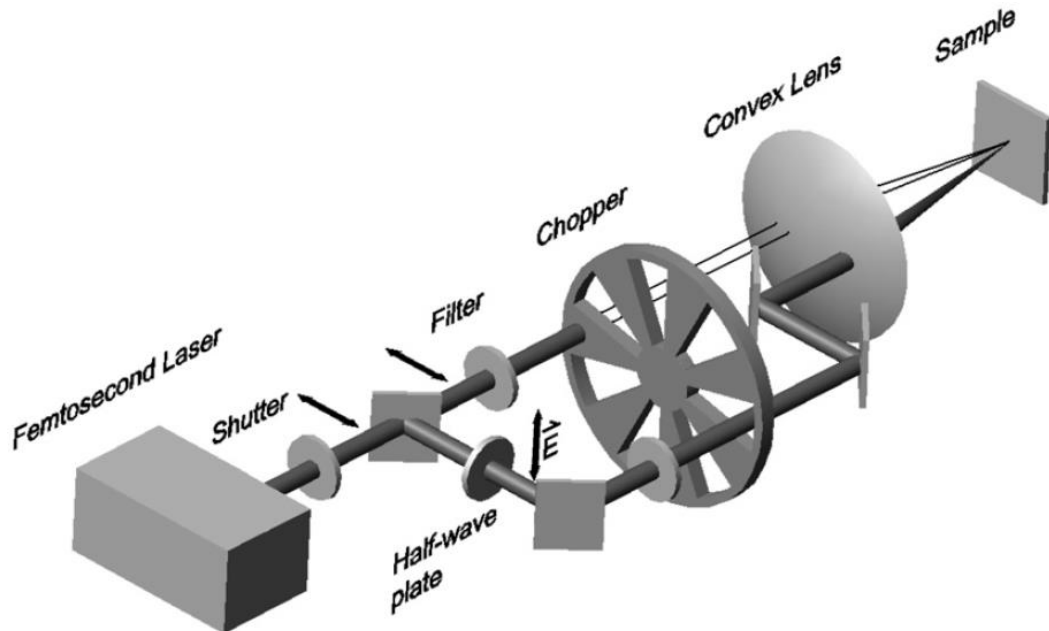


Fig. 34 Sketch of the experimental set-up for two-beam alternate ablation (TBAA). [96]

A further approach for 2-D sub-wavelength surface structuring is the use of optical vortex beams generated by an s-waveplate [97] or q-waveplate [98], whose control of the beam polarization induces subwavelength ripples preferentially oriented in a direction normal to the local laser polarization. Successive studies conducted by Skoulas et al. [53] have reported rhombic-like LIPSS that mimic the sharks' skin morphology on Ni surface (Fig. 35). These structures were originated by line scans with radial and azimuthal cylindrical vector (CV) beam.

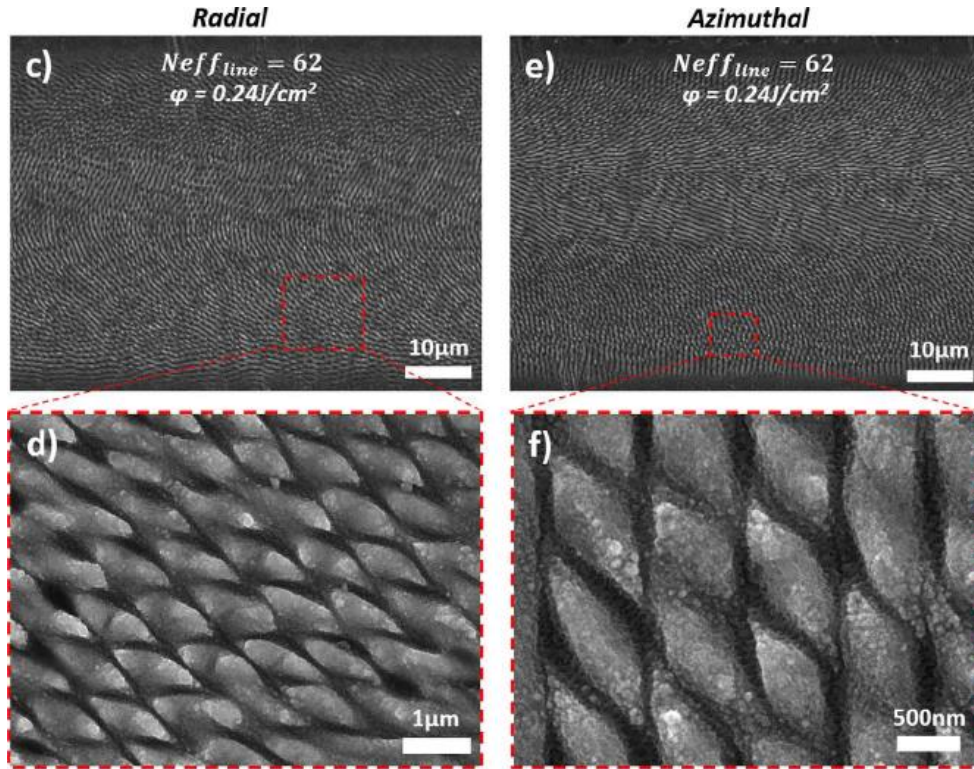


Fig. 35 SEM images of line scans produced by (c-d) radially and (e-f) azimuthally polarized beam at scan speed of 0.5 mm/s and laser fluence $F = 0.24 \text{ J/cm}^2$. The images (d, f) represent a zoomed view. [53]

Very recently novel two-dimensional periodic structures have been reported: array of triangles organized in hexagonal arrangements, as reported in Fig. 36a [99]. Surprisingly, these 2D triangular-like LIPSS were fabricated on stainless steel surfaces in single step using femtosecond laser beam with circular polarization. The triangles placed in hexagonal arrangement were indicated by peaks in the 2D-FFT aligned along 3 directions of periodicity at around 60° from each other (2D-FFT of Fig. 36a).

The 2D-LIPSS generation, with approximately 900 nm periodicity, was very sensitive to the process parameters, i.e. scanning speed, pulse fluence and focal plane offsets (Fig. 36b).

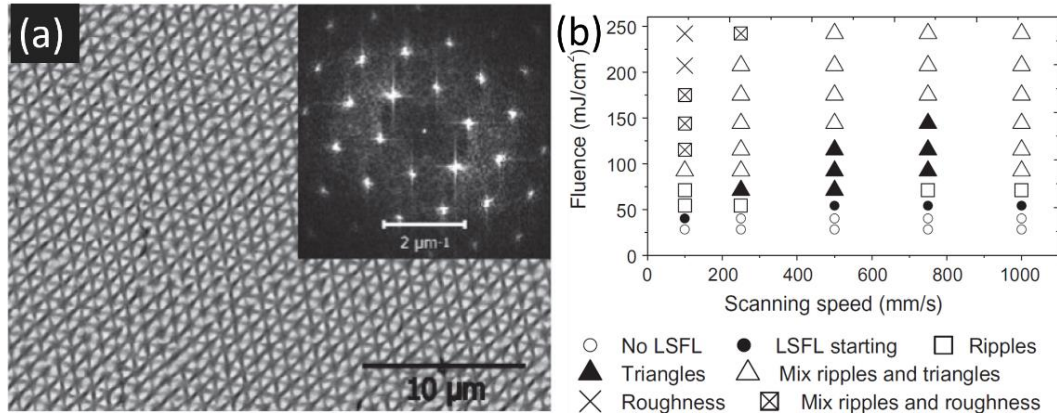


Fig. 36 SEM image of the triangular-like 2D-LIPSS obtained on stainless steel with $F = 92 \text{ mJ/cm}^2$, pulse per spot pps = 177 (overlap $O = 92\%$) and scanning speed $s = 500 \text{ mm/s}$. The inset represents the FFT of the SEM image. (b) Surface morphologies generated varying scanning speed and pulse fluence with 250 kHz and hatch distance of $2 \mu\text{m}$. [99]

Similar triangular structures were induced by Fraggelakis et al. [100] on stainless steel by employing a different technique. They used double pulse irradiation with variable inter-pulse delay Δt and orthogonal polarization states. A possible explanation for the formation of such structures is that in response to the first pulse interaction with the surface, the material stays in a transient state within few tens of picoseconds. If in this time lapse, a second pulse with different polarization compared to the first one, impinges the target, the surface material undergoes peculiar transformations giving rise to interesting surface morphologies, such as triangular-like LIPSS (Fig. 37). Accordingly, homogeneous triangle structures were obtained for $\Delta t < 10 \text{ ps}$. Nevertheless, similar structures reappear for $\Delta t = 3 \text{ ns}$ in Fig. 37, when the second pulse interacts with the supposedly resolidified surface.

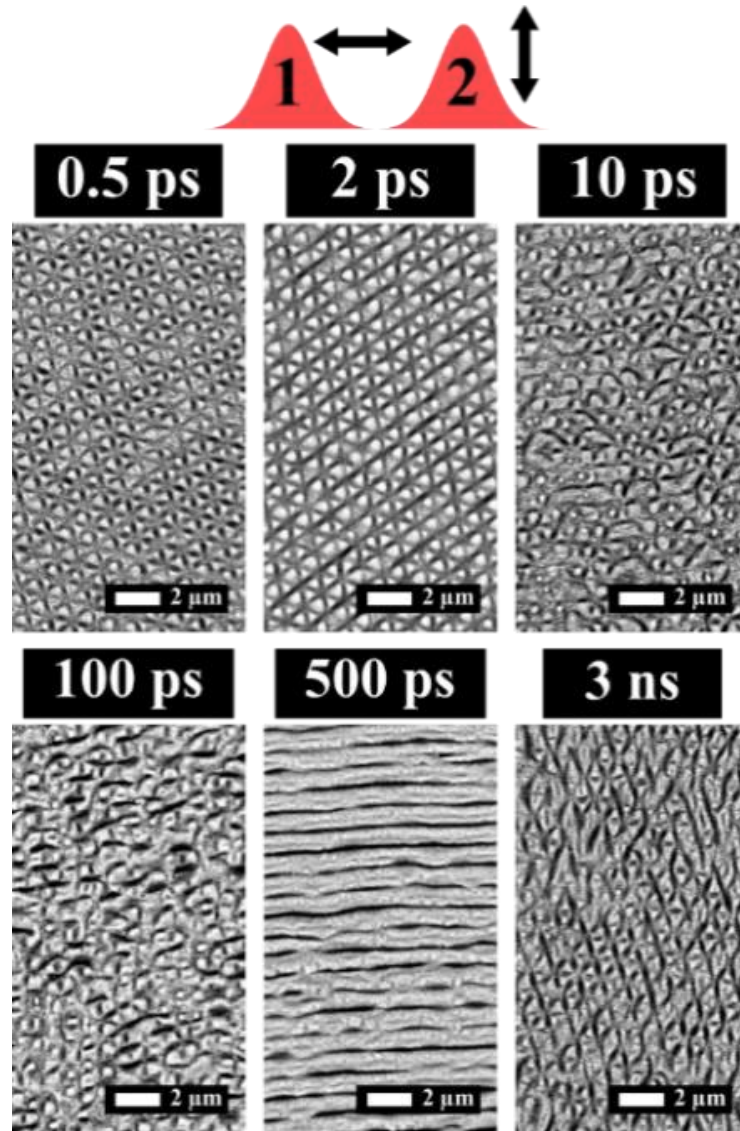


Fig. 37 SEM images of stainless steel surface irradiated by double pulse at different interpulse delay. The scanning parameters are: pps = 10, $H = 1 \mu\text{m}$. The fluence value was fixed to $F = 0.1 \text{ J/cm}^2$. [101]

Finally, Liu et al. [102] fabricated triangular structures on tungsten surface in single step using double cross-polarized beams ($\lambda = 800 \text{ nm}$; $\tau = 50 \text{ fs}$), similarly to Fraggelakis [100], at fixed time delay of 1.2 ps . Their investigation showed that the depth profile and spatial period of the structures can be modulated by changing the ambient air pressure from 1 atm to 10^{-3} Pa , as reported in Fig. 38. The structures depth was measured in correspondence of individual linear nanograting (d, Fig. 38d) and in the intersection point of the three nanograting (D, Fig. 38c), i.e. the centre of the hexagonal arrangement. It was found that when the air pressure was reduced,

the nano-triangles become less marked. Moreover, nanowires were noticed on the bottom of the nanogrooves.

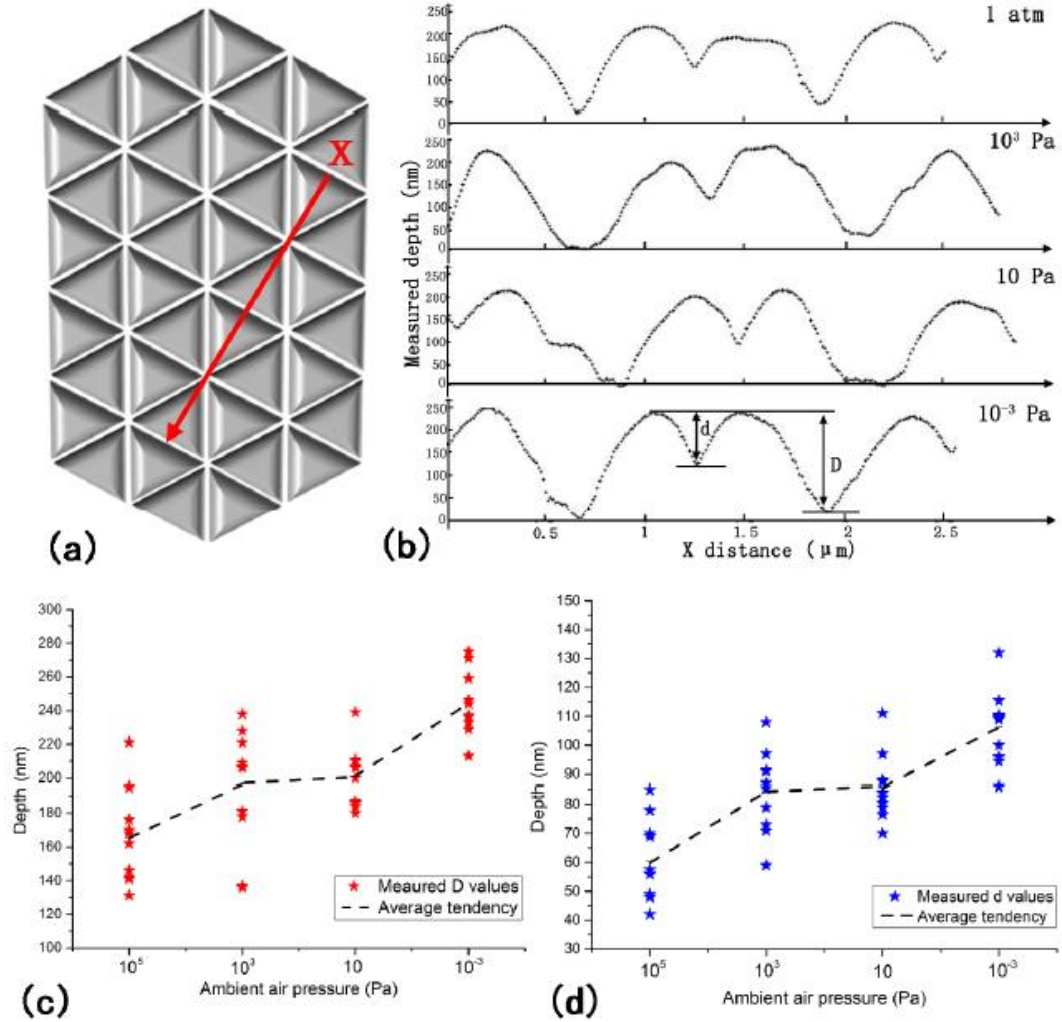


Fig. 38 (a) Schematic of the array of triangular structures on tungsten surface. The red line along X direction represents the direction along which was evaluated the ripples' profile. (b) Measured cross-sectional profiles for the triangular structures obtained under several different air pressures. d and D denote the depth of the individual groove and the intersection point of three grooves, respectively. (c) Depth D as a function of the ambient air pressure. (d) Depth d as a function of the ambient air pressure. [102]

Chapter 4

TTM with burst of pulses

In general, laser-matter interaction with ultrashort laser pulses produces a large excitation of electrons which redistribute momentum and energy among them via electron–electron collisions until a Fermi–Dirac distribution is reached within tens of femtoseconds [15]. After thermalization the electronic subsystem has a typical electronic temperature T_e of thousands of kelvin, while at the same time, the lattice system is mostly unaffected remaining at temperature T_l close to ambient temperature value. As a result of this electron–lattice nonequilibrium state, i.e. $T_e \neq T_l$, the energy stored in the electronic subsystem is transferred to the lattice by electron–phonon coupling on a typical timescale for metals of few picoseconds to reach the equilibrium, $T_e = T_l$. As already mentioned in chapter 1.2, this temperature evolution is modelled through the two-temperature model which takes into account also the energy dissipation inside the material due to heat thermal diffusion. Such TTM model was employed in case of burst of fs-pulses and making same approximations/assumptions related to numerous thermodynamic parameters, among them the electronic heat capacities, the electron–phonon coupling and the thermal conductivity for stainless steel.

4.1 Numerical model

Numerical simulations based on TTM model have been developed to calculate the temporal and spatial evolution of the lattice temperature when bursts with different number of sub-pulses are used. In particular, one of the aims is to evaluate the time and the laser energy needed for the lattice to reach the melting temperature.

Due to ultrashort laser pulses, the thermal non-equilibrium between electrons and lattice is described by the two energy conservation equations already mentioned (Eq. 1.12 and 1.13):

$$4.1 \quad C_e \frac{\partial T_e}{\partial t} = \frac{\partial}{\partial z} \left(k_e \frac{\partial T_e}{\partial z} \right) - G(T_e - T_l) + Q$$

$$4.2 \quad C_l \frac{\partial T_l}{\partial t} = \frac{\partial}{\partial z} \left(k_l \frac{\partial T_l}{\partial z} \right) + G(T_e - T_l)$$

which govern the electron temperature, $T_e = T_e(z, t)$, and the lattice temperature, $T_l = T_l(z, t)$. For simplicity without losing accuracy, the TTM equations have been expressed in one-dimension, along the laser beam

propagation direction (z-axis) because in the real situation the laser spot size on the sample surface is much larger than the thermally affected depth. In general, the thermodynamic parameters, such as heat capacities (C_e , C_l), thermal conductivity (k_e , k_l) and electron–phonon coupling factor (G), are function of the temperature of the electron and lattice sub-system. Nevertheless, they are subject of approximation. The lattice thermodynamic properties were assumed constant and set to $C_l = 4.1496 \times 10^6 \text{ J K}^{-1} \text{ m}^{-3}$ and $k_l = 18 \text{ W K}^{-1} \text{ m}^{-1}$ [103,104]. On the other hand, the electron thermodynamic properties were strongly dependent on the electron temperature, as shown in Fig. 39.

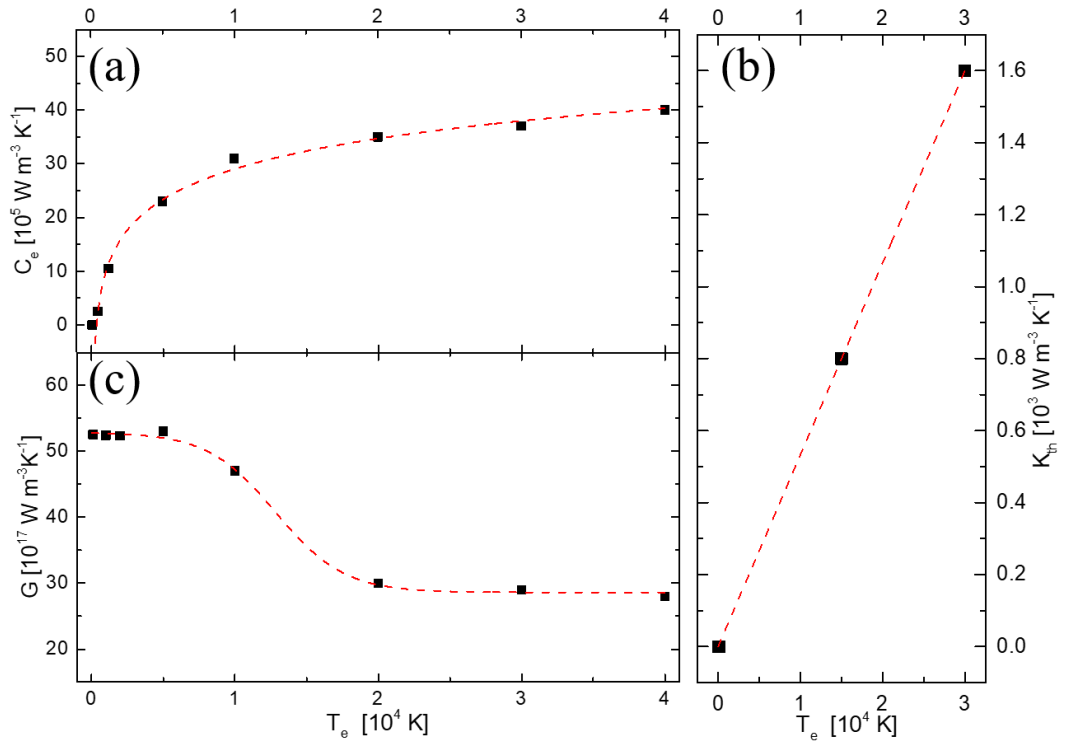


Fig. 39 (a) Electronic heat capacities as a function of the electronic temperature. (b) Strong dependency of the thermal conductivity by the electronic temperature. (c) T_e dependent effective electron–phonon coupling for stainless steel. Red dotted lines represent the fit of the black point evaluated by Bvillon in [105] for 316L stainless steel.

The behaviour of the thermodynamic coefficients as a function of T_e in Fig. 39 were obtained by Bvillon et al. [105]. The calculations were carried out in the framework of the density functional theory (DFT) on the time scale of electron–phonon relaxation upon ultrashort laser excitation for 316L stainless steel. In order to solve the TTM equations, for each thermodynamic

property the analytic functions of T_e were obtained by fitting the Bvillon' results (red dotted lines in Fig. 39).

$$4.3 \quad C_e(T_e) = [28.02 + 9.29 \ln(T_e \times 10^{-4} + 0.03)] \times 10^5$$

from Fig. 39a

$$4.4 \quad k_e(T_e) = [0.535 (T_e \times 10^{-4}) - 0.004] \times 10^3$$

from Fig. 39b

$$4.5 \quad G(T_e) = \left[28.68 + \frac{24.25}{1 + \exp\left(\frac{T_e \times 10^{-4} - 1.27}{0.23}\right)} \right] \times 10^{17}$$

from Fig. 39c

where C_e has the dimensions of a volumetric specific heat, $J K^{-1} m^{-3}$, k_e in $W K^{-1} m^{-1}$ and G in $W K^{-1} m^{-3}$ (T_e in K). Finally, the laser energy absorbed from electrons was connected to the laser irradiation I_{las} by:

$$4.6 \quad Q = \alpha(1 - R) I_{las}(t) \exp(-\alpha z)$$

where R is the reflectivity of the irradiated surface, and α^{-1} the optical penetration depth. In case of bursts, the laser beam time profile $I_{las}(t)$ was given by the sequence of the n gaussian sub-pulses delayed of Δt :

$$4.7 \quad I_{las}(t) = \sqrt{\frac{\beta}{\pi}} \frac{I_0}{n} \sum_{i=0}^{n-1} \exp \left[-\beta \frac{(t - (i \Delta t + t_0))^2}{\tau^2} \right]$$

where $\beta = 4 \ln 2$, $I_0 = F_0/\tau$, τ denotes the pulse duration, and t_0 is the time at which the laser source is switched on. F_0 is the peak laser fluence defined as a function of the pulse energy E and the laser spot radius w on the sample surface.

4.2 Numerical simulations

The TTM model described by Eqs. 4.1-4.2 was applied to calculate the electron and lattice temperatures as functions of time t and position z through the sample thickness. It was implemented in the open source computational software OpenFOAM®. Moreover, the model results valid for $T_l \leq T_m$ where T_m denotes the melting temperature of the stainless steel and it becomes oversimplified when T_l exceeds T_m since the energy sink term of fusion enthalpy is not taken into account in Eq. 4.2. No phase changes were taken into account.

The calculations were done assuming that the optical properties, i.e. absorption length and reflectivity, of the solid material are constant during irradiation. Hence, for the source term of Eq. 4.6, the constant parameters were set to $R = 0.9$ and $\alpha = 51 \times 10^4 \text{ cm}^{-1}$ [106,107]. Five cases were employed as laser beam time profile, four of these were bursts and the other

was the single pulse referred to as NPM. The latter corresponded to $n = 1$ in Eq. 4.7. The investigated bursts had two and four sub-pulses, respectively, with intra-burst delay of 1.5 ps and 3 ps:

$$4.8 \quad (n, \Delta t) = \{(2, 1.5 \text{ ps}); (2, 3 \text{ ps}); (4, 1.5 \text{ ps}); (4, 3 \text{ ps})\}$$

Moreover, for each configuration the pulse duration was set at $\tau = 650 \text{ fs}$, the laser spot $w = 21.5 \text{ }\mu\text{m}$, the burst energy $E = 5 \text{ }\mu\text{J}$ and $t_0 = 5 \text{ ps}$ in Eq. 4.7.

In Fig. 40, the laser power density on the top surface of the sample (i.e. $z = 0 \text{ nm}$) is plotted as a function of time for different combinations of n and Δt .

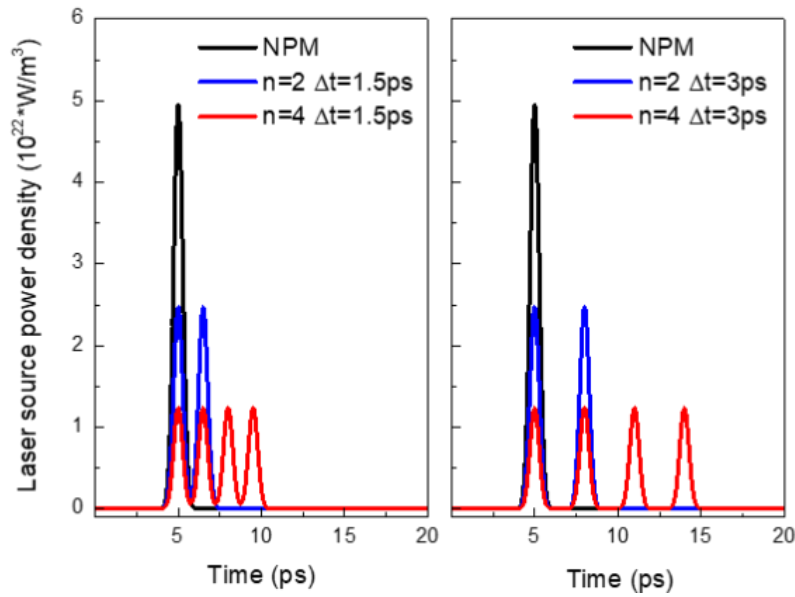


Fig. 40 Laser power density as a function of time calculated on the top surface of the sample (i.e. in $z = 0 \text{ nm}$) in case of constant burst energy. On the left: NPM and BM with time separation of 1.5 ps and 2 and 4 sub-pulses; on the right: NPM and BM with time separation of 3 ps and 2 and 4 sub-pulses.

As clearly shown in Fig. 40, the numerical simulations were carried out by keeping fixed the total laser intensity impinging on the sample for all configurations: the laser energy heat source in NPM was split in more sub-pulses in BM. It was assumed that heat transfer to the surroundings is negligible during the time interval of the few picoseconds between sub-pulses. Therefore, processes of natural convection and radiation for the sample cooling were neglected. The Neumann boundary conditions with zero gradient were set in $z = 0 \text{ nm}$:

$$4.9 \quad \partial_z T_e(0, t) = 0 \quad \text{and} \quad \partial_z T_l(0, t) = 0$$

It was verified for each of the test cases that a computational domain of thickness $L = 1000 \mu\text{m}$ (less than the sample thickness of 2 mm) was sufficient to allow setting the following boundary conditions in $x = L$:

$$4.10 \quad \partial_z T_e(L, t) = 0 \quad \text{and} \quad \partial_z T_l(L, t) = 0$$

The sample started with uniform temperature equal to 300 K . Therefore, the initial conditions were written as:

$$4.11 \quad T_e(z, 0) = T_l(z, 0) = 300 \text{ K} \quad \text{for} \quad 0 \leq z \leq L$$

The domain was meshed with uniform cells of 1 nm . It was verified that such cell size was sufficient to reach convergence in mesh. The time step was set to 0.0001 ps to satisfy a convergence criteria of 10^{-6} (residual in L^2 norm). The electron and lattice temperatures calculated as functions of time in $z = 0 \text{ nm}$ are plotted in Fig. 41 for NPM case and in Fig. 42 for the different burst configurations of sub-pulses n and intra-burst timer delay Δt . The correspondence laser source power density, Q , is also drawn in each plot.

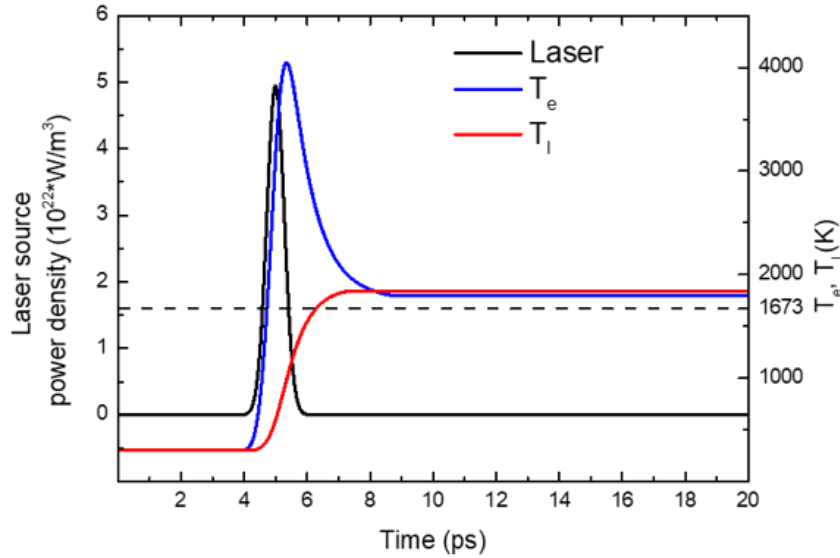


Fig. 41 Temporal evolution of the laser source power density and of the electron and lattice temperatures calculated on the top surface of the sample (i.e. in $z = 0 \text{ nm}$), in NPM. The black curve represents the laser power density. The dashed line corresponds to the melting temperature of stainless steel.

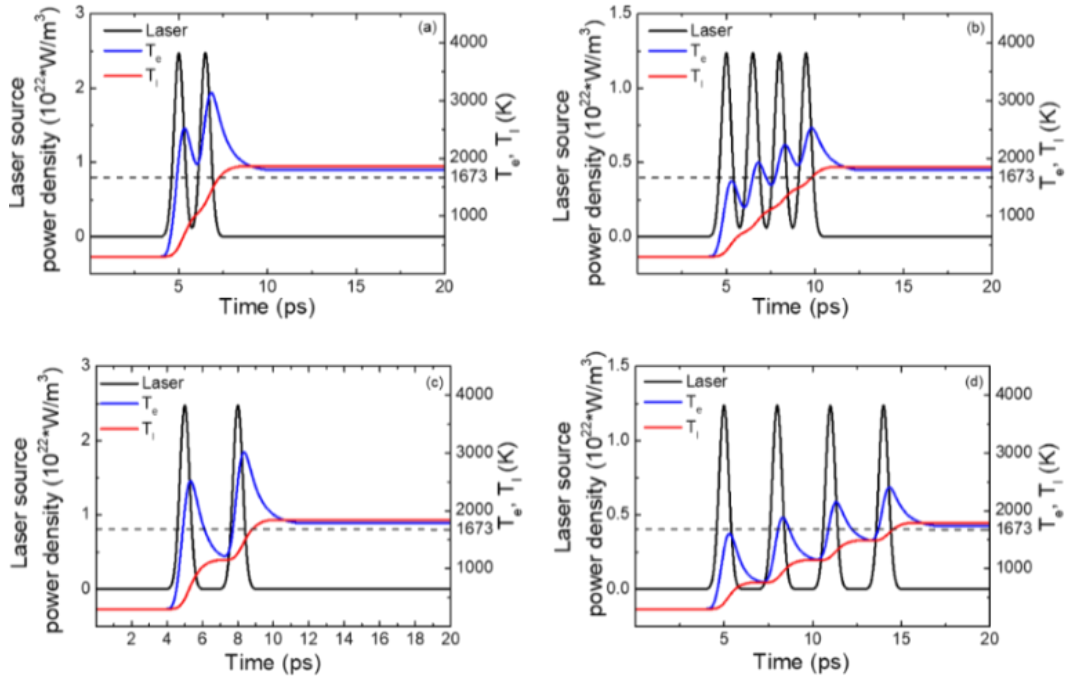


Fig. 42 Temporal evolution of the laser source power density and of the electron and lattice temperatures calculated on the top surface of the sample (i.e. in $z = 0$ nm), in BM. (a) $n = 2$ and $\Delta t = 1.5$ ps; (b) $n = 4$ and $\Delta t = 1.5$ ps; (c) $n = 2$ and $\Delta t = 3$ ps; (d) $n = 4$ and $\Delta t = 3$ ps. The dashed line in each plot corresponds to the melting temperature of stainless steel.

In Fig. 41 it can be observed that in NPM the lattice temperature reaches the melting temperature T_m after the pulse is over (i.e. after the trailing tail of the laser pulse). On the other hand, in case of BM, Fig. 42 shows that the melting temperature is achieved before the end of the burst (i.e. before the last sub-pulses in the burst is over). Therefore, it can be concluded that less energy is needed in BM for reaching T_m . This indicates that using bursts of sub-pulses with ps delays produces a more efficient transfer of the laser energy to the material. To better represent this result, in Fig. 43 the normalized laser energy needed to reach melting of the lattice E_m is plotted as a function of the burst features.

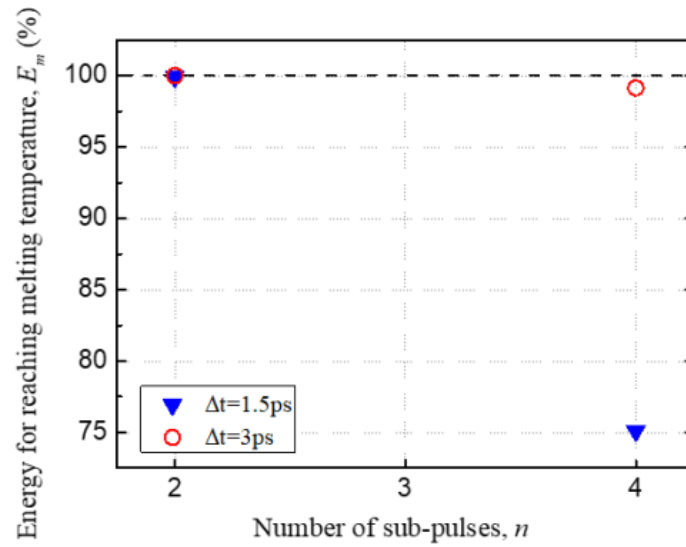


Fig. 43 Normalized energy for reaching melting versus number of sub-pulses, for $\Delta t = 1.5 \text{ ps}$ and $\Delta t = 3 \text{ ps}$. For comparison, the dashed line represents the NPM case, where all the laser energy is needed to reach melting.

Here, it can be noticed that in NPM the entire amount of the laser energy absorbed by the sample is needed for melting to take place. Similar result is obtained in BM with $n = 2$ and $\Delta t = 3 \text{ ps}$. Increasing the pulse splitting from 2 to 4, less energy E_m is required for reaching melting. Results of this analysis are summarized in Table 4-1.

Table 4-1 Normalized energy needed for reaching the melting temperature in NPM (i.e. $n=1$) and BM.

$n \backslash \Delta t$	1.5 ps	3 ps
1	100%	
2	99.9%	100%
4	75.0%	99.1%

Chapter 5

Experimental setup and methods

In this chapter, the experimental apparatus for studying the ablation and texturing processes with bursts and the instruments used for post-process analysis for characterizing the features of produced samples, are presented. Experiments on steel targets were run with the experimental setup sketched as follows (Fig. 44):

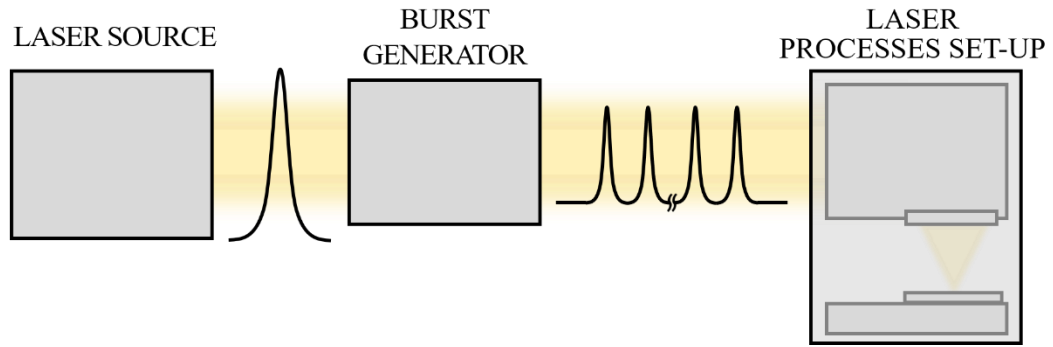


Fig. 44 Schematic of the experimental setup.

The *laser source* delivered the ultrafast laser pulses which were split in sub-pulses by the *burst generator*. Finally, the laser beam was employed for the target processing (*laser processes set-up*). In the following, each block will be described together with the used operation conditions.

5.1 Laser source

Two laser sources were used for carrying out the experiments of this thesis. Both were able to generate ultrashort laser pulses at the wavelength of 1030 nm. In the following, the main features of each lasers are presented.

5.1.1 Active Fiber System Sci-Series

The ultrashort laser source Sci-Series from Active Fiber Systems (AFS) GmbH consists of a fiber chirped pulse amplification (CPA, [108]) system comprising an ultrafast fiber laser oscillator, a stretcher-compressor unit and two amplification stages based on diode-pumped Yb-doped core photonic crystal fibers. The schematic of the laser source is sketched in Fig. 45.

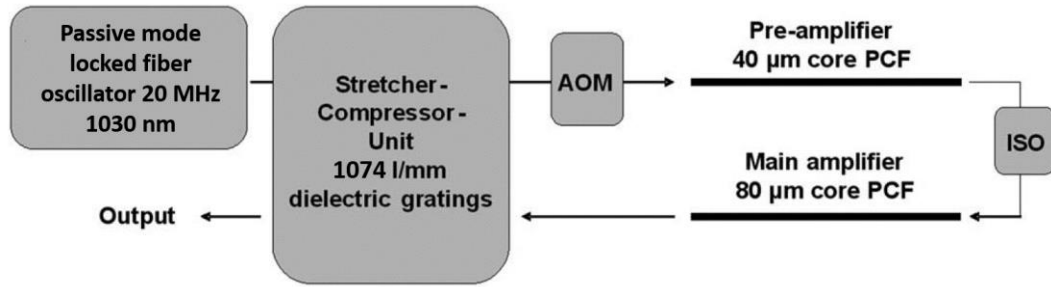


Fig. 45 Schematic of the Active Fiber System GmbH. ISO: optical isolator; AOM: acousto-optical modulator; PCF, photonic crystal fiber. [109]

First, a passively mode-locked diode-pumped Yb-doped fiber oscillator [110] delivers pulses at a repetition rate of 20 MHz at 1030 nm center wavelength. The time duration of outgoing pulses is around 500 fs. Then, a stretcher unit temporally stretches the ultra-short pulses from the oscillator up to 500 ps. It consists of two 1074 lines/mm dielectric diffraction gratings, one of which is mounted on a motorized translation stage. The following quartz-based acousto-optic modulator (AOM) allows reducing the pulse repetition rate in a range 50 kHz - 10 MHz by pulse picking. Afterwards two single-pass amplification stages which comprise a 1.2 m long Yb-doped photonic crystal fibers, spaced out by an optical isolator, providing a total gain factor of 25000. Both fibers are pumped by laser diodes at the wavelength of 976 nm. In particular, the preamplifier fiber is an air-clad photonic crystal with internal cladding diameter of 170 μm and 40 μm in core diameter. It is capable of delivering a single pass gain as high as 35 dB and average powers up to 6 W. The main amplification fiber has 80 μm core diameter and 200 μm internal cladding diameter allowing a pump stage with a coupling efficiency up to 80%. A water cooling system is used to prevent thermo-optical and thermo-mechanical damages in the fibers, when high pump power is provided. Finally, the dielectric compression grating operates the time compression of the amplified pulses in a continuously tunable range from 650 fs to 20 ps.

The laser beam comes out with linear polarization, Gaussian profile with $M^2 < 1.5$. The maximum pulse energy is limited to 100 μJ up to 500 kHz. At higher repetition rates, the maximum available average power is 50 W. Second and third harmonic generators are also provided, with conversion efficiency respectively equal to 50% and 15%.

5.1.2 Pharos laser

The Pharos-SP from Light Conversion is a single-unit integrated femtosecond laser system. It is based on CPA technique, which uses

Yb:KGW (ytterbium doped potassium gadolinium tungstate) as active medium, pumped by Light Conversion high-brightness diode modules delivering optical power up to 60 W. The laser system, depicted in Fig. 46, consists of a Kerr-lens mode-locked Oscillator (OSC), Regenerative Amplifier (RA), Stretcher-Compressor (S-C), Chiller, and Power Supply Unit (PS), supplying electrical current for laser diodes and other parts mentioned above. The system includes a motorized delay line for automated Compressor length adjustment and a Pulse-Picker (PP) for selecting a precise number of pulses to be driven on the target, which consists of a low loss BBO Pockels cells. Finally, the Timing Electronics Module (TEM) automatically controls the whole system.

The PHAROS laser delivers a linearly polarized beam at a wavelength equal to 1030 nm, with tunable pulse duration between 190 fs and 10 ps, variable repetition rate between 1 kHz and 200 kHz, maximum pulse energy higher than 1.5 mJ and maximum average power of 6 W.

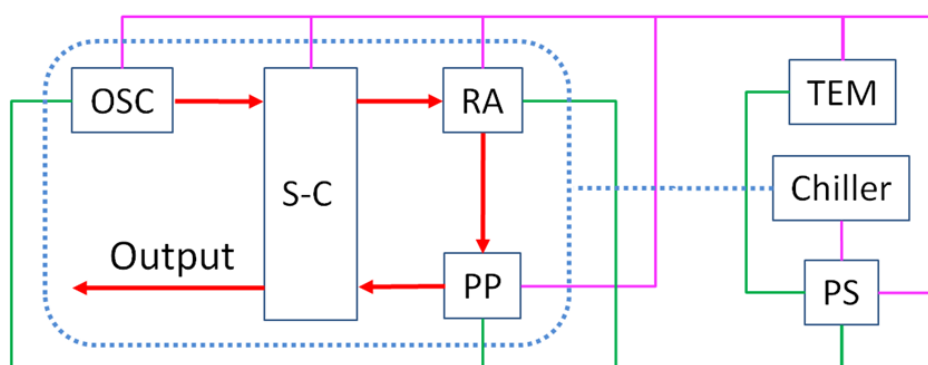


Fig. 46 Pharos system design. Red line: laser path; Dotted blue line: water cooling system; Green line: electric circuit; Pink line: Control electronic. From PHAROS User's Manual.

5.1.3 Selection of laser pulses

In some experiments were required a limited number of pulses from ones delivered by the laser sources at fixed repetition rate. In this research work, it was necessary to select a precise number of laser pulses to evaluate the ablation threshold fluence and the subsequent incubation factor, as will be described in the next chapter. In detail, an external acousto-optic modulator (AOM) was employed to pick any desired number of pulses from the pulse train outgoing from the AFS Sci-Series laser system at a fixed repetition rate (i.e. the laser repetition rate). It was controlled by AOM Quantum Composer unit.

5.2 Burst generator

The burst generator consisted of five birefringent crystals (Fig. 47) which can originate bursts up to 32 sub-pulses. The ultrafast laser pulses coming from the laser source were linearly polarized and each of them gives rise to a single burst of specific features, such as number of sub-pulses n and intra-burst delay Δt , according to the arrangement and orientation of each crystal of the burst generator. This means that the bursts left the generator with repetition rate (burst repetition rate, f_{burst}) equals to that one of incoming laser pulses (laser repetition rate, f_{laser}).

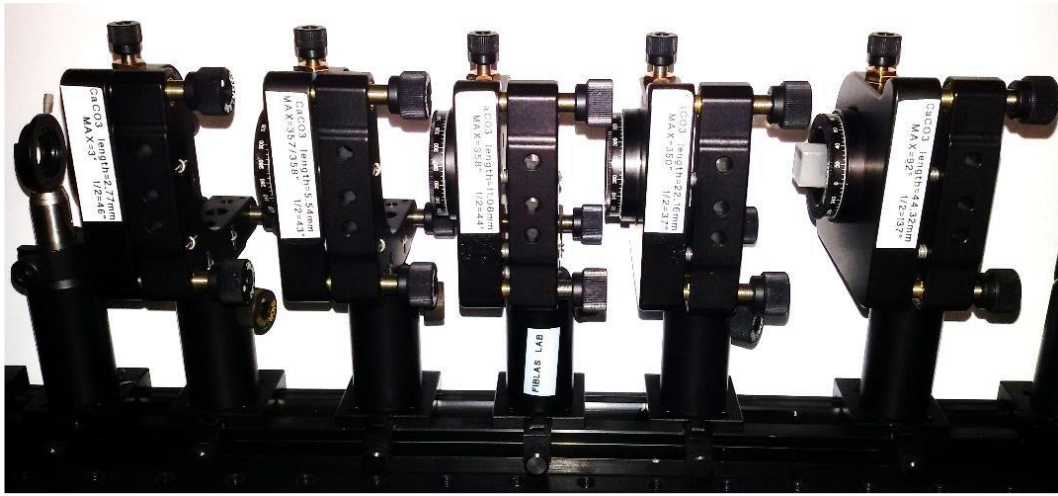


Fig. 47 Picture of the five CaCO_3 crystals.















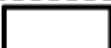



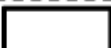



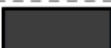




































The crystals were made of calcite (CaCO_3) with optical axes parallel to the incidence surface of the laser pulses. The laser beam was directed perpendicularly to the crystals. A laser pulse was split in two sub-pulses when its linear polarization results along the direction other than parallel or perpendicular to the optical axis of the crystal. At the exit from the crystal the two sub-pulses were time delayed. As described in Eq. 2.1, the time delay was proportional to the difference between the ordinary and extraordinary refractive index values, for calcite $n_o = 1.658$ and $n_e = 1.486$, but also to the crystal thickness l .


The burst generator was designed to work with pulses as short as 750 fs ($FWHM_{max}$), generating burst with constant intra-burst delay Δt . This allowed to use the burst generator for both laser sources at their shortest pulse durations. To distinguish the two sub-pulses in time, it was necessary that of the delay Δt introduced by each crystal was at least double the pulse duration, ($\Delta t \geq \Delta t_{min} = 2 FWHM_{max}$), hence of 1.5 ps. So that, the smallest calcite crystal was fixed at $l = 2.77 \text{ mm}$ (theoretical time delay of $\Delta t = 1.5 \text{ ps}$).

The thickness of the other crystals were chosen to be multiple of 2.77 mm in order to have bursts of sub-pulses with constant intra-burst delay ($\Delta t = 1.5\text{ ps}$). In other words, crystals of five different thicknesses were designed to produce inter-sub-pulse delays of 1.5, 3, 6, 12, 24 ps when they split the incoming pulse. Moreover, each crystal was mounted on a rotational stage allowing to change the orientation of its optical axis with respect to the polarization of the incident pulse/s. This represented the main advantage of such set-up since it allows to change the burst configurations, by simply ‘rotating out’ or ‘rotating in’ the crystals. ‘Rotating out’ means to make the crystal off, i.e. to orient its optical axis collinearly, or orthogonally to the incident polarization [35,36], so that the incident pulse does not undergo splitting. ‘Rotating in’ enables the crystal to split the pulse and if the optical axis is oriented at 45° to the incident pulse polarization, an equal energy splitting (50:50) between the two sub-pulses occurs.

For example, when all crystals of the burst generator had the optical axes aligned and parallel to the polarization of the incident pulse, the latter crossed the generator without undergoing any splitting and no burst was generated (Fig. 48a). On the other hand, when the optical axes were oriented in such a way that each crystal split the incident pulses/sub-pulses, the final burst consisted of 32 sub-pulses with energy $E_{sub-pulse} = E/32$, where E is the pristine laser pulse energy (Fig. 48f). Several other crystal configurations are possible to obtain bursts with equally time-spaced (Δt) pulses. The main burst generator configurations are represented in Fig. 48. The burst features depended on the orientation of the crystals’ optical axes and their order along the array, from the left crystal (I) to the right one (V) in Fig. 48.

The outgoing bursts from the crystals array was indicated as XP, cross polarized burst, because the sub-pulses were polarized both parallelly and orthogonally with respect to the optical axes of the crystals.

Crystal order						n	Δt (ps)
I	II	III	IV	V			
Pulse							
Crystal name	C_1	C_2	C_3	C_4	C_5		
(a)						1	/
(b)						2	1.5
(c)						4	1.5
(d)						8	1.5
(e)						16	1.5
(f)						32	1.5
(g)						2	3
(h)						4	3
(i)						8	3
(l)						16	3
(m)						2	6
(n)						2	12
(o)						2	24
(p)						2	46.5

 Optical axes collinear to the incident pulse polarization


 Optical axes at 45° to the incident pulse polarization

Fig. 48 (dotted rectangle) Array of five crystals with increased thickness from C_1 to C_5 . The laser pulse crosses the crystals array from left to right in the sketch, from I to V crystal. (a-p) Main crystals configurations to generate burst with n number of sub-pulses and Δt intra-burst time delay. (a) no split (empty crystals); Generation of burst with (b-f) fixed time delay at 1.5 ps and number of sub-pulses $n = 2^x$, with x number of splitting (filled crystals); (g-l) fixed time delay of 3 ps and number of sub-pulses $n = 2^x$; (b,g,m-o) $n = 2$ and time delay related to the V crystal; (p) $n = 2$ and time delay sum of all crystal time delays.

When a quarter-wave plate was used after the optical chain of the calcite crystals, the XP burst was converted into circularly polarized (CP) burst. In some experiments the CP burst polarization has been preferred in order to prevent anisotropic absorption of light in during ablation of deep features [111]. In addition, a polarizer was used to obtain linearly polarized burst that will be referred as LP burst in the following. The optical axes of the polarizer was oriented along the bisector between the two linear polarizations of the XP burst, so that all sub-pulses resulted linearly polarized and parallel among them. Nevertheless, using the polarizer with XP burst, only half of the laser power was transmitted.

The crystals order was fundamental, in fact reversing their order different burst configurations were obtained, as shown in Fig. 48b and Fig. 48p.

It is worth noticing that with decreasing crystal thicknesses (such as Fig. 48f), the resulting sub-pulses inside the burst are alternately polarized. Instead, with increasing crystal thicknesses (inverting the order of the crystals in Fig. 48f), the first $n/2$ sub-pulses have parallel polarization to optical axis of the last crystal while the following $n/2$ sub-pulses have orthogonal polarization. Finally, the total energy per burst and/or the sub-pulses energy was finely adjusted by means of a half-wave plate and a polarizer placed upstream of the calcite crystals. A further half-wave plate followed by a polarizer were positioned after the crystals array to rotate the sub-pulse polarization at desired angles. This was required during the LIPSS experiments because the polarization direction influence the final ripples orientation [72].

5.2.1 Characterization of the burst generator

In this section, the characterization of each single crystals and of the whole burst generator is described. This was performed by an APE (Angewandte Physik&Elektronik GmbH) PulseCheck 150 autocorrelator (AC), which was able to measure pulse duration from 50 fs to 35 ps, with a resolution of 1 fs. The autocorrelator was used to measure the time duration of the laser pulses after the burst generator and check the time delay between consecutive sub-pulses generated by the birefringent crystals. Inside the autocorrelator the incident beam is split into two lines with tunable time delay τ , which are then re-combined into a nonlinear crystal. The latter generates a second harmonic signal only when the phase matching condition is satisfied [112]. The intensity of the second harmonic signal $I_{2\omega}(t, \tau)$ is proportional to the intensity of the two impinging beams on the nonlinear crystal:

$$5.1 \quad I_{2\omega}(t, \tau) \propto I_{\omega}(t)I_{\omega}(t + \tau)$$

where the beam with intensity $I_{\omega}(t + \tau)$ is delayed by τ with respect to the other one, $I_{\omega}(t)$. From a mathematical point of view, the nonlinear crystal

returns the convolution of the two incoming intensities as a function of the delay τ , according to the equation:

$$5.2 \quad G^2(\tau) = \frac{\int_{-\infty}^{+\infty} I_{\omega}(t)I_{\omega}(t+\tau)dt}{\int_{-\infty}^{+\infty} I_{\omega}^2(t)dt}$$

where G^2 is the second order autocorrelator function [113]. From the plot of the autocorrelation intensity as a function of τ the temporal shape of the incident beam can be evaluated. In Fig. 49 the autocorrelator signals for the laser beams of the two different laser sources after crossing the burst generator in case of no split configuration (Fig. 49a), are shown. A single peak is shown for each signal. Assuming for both lasers, AFS and Pharos, a Gaussian temporal profile of the pulses, their time duration is evaluated by [114]:

$$5.3 \quad FWHM_{pulse} = \frac{FWHM_{AC}}{\sqrt{2}}$$

where $FWHM_{pulse}$ and $FWHM_{AC}$ are the full width at half maximum of the actual laser pulse and of the autocorrelation peak, respectively. From Fig. 49 it follows that the experiments in NPM were conducted with pulses of duration ~ 752 fs and ~ 239 fs using AFS and Pharos laser, respectively.

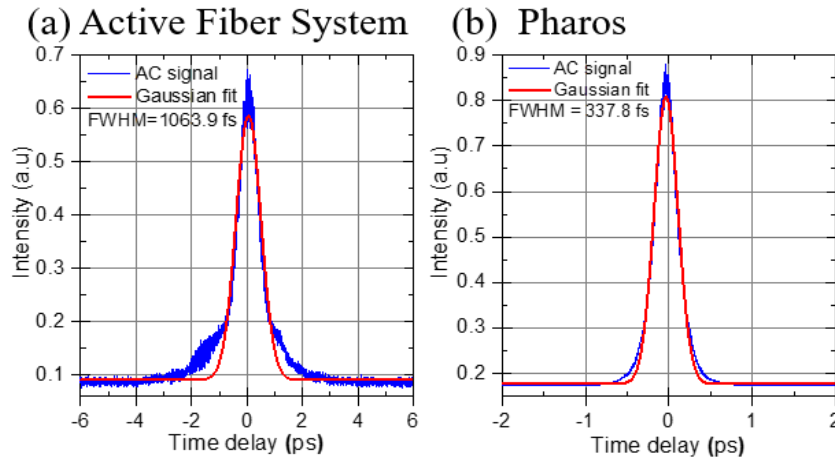


Fig. 49 Autocorrelation function for pristine pulses by (a) AFS and (b) Pharos laser. These pulses crossed the burst generator undisturbed (no split, configuration of Fig. 48a). The AC peaks are fitted with gaussian function because the incident pulses are supposed of gaussian shape [114].

In Fig. 50, the autocorrelator was used to check the time delay between the two sub-pulses generated by each single birefringent crystal. Here, more peaks are generated from the autocorrelation function and their temporal distance corresponds to the time delay between sub-pulses in the burst. In detail, the number of peaks in the AC signal is equal to $2n - 1$, where n is the number of sub-pulses in the burst. Hence, for two sub-pulses, three peaks were observed for each plot represented in Fig. 50.

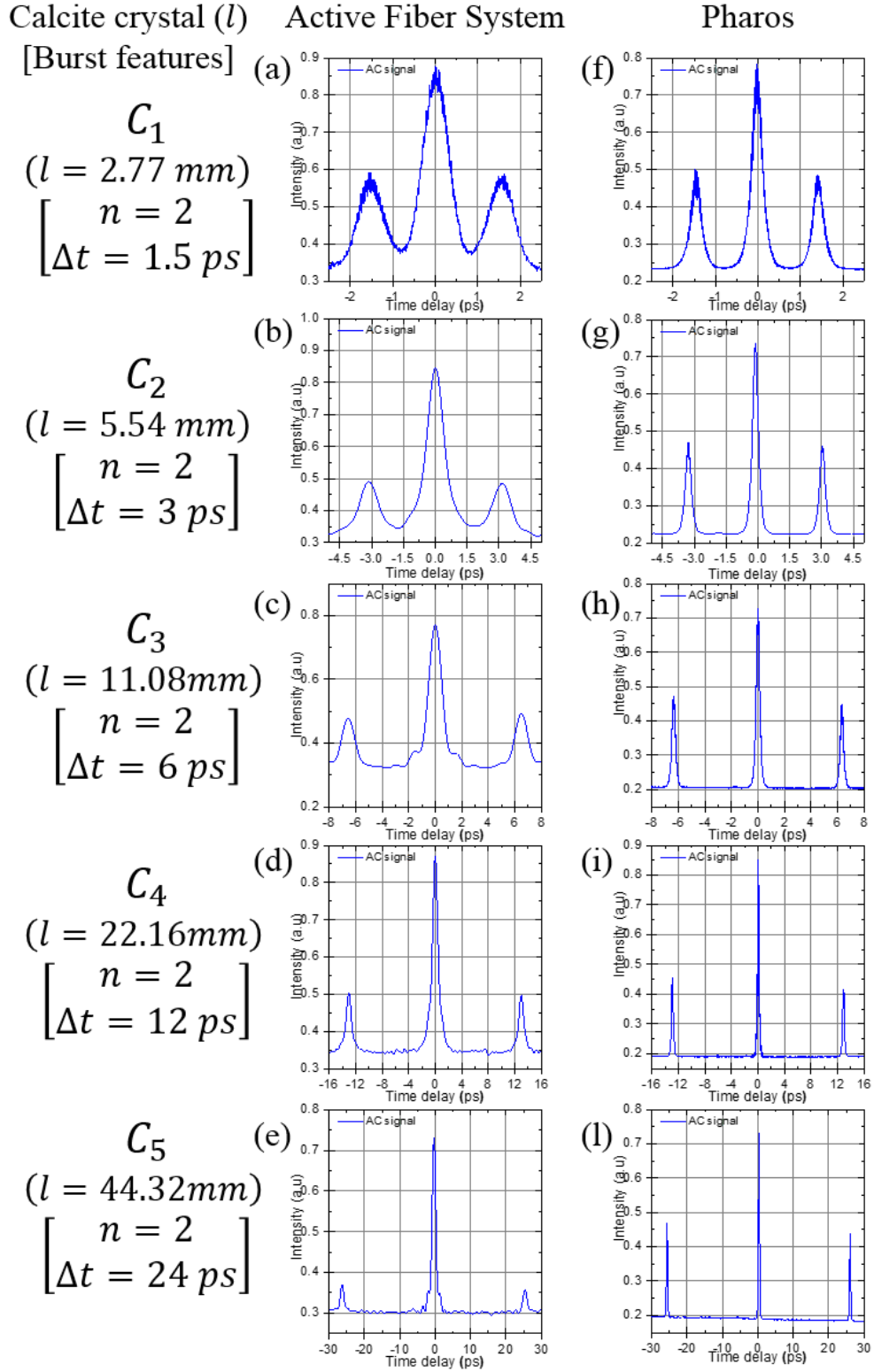


Fig. 50 Autocorrelation function of two sub-pulses burst induced by single crystal for laser beams by (a-e) AFS and (f-l) Pharos. Each row corresponds to burst generated by the single crystal whose time delay is indicated in the square brackets.

The time delay generated by each crystal is reported in Table 5-1. The last row of the table reports the time delay between two sub-pulses produced by the crystal configuration of Fig. 48p. With the latter arrangement a total delay between the two sub-pulse corresponding to the sum of the time delay introduced by each crystal is produced.

Table 5-1 Experimental values of time delay in correspondence of the theoretical ones.

Crystals	Δt_{th} (ps)	Δt_{AFS} (ps)	Δt_{Pharos} (ps)
C_1	1.5	1.56 ± 0.02	1.71 ± 0.01
C_2	3	3.12 ± 0.06	3.19 ± 0.13
C_3	6	6.34 ± 0.03	6.57 ± 0.11
C_4	12	12.85 ± 0.04	13.02 ± 0.07
C_5	24	25.85 ± 0.14	25.89 ± 0.17
$C_1 C_2 C_3 C_4 C_5$	46.5		50.36 ± 0.25

From Table 5-1 a small discrepancy (mostly below 1 ps) between the expected time delay and the measured one can be noticed. For simplicity, in the rest of this thesis the expected intra-burst time delays will be mentioned instead of the measured ones. The autocorrelation signals of the pulses produced with all possible burst configurations were analysed in order to make sure that the original pulse temporal profile was preserved and that the crystals did not introduce any distortion of the pulse shape. All the observed autocorrelation signals did not show any distortion. As an example, in Fig. 51, the autocorrelation function for the case of 8 sub-pulses with 1.5 ps intra-burst delay is reported, where 15 clearly distinguishable peaks were found. A total laser beam average power attenuation of about 12% was measured after the five crystals.

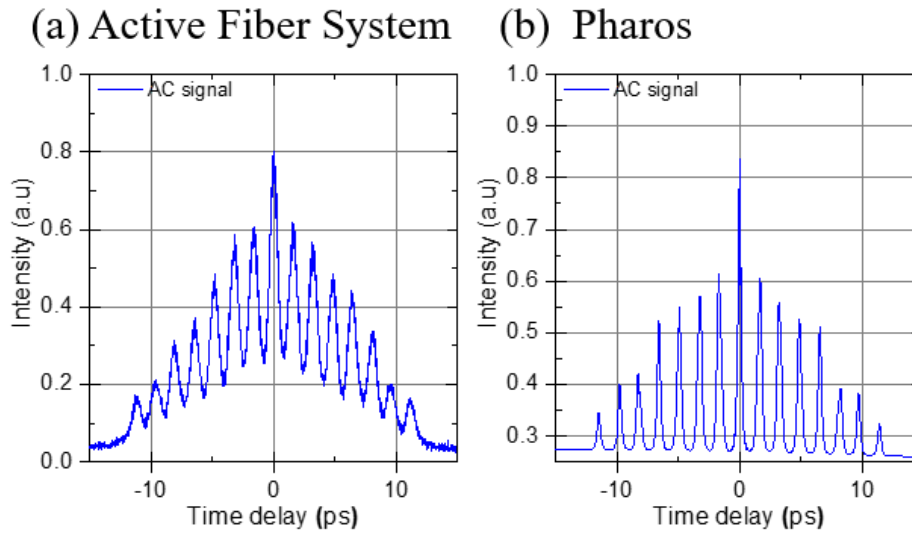


Fig. 51 Autocorrelation function of eight sub-pulses bursts in case of (a) AFS beam and (b) Pharos laser beam. The crystals configuration is that of Fig. 48d which should correspond to a time delay between sub-pulses of 1.5ps. 15 peaks are clearly visible for each plot.

5.3 Materials and laser processes set-up

The laser beam outgoing from the burst generator was focused on the target surface, which consisted of plates of austenitic stainless steel of 0.5 mm thickness of type AISI 301 and 304. The samples at low carbon content, 0.15% and 0.08% for AISI 301 and 304 respectively [115], were used with no chemical and/or mechanical pre-treatments of the surfaces before laser exposure. The chemical composition of samples is summarized in Table 5-2 while their physical and thermal properties are reported in Table 5-3.

Table 5-2 Chemical composition of austenitic stainless steels. [115]

AISI	C %	Cr %	Ni %	Mn %	Si %	P %	S %
301	0.15	16.0-18.0	6.0-8.0	2.0	1.0	0.045	0.03
304	0.08	18.0-20.0	8.0-10.5	2.0	1.0	0.045	0.03

Table 5-3 Physical and thermal properties of stainless steels. [115]

AISI	Melting point K	Density g cm ⁻³	Thermal conductivity W K ⁻¹ m ⁻¹
301	1400-1420	7.9	16.3
304	1400-1455	7.93	18.0 [103]

These steels are particularly used in chemical industry equipment, food processing, and automotive industry thanks to their good formability and weldability.

Three types of experiments were conducted to investigate the influence of the bursts features on ablation threshold fluence, ablation removal rate and laser-induced surface structures. In the following the setups used for each experiment are described in detail. All experiments have been performed at room temperature in ambient air without any gas shielding.

5.3.1 Laser ablation threshold

In order to evaluate the ablation threshold fluence, the method proposed by Liu [23] was used, which is based on the ablation of craters with different laser fluence and on the experimental measurement of their size. Such method, proposed for NPM processing, was applied also for BM processing, varying the burst features, i.e. number of sub-pulses $n = 2, 4, 8, 16, 32$ and intra-burst time delay $\Delta t = 1.5, 3$ ps.

In detail, the craters were produced by focusing the laser beam using a 100 mm focal length lens at normal incidence to the stainless steel AISI 304 target surface. The samples were translated through a motorized XY linear stage.

In these experiments, the Sci-Series laser (Chap. 5.1.1) was used with pulse duration of 750 fs, at a fixed repetition rate of 100 kHz. Moreover, the beam outgoing from the burst generator was converted to circular polarization (CP) in order to prevent anisotropic absorption of light in the inner walls of the craters [111].

Five craters were generated for each set of laser and burst parameters for averaging the diameter measurements. The energy of the burst was varied in the range $5 - 25 \mu J$ while number of bursts from 50 to 1600. Analogous experiments were conducted in NPM for comparison.

5.3.2 Laser surface texturing

Surface texturing experiments were performed to study the influence of the burst features on the morphology of the laser-induced surface structures. In these experiments the influence of the number of sub-pulses, the time delay, and the burst polarization were investigated. As regards the burst polarization, three groups of experiments were carried out, i.e. burst with linear, circular and crossed polarization. The number of sub-pulses was varied from 2 to 32 sub-pulses while the intra-burst time delay between 1.5 ps and 24 ps.

These experiments were conducted with Pharos laser (Chap. 5.1.2) with pulse duration of 238 fs, at a fixed repetition rate of 200 kHz.

The surface areas of stainless steel AISI 301 plates were scanned by means of a Galvo Scanner system (SCANLAB's intelliSCAN 14) equipped with a F-theta telecentric lens of 56 mm in focal length. The laser beam with a spot diameter on the target surface of $24 \mu\text{m}$ ($1/e^2$ peak intensity) was moved over the sample surface following regular patterns of successive parallel lines separated each other by a space distance called hatch (H). The pulse overlap along each scanning line (referred as horizontal overlap in Fig. 52 P^H) can be evaluated by [116,117]:

$$5.4 \quad P^H = 100 \cdot \left[1 - \frac{v}{f d} \right]$$

where v is the laser scanning speed, d is the laser beam spot diameter and f is the laser repetition rate. The hatch distance determines the transverse overlap (defined as vertical overlap in Fig. 52, P^V) through [116,117]:

$$5.5 \quad P^V = 100 \cdot \left[1 - \frac{H}{d} \right]$$

The average number of pulses irradiated on a dimensionless spot of the surface along a line scan is defined as “pulses per spot”, pps , calculated as [118]:

$$5.6 \quad pps = \frac{d f}{v}$$

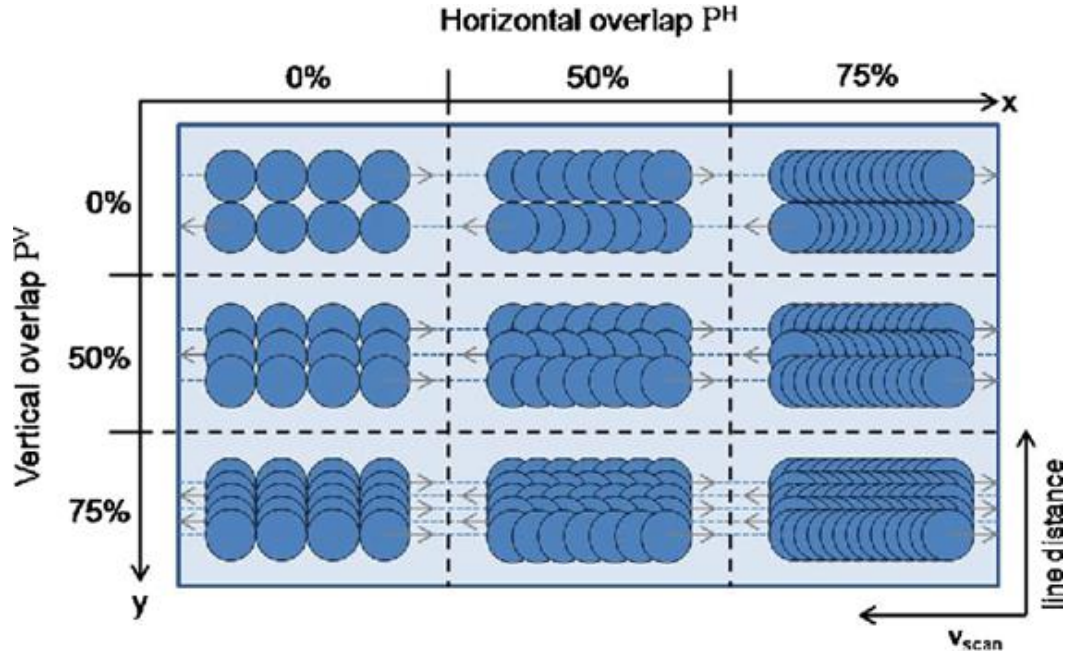


Fig. 52 Scheme of the two-dimensional pulse overlap along the scanning line and among the lines. The “horizontal overlap” P^H , which depends on repetition rate, scanning speed, and focal spot size. The second kind of

overlap is the “vertical overlap” P^V , given by the spacing between two lines and the focal spot size. [119]

The laser texturing took place in a single step and the experiments were carried out with laser fluence, scan speed and hatch distance in the ranges $0.1 - 1.0 \text{ J/cm}^2$, $0.02 - 1.0 \text{ m/s}$, and $1 - 20 \text{ }\mu\text{m}$, respectively.

5.3.3 Laser ablation removal rate

The laser milling experiments were carried out to evaluate the ablation removal rate when circularly polarized bursts are used instead of single pulses in NPM and to study the influence of the number of sub-pulses and the time delay on the removal rate.

The experiments consisted in laser milling of squared pockets with surface area of $0.5 \times 0.5 \text{ mm}^2$ on stainless steel AISI 301 targets. 238-fs pulses at a repetition rate of 200 kHz delivered by Pharos laser were used.

The milling process was conducted with the same set-up of the surface texturing, a galvoscaner equipped with a 56 mm focal length F-theta lens and using analogue scanning strategy described in Fig. 52. The differences between laser milling and surface texturing concerned the laser fluence range and the number of loops of the scanning process, that in case of laser milling, corresponded to $0.1 - 4.0 \text{ J/cm}^2$ and $N_{loops} = 50$, respectively.

5.4 Post-processing analysis equipment

The morphological characterization of the laser machined samples was done by using optical, scanning electron (SEM) and atomic force microscopy (AFM) as well as optical profilometry. XPS analyses assessed the surface chemistry immediately after laser irradiation and in the following weeks. The wettability of the surfaces was investigated by contact angle measurements. In this section, all the different setups and devices used for the sample characterization are described.

5.4.1 Nikon Eclipse ME600

An optical microscope equipped with five objectives (magnification of 5X, 10X, 20X, 50X and 100X) and a PC-interfaced digital camera which allows measurements of samples features was used for measuring the craters diameters. A motorized z-axis sample holder allows to precisely focus on the sample surface and to make evaluations of the depth of the ablated structures. Two light sources are provided, thus allowing measurements in both reflection and transmission configurations. The measurements of this thesis were carried out in reflection configuration, being the samples opaque.

5.4.2 SEM Zeiss Sigma

A Field Emission Scanning Electron Microscope (SEM) from Zeiss mod. Sigma was used to analyse the morphology of the laser-induced microstructures and the quality of the micro-machined surfaces. This microscope allows magnification factors up to 500000X, with a resolution of 1:5 nm at a beam accelerating voltage of 15 kV. It is equipped with two detectors. The InLens detector for an efficient detection of the secondary electrons generated by the interaction between the primary electrons beam and the specimen surface. The SE2 detector allows to collect both the secondary and the backscattered electrons. These come from the elastic scattering of primary electrons in a deep range of the interaction volume and carry sample depth information.

5.4.3 Optical profilometer

An optical ContourGT InMotion profilometer with nanometric resolution was used to measure the depth and roughness of the samples. It is a non-contact interferometry-based microscope for analysis of surfaces. Inside an optical interference profiler, the light beam is split; part of the split light is led to a reference arm while the other part is focused on the testing surface. Depending on the difference of the reference arm and the testing arm lengths, constructive and destructive interference occur, thus creating light and dark fringes, which are focused into a digital camera.

5.4.4 AFM

The atomic force microscope (AFM, NT-MDT mod. Ntegra) was used to evaluate the burst-induced LIPSS depth (Δz). The AFM images were acquired in semi-contact mode using a tip apex size of 10 nm at a frequency $f = 263$ kHz. The employed optical head allows viewing the tip-sample positioning during the scan and to achieve 10 nm of resolution. The main part of the AFM apparatus is the optical cantilever (semi-contact NSG10 cantilever used) made of single-crystal silicon with a pyramidal apex. Its deflection system consists of a red diode laser whose spot hits the reflecting surface of the cantilever and a quad-photodiode reveals its intensity variations. The semi-contact operating mode (called tapping-mode) overcomes the issues of friction or/and adhesion occurring in contact mode and that of low resolution by non-contact mode.

5.4.5 XPS

Surface Chemical analysis were performed with X-ray Photoelectron Spectroscopy (XPS) by using a Versa Probe 5000 PHI Spectrometer equipped with a monochromatic Al-X Ray source at low power and a hemispherical analyser in the Fixed Analyser Transmission (FAT) mode. Different regions of the sample surface were scanned by using the mono X-ray source at a power of 25 W and an acceleration voltage of 15 kV, with 100 μm spot size. Survey scans were recorded for all the samples in the range of 0-1400 eV of binding energy, with a pass energy of 187.85 eV. Narrow scan high resolution spectra of C1s, O1s and Fe2p, Ni2p, Cr2p were acquired with a pass energy of 50 eV.

5.4.6 Contact Angles measurements

The most diffused method for evaluating the wettability of a surface is the measurement of the contact angle (CA) of a liquid drop. It is a direct geometric determination [120] based on the direct measurement of the tangent angle at the three-phase contact point, called triple point, of a sessile drop of a test liquid, e.g. water, placed on a surface to investigate (Fig. 53a).

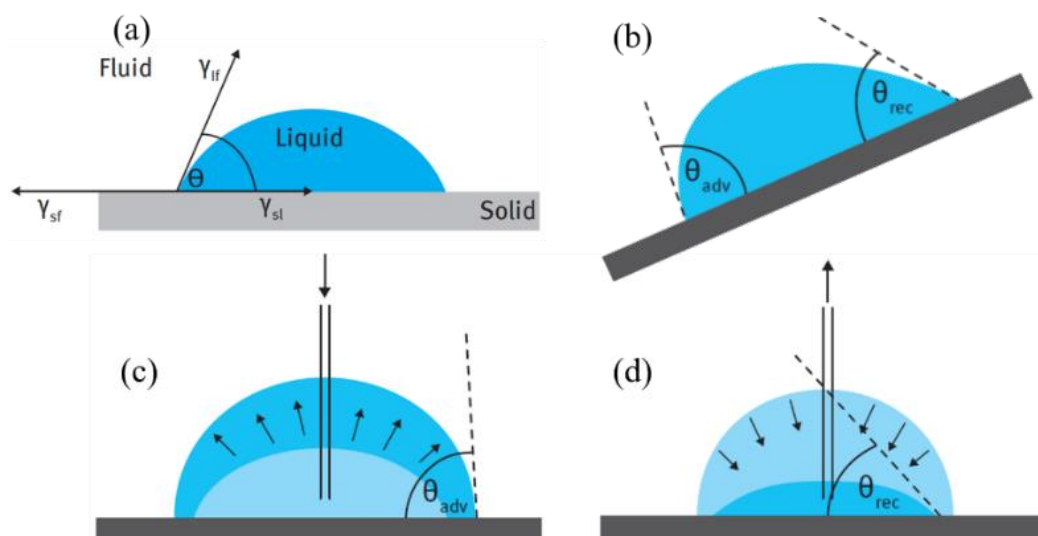


Fig. 53 (a) CA, θ , of a sessile drop between a liquid l and a solid s , immersed in a fluid f , air generally. (b) Drop profile on tilted surface: advanced and receding CA are shown. (c-d) Determination of the advancing and receding angle of the sessile drop by increasing and decreasing the volume of the drop. [120]

The CA measurement was done through a quite simple apparatus consisting of three components (Fig. 54): a sample holder stage, a light source for the

illumination of the drop placed on the sample (typically 2–5 μl), and an image capture system on the opposite side. The accuracy of this method is $\pm 2^\circ$. To improve the reliability and accuracy of the analysis, a graduated micro-syringe for dispensing the liquid drop and a camera (Dino-Lite) to acquire both photographs and movies were used. The acquired movies were useful to evaluate the dynamic CA. Usually, a liquid drop has a non-symmetric profile when placed on a tilted surface. This means that the CA on both sides of the liquid drop profile are different (Fig. 53b) and called advancing and receding CA, respectively. The difference between them, called hysteresis, represents the dynamic CA value.

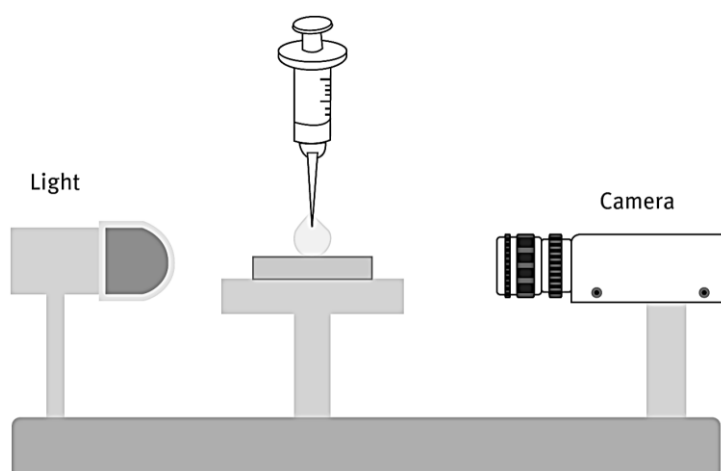


Fig. 54 Sketch of the setup for contact angle measurements. [120]

From the operative point of view, the advancing and receding CA evaluation were accomplished by measuring the CA while increasing and decreasing the volume of the drop during the analysis, keeping the needle of the syringe inside the drop, as shown in Fig. 53c-d [120]. The volume of the liquid drop placed on the sample is slowly increased for small added volume. The measured CA increases but the triple-phase contact line remains stuck. For a certain drop size, the line front starts to move, without the CA increases more: that is the advancing CA (Fig. 53c). On the contrary, for the receding CA (Fig. 53d). The liquid is slowly withdrawn, reducing the drop volume and the CA while the triple-phase contact line remains stuck. When the contact line starts to retreat, the acquired CA is the receding one.

Finally, the acquired photos and movies were analysed by ImageJ software for the elaboration of the drop shape and the CA estimation.

Chapter 6

Influence of burst features on ablation

This chapter reports on the experimental investigation of the ablation threshold fluence, the incubation effect and the ablation efficiency on stainless steel targets when bursts of ultrashort laser pulses are used. Several works have already addressed the study of the reduction of the ablation threshold owing to incubation, when trains of ultrashort laser pulses were used in the kHz to MHz repetition rates regime.

The present work tries to reveal whether the incubation effect depends on the burst features, i.e. the number of sub-pulses and intra-burst time delay, when bursts of sub-pulses with picosecond time delays are employed. In detail, the dependence of the incubation coefficient with the burst features was experimentally investigated. Afterwards, the influence of the number of sub-pulses per burst and their time spacing on the ablation efficiency was studied. Results of these experiments are compared with data available from literature.

The studies on threshold fluence and incubation were conducted using the AFS laser source providing laser pulses with pulse duration (FWHM) of 750-fs (measured by the autocorrelator, (Fig. 49a) at a wavelength of 1030 nm, while for the experiments on the ablation removal rate, the Pharos laser was used, which produces 238-fs pulses (Fig. 49b) at the same wavelength.

6.1 Ablation threshold fluence with bursts of pulses

The laser ablation threshold fluence F_{th} has been estimated by using the method proposed by Liu [23], based on the experimental measurement of the size of ablation craters obtained at different laser fluences. The craters were produced by focusing the laser beam on the sample surface. Assuming a Gaussian profile for the spatial energy distribution of the laser beam, the threshold fluence F_{th} is related to the crater diameter D , by the following equation:

$$6.1 \quad D^2 = 2w^2 \ln \left(\frac{F_0}{F_{th}} \right)$$

where w is the laser spot radius on the sample surface and F_0 is the peak laser fluence given by:

$$6.2 \quad F_0 = \frac{2 E_p}{\pi w^2}$$

where E_p is the pulse energy. Interestingly, this method is based on the assumption that the ablated diameter is only function of the beam energy profile because the pulse duration in the ultrashort regime implies negligible heat diffusion.

First of all, the ablation threshold fluence was evaluated in case of NPM at fixed laser repetition rate of 100 kHz, varying the pulse energy in the range $5 - 25 \mu\text{J}$. After irradiation of $N = 50$ circularly polarized pulses, the experimental crater diameters were measured with the optical microscope and plotted as a function of the pulse energy E_p , as shown in Fig. 55 (pink points). Five replicas for each E_p have been performed for averaging the results. In order to estimate the ablation threshold, these points were fitted by the function $D^2 = D^2(E_p)$, which results from the combination Eqs. 6.1 and 6.2. Graphically, the intercept between the fitting curve and the x-axis corresponds to the minimum pulse energy able to generate a crater, $D \neq 0$. The fit parameters return also the w value, hence, the ablation threshold fluence can be evaluated from Eq. 6.2.

The evaluated threshold was indicated as $F_{th}(50)$ since it refers to the case of $N = 50$ pulses. In fact, due to incubation (see section 1.4), the threshold fluence depends on the number of impinging pulses. The same experiments were repeated also for $N = 100, 200, 400, 800, 1600$ pulses (shown in Fig. 55) in order to gather enough data to determine the incubation factor in NPM as it will be described in the next section.

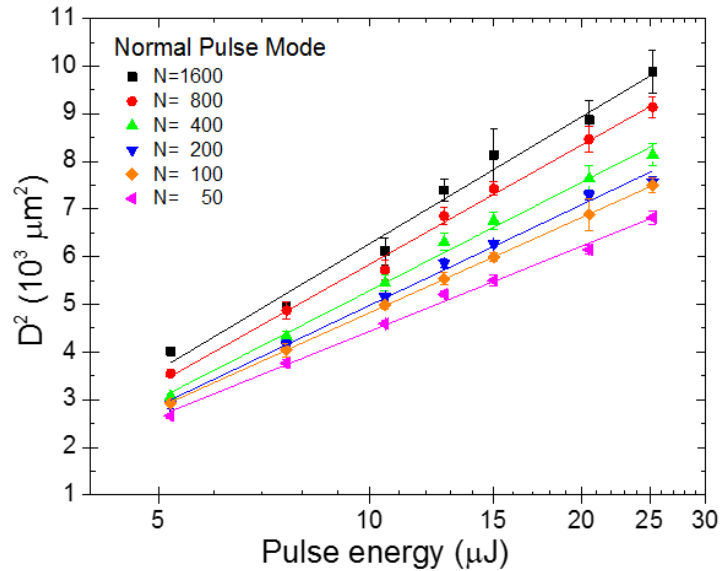


Fig. 55 Semi-log plot of squared diameters of ablated craters in stainless steel versus pulse energy for $N = 50, 100, 200, 400, 800, 1600$ number of pulses at 100 kHz and 750 fs in pulse duration.

Similarly to the NPM case, experiments were carried out in BM by employing different burst configurations. Bursts with different number of sub-pulses ($n = 2, 4, 8, 16, 32$), two intra-burst delays Δt (1.5 ps and 3 ps), and variable burst energy E_b in the range 5-25 μJ , were used. The number N of bursts in BM, originated by splitting N pristine laser pulses, was also varied from 50 to 1600. Table 6-1 reports a summary of the set of parameters used for the ablation experiments.

Table 6-1 Summary of investigated working parameters in BM.

Number of sub-pulses in the burst, n	2	4	8	16	32
Time delay between sub-pulses, Δt	1.5 ps 3 ps	1.5 ps 3 ps	1.5 ps 3 ps	1.5 ps 3 ps	1.5 ps
Burst energy, E_b	5 – 7.5 – 10 – 12.5 – 15 – 20 – 25 μJ				
Number of bursts, N	50 – 100 – 200 – 400 – 800 – 1600				

The plots in Fig. 56 report the ablated craters diameters squared as a function of the sub-pulse energy E_{sp} for bursts with 16 sub-pulses and intra-burst time delay of 1.5 ps and 3 ps, respectively. The threshold fluence for each number of bursts have been estimated as in NPM, by fitting the experimental data with fixed number N of bursts.

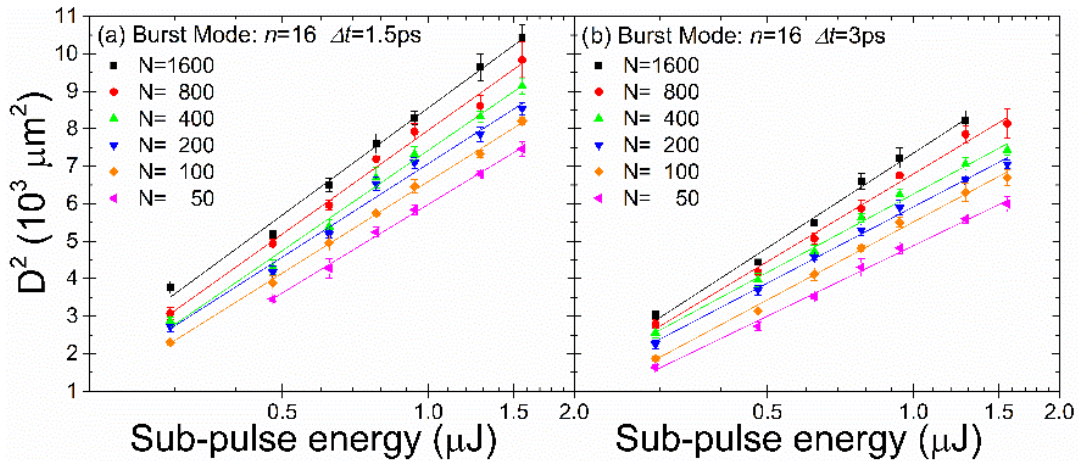


Fig. 56 Semi-log plot of squared diameters of the ablated craters in stainless steel versus sub-pulse energy for bursts with $n = 16$ sub-pulses and intra-burst time delay of (a) $\Delta t = 1.5 \text{ ps}$ and (b) $\Delta t = 3 \text{ ps}$, when irradiated with $N = 50, 100, 200, 400, 800, 1600$ bursts at the burst repetition rate of 100 kHz. [121]

Results in Fig. 56 show a linear dependence of the measured quantities on semi-log plots for each value of investigated N . This trend was confirmed for all the combinations of explored parameters reported in Table 6-1. Next to threshold fluence, the fits also return the beam spot size w on the target surface. The resultant average value of the laser spot radius was $43.1 \pm 3.8 \mu\text{m}$. The small error indicates that all experiments were performed under uniform focusing conditions.

In Fig. 57 the ablation thresholds obtained in BM processing as well as in NPM have been compared and plotted as a function of the total number of sub-pulses, $N_{tot} = N \cdot n$, for both intra-burst time delays of 1.5 ps and 3 ps , respectively. It is worth mentioning that N_{tot} in NPM is equal to N because the pristine pulse can be considered as a burst with a single sub-pulse ($n = 1$). As expected, a decrease of the threshold fluence was clearly observed in case of NPM (black squares) as N_{tot} increases. This result is in agreement with literature and can be ascribed to incubation [11,21,26,28,29,31]. A similar trend is noticed for each investigated burst configuration as the total number of impinging sub-pulses increases. However, the threshold fluence with bursts is generally lower than the NPM value.

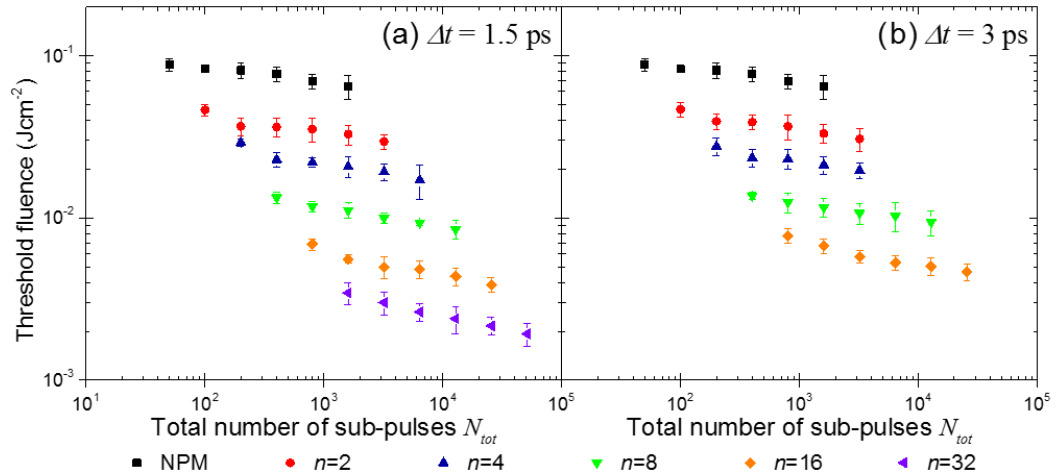


Fig. 57 Bi-log plots of threshold fluence as a function of the total number of sub-pulses $N_{tot} = N \cdot n$. The time delay between consecutive sub-pulses in the burst is (a) $\Delta t = 1.5 \text{ ps}$ and (b) $\Delta t = 3 \text{ ps}$. [121]

In Fig. 57 it is evident that the decrease of damage threshold in BM for increment of N_{tot} is mainly due to the growth of the number of sub-pulses constituting the burst, rather than the number of bursts itself. In fact, for $\Delta t = 1.5 \text{ ps}$ (Fig. 57a) a threshold reduction of 93% was found when increasing N_{tot} from 100 to 1600, while keeping the same number of bursts $N = 50$ and just changing the number of sub-pulses per burst from 2 to 32. Similarly, 83%

reduction of the threshold fluence was observed for $\Delta t = 3 \text{ ps}$ and $N = 50$ (Fig. 57b), when increasing the number of sub-pulses from 2 to 16, and thus increasing N_{tot} from 100 to 800. On the other hand, the threshold fluence shows a slower decrease when increasing the number of bursts N and keeping the same number of sub-pulses n . This can be observed in e.g. the cases of $\Delta t = 1.5 \text{ ps}$, $n = 2$, and N from 50 to 800 and $\Delta t = 3 \text{ ps}$, $n = 2$ and N from 50 to 400. In both of these cases, the measured reduction of the threshold fluence was 28%.

A further characteristic result emerging from the analysis of the experimental data obtained in BM was that for a fixed total number of sub-pulses N_{tot} different damage threshold values were found for each combination of N and n . This is better highlighted in Table 6-2 where data for $N_{tot} = 1600$ in BM are summarized.

Table 6-2 Threshold fluences for the combinations of N and n giving $N_{tot} = 1600$.

Number of bursts N	Sub-pulses in the burst n	Total number of sub-pulses N_{tot}	Threshold fluence F_{th} (J/cm ²)	
			$\Delta t = 1.5 \text{ ps}$	$\Delta t = 3 \text{ ps}$
800	2	1600	0.0328 ± 0.0045	0.0332 ± 0.0044
400	4		0.0207 ± 0.0030	0.0211 ± 0.0032
200	8		0.0111 ± 0.0012	0.0116 ± 0.0015
100	16		0.0056 ± 0.0003	0.0067 ± 0.0007
50	32		0.0034 ± 0.0005	

6.2 Incubation with bursts

In section 1.4 the main incubation models describing the threshold fluence variation when processing with multiple pulses have been reviewed. All the models refer to multiple irradiation in NPM and, apparently, no study has investigated yet the incubation effect with bursts of ultrashort pulses. From the results of the previous section, different values of threshold fluence have been found for a given total number of sub-pulses. This is not envisaged by any of the incubation models that return one single value of threshold fluence once the number of impinging pulses is fixed [11,21,25,31,32]. This indicates that the burst features have an influence on incubation. To take into account of this effect the well-known Jee's model [21] developed for NPM (Eq. 1.21) has been extended to fit also experimental data of BM processing. In that

aim, same adaptations were done. First of all, a dependence of the incubation factor (which is now indicated as S_n and is no longer a constant value as in NPM) on the characteristics of the bursts was introduced:

$$6.3 \quad F_{th,b}(N) = F_{th,b}(1) \cdot N^{(S_n-1)}$$

where $F_{th,b}(N)$ represents the threshold fluence with N bursts, while $F_{th,b}(1)$ is the threshold fluence for a single burst.

It is worth noticing that Eq. 6.3 represents also the case of NPM when $n = 1$. In order to estimate the incubation factor, the $F_{th,b}(N)$ values were plotted as a function of N and fitted by Eq. 6.3. As an exemplary case, in Fig. 58 the experimental data related to bursts with 16 sub-pulses are reported on bi-log plots and compared to NPM. As it can be seen, the extended incubation model (Eq. 6.3) was found to fit well the experimental data ($R^2 > 0.93$). Such result has been confirmed for all the investigated burst features.

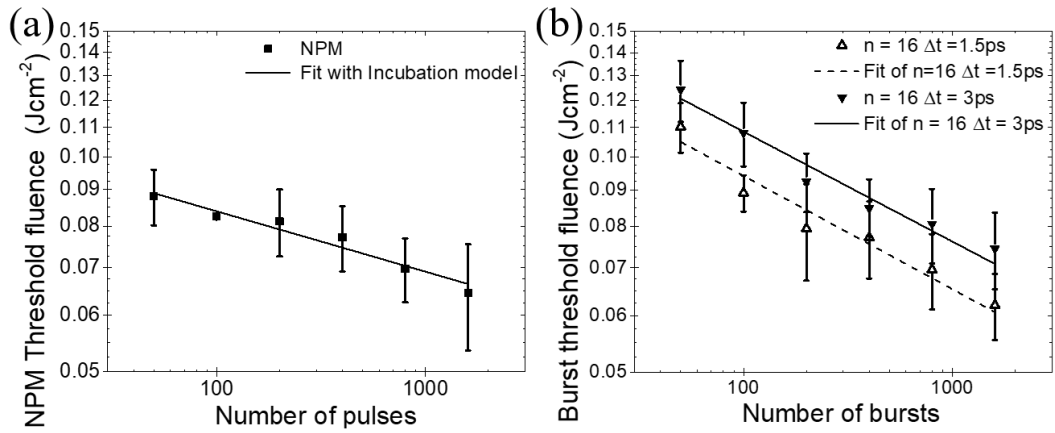


Fig. 58 (a) Threshold fluence as a function of the number of laser pulses in NPM processing. (b) Burst threshold fluence as a function of the number of bursts for two burst configurations: $n = 16, \Delta t = 1.5 ps$; $n = 16, \Delta t = 3 ps$. The experimental points for NPM and BM were fit with Eq.6.3.

From the slope of the fit the incubation factor S_n for each investigated burst configuration of n and Δt (Table 6-1) was obtained and its dependence from n is shown in Fig. 59. The value of the incubation coefficient obtained in NPM was also reported in Fig. 59 (dotted line) for comparison. The NPM incubation coefficient, which is equal to 0.91, was in very good agreement with values reported by Di Niso and Mannion [11,31] for stainless steel.

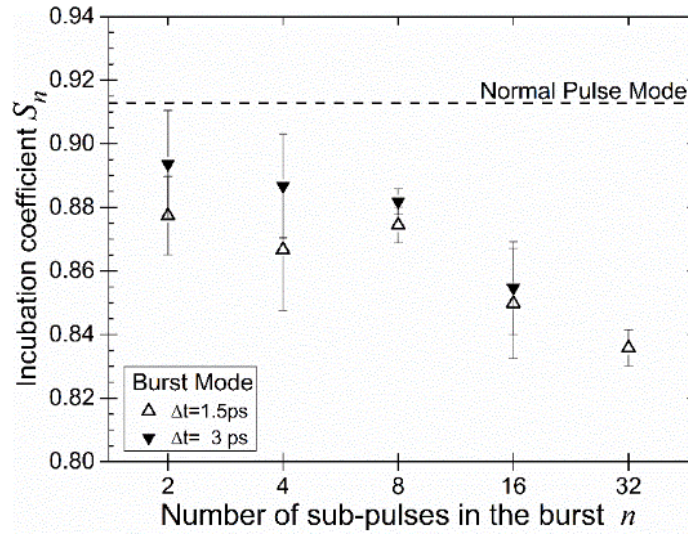


Fig. 59 Incubation coefficient S_n versus the number n of sub-pulses in the burst for the two different time delays, 1.5 and 3 ps. The dashed line represents the incubation coefficient in case of Normal Pulse Mode. [121]

It can be observed that the BM incubation coefficient S_n noticeably decreases with the number of sub-pulses in the burst, thus revealing that the higher the pulse splitting, the stronger is the incubation effect, independent of the time separations. It can also be seen that the NPM incubation factor was always higher than in BM, thus indicating that the use of bursts enhances the incubation effect.

The origin of the increased incubation observed when using bursts of pulses can be of different nature, like e.g. damage accumulation that weakens the molecular bonding, changes in the surface chemistry and/or topography.

All these mechanisms may contribute to the lowering of the damage threshold and/or to the variation of the absorption length, so that the deposited energy is increased during multi-burst laser irradiation [30].

Finally, the experimental data of the incubation factor were compared with the results of numerical solutions of TTM presented in Chapter 4. From the results of the numerical simulations on the temporal and spatial evolution of the lattice temperature after laser irradiation with single pulse or single burst with two and/or four sub-pulses with 1.5 and 3 ps delays, respectively, it was found that the laser energy needed to reach the melting temperature was always lower in BM than in NPM. Moreover, it diminished as the pulse splitting increased (as shown in Table 4-1 from $n = 2$ to $n = 4$). Although results of the numerical simulations are limited to single burst with maximum pulse splitting of 4 sub-pulses, they indicate a clear trend which is expected to be enhanced in case of multi-burst irradiation and higher pulse splitting.

It was further experimentally demonstrated that the intra-burst time delay influences the incubation effect. In fact, a lower incubation factor was found for 1.5 ps time delay between sub-pulses compared to the 3 ps case, as shown in Fig. 59. This was also in agreement with the numerical results, which showed that the longer the time delay the higher was the laser input energy needed to reach melting temperature (Table 4-1).

6.3 Ablation removal rate with bursts

A reduced ablation threshold owing to the enhanced incubation, which occurred in burst mode processing, should in principle lead to an increase of the ablation efficiency. In order to ascertain whether such beneficial effect is actually found in terms of increased ablation removal rate, laser milling experiments were conducted in BM processing and compared to NPM. The impact of burst features (i.e. number of sub-pulses in the bursts and intra-burst time delay) on material removal rate was also investigated. Squared pockets with surface area of $0.5 \times 0.5 \text{ mm}^2$ were milled on stainless steel targets.

All the milling experiments have been performed adopting the same scanning strategy, which consisted of parallel hatching with scan speed of $v = 0.96 \text{ m/s}$ and hatch distance $H = 5 \text{ }\mu\text{m}$ corresponding to 5 pps overlap being the spot radius $w_0 = 12 \text{ }\mu\text{m}$ (at $1/e^2$ peak intensity measured by a CCD camera). The experiments were carried out with several burst configurations to evaluate the influence of the burst features on the material removal rate. The depth d of each milled pocket was measured using a white light interference profilometer. In the investigated range of laser fluence, from 0.1 to 4 J/cm^2 , 50 scan loops (N_{loops}) were performed in order to obtain appreciable pocket depths to be measured by the optical profilometer. In Fig. 60 the pocket depths as a function of the burst fluence are plotted for bursts with variable number of sub-pulses with fixed delay $\Delta t = 1.5 \text{ ps}$. While in Fig. 61, analogous plot is reported with data obtained with bursts of double sub-pulse with different time delays. In both graphs the results obtained in NPM are also reported for comparison. The ablation depth results influenced by the burst features in the following way:

- splitting the burst fluence in more sub-pulses reduces the overall depth of the packet (Fig. 60);
- for burst of double sub-pulses, the depth decreases with the intra-burst delay (Fig. 61);
- for a given total amount of laser fluence the pockets milled in NPM processing were always deeper than BM.

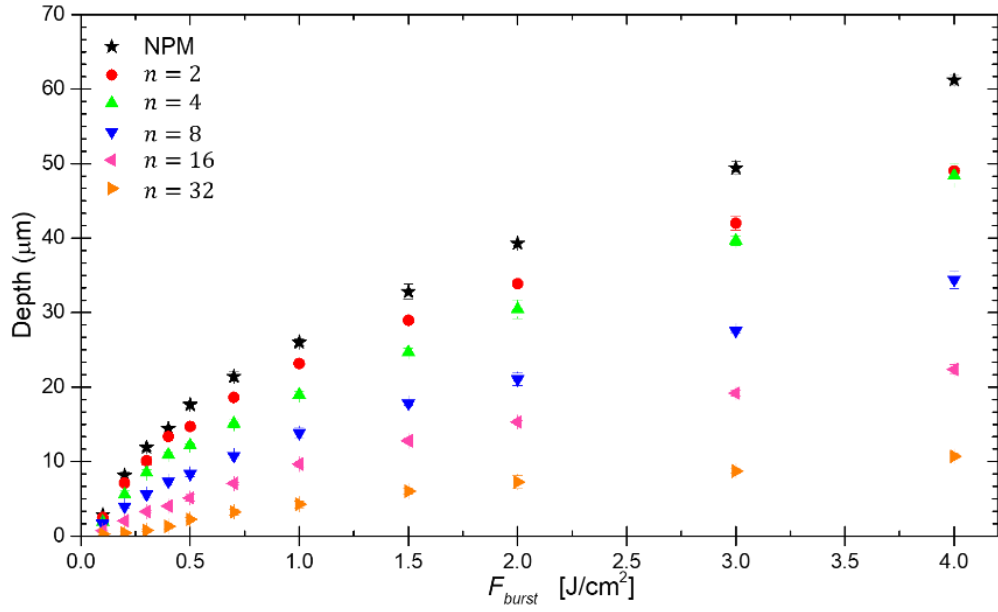


Fig. 60 Ablated depth as a function of the burst fluence for different burst configurations with number of sub-pulses of 2,4,8,16,32 and fixed intra-burst time delay of 1.5 ps. The normal pulse mode depth is reported for a comparison.

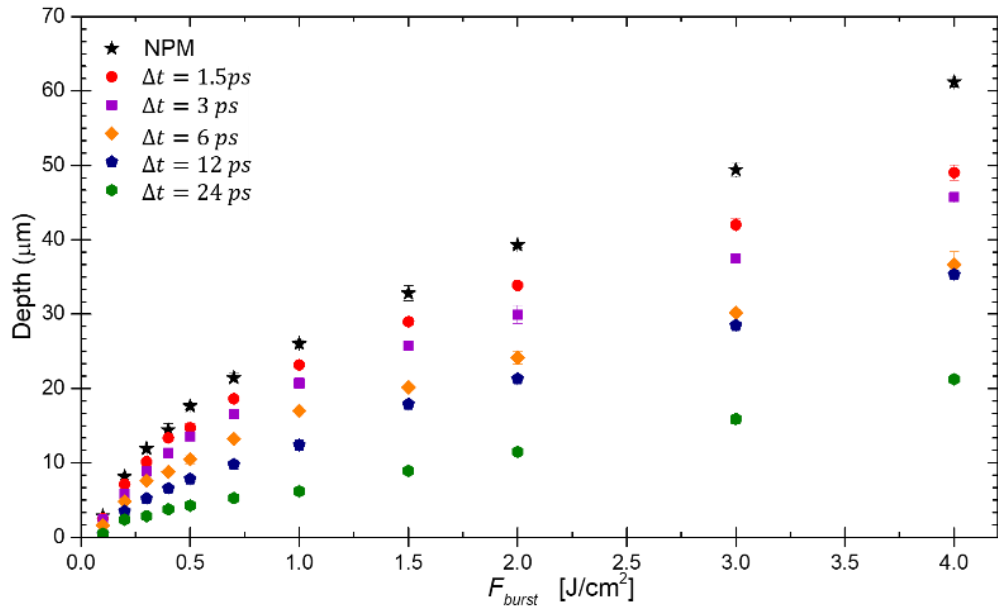


Fig. 61 Ablated depth as a function of the burst fluence for different burst configurations of double-sub-pulse with time delay of 1.5, 3, 6, 12, 24 ps. The normal pulse mode depth is reported for a comparison.

For each burst configuration and for NPM has been evaluate the specific removal rate that has been defined by Neuenschwander et al. [7] as:

$$6.4 \quad \frac{\dot{V}}{P_{av}} = \frac{\Delta V}{E_{sp}} = \frac{d A_{pps=1}}{n N_{loop}} \frac{f n}{P_{av}}$$

This quantity represents the volume of material ΔV ablated by each sub-pulse divided by the sub-pulse energy E_{sp} . Being known the laser repetition rate f and the beam average power P_{av} , the sub-pulse energy is calculated as $E_{sp} = P_{av}/(f n)$. Whereas, the ablated volume can be estimated assuming that all the sub-pulses in the burst ablate the same amount of material. If so, the ablated volume can be approximated to a parallelepiped of height $d/(n N_{loop})$ and area $A_{pps=1} = \Delta x \cdot \Delta y$, where Δy is the hatch distance ($\Delta y = H$) and Δx is the pitch between two consecutive spots. From the data plotted in Fig. 60 the specific removal rates for bursts with fixed $\Delta t = 1.5$ ps have been calculated and reported in Fig. 62 as a function of the fluence of the single sub-pulse in the burst, F_{sp} . The specific removal rates achieved in NPM are also plotted.

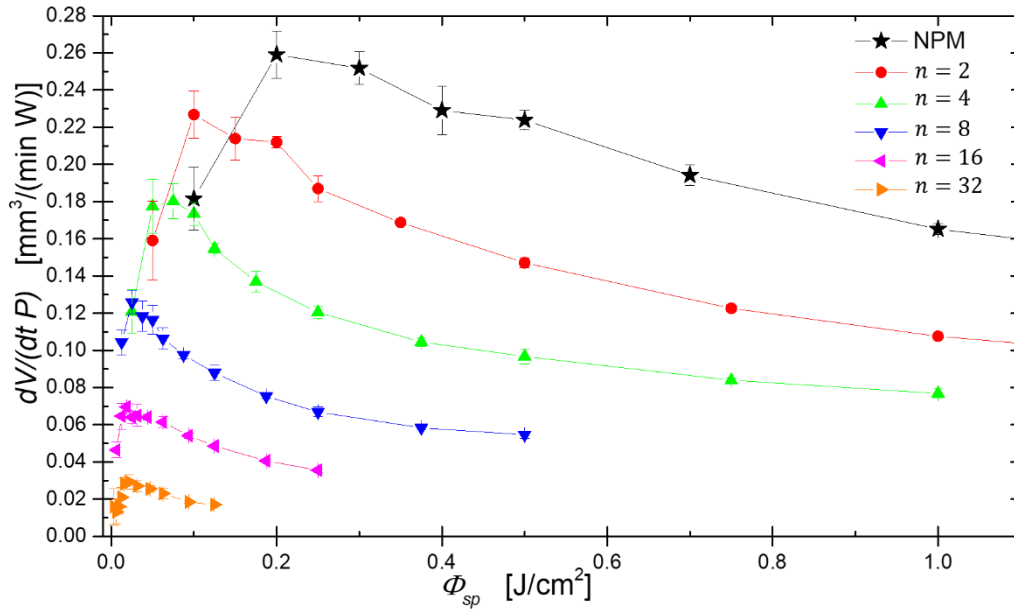


Fig. 62 Specific removal rates for different number of sub-pulses in a burst at fixed intra-burst time delay of 1.5 ps. NPM is reported as a reference. The solid lines represent guides to the eye.

Also from this graphical representation it can be noticed that the highest specific removal rate value is achieved in NPM at an optimal pulse fluence around 0.2 J/cm². However, for each subset of data the optimum sub-pulse fluence maximizing the specific removal rate shifts towards lower values as far as the number of sub-pulses in the bursts is increased. Therefore, there is

a specific range of sub-pulse fluences, i.e. below 0.22 J/cm^2 , where an advantage in terms of specific removal rate can be achieved by operating in BM processing instead of NPM. This happens, for instance, when using bursts with two sub-pulses at a sub-pulse fluence of around 0.1 J/cm^2 . From Fig. 62 it can be noticed that in this BM processing window the removal rate is higher than NPM. This advantageous situation of BM is only achieved for intra-burst delays of 1.5 ps. Indeed, Fig. 63 shows that as far as the double-pulse intra-burst delay gets longer, the specific removal rate decreases. It drops below the NPM value already for delays longer than 3 ps.

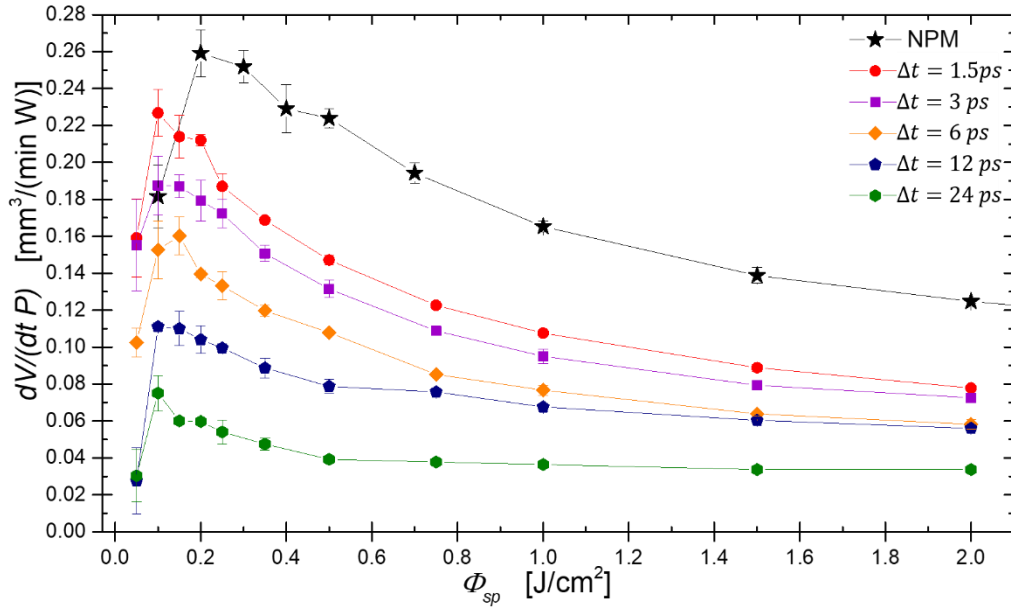


Fig. 63 Specific removal rates for different time spacing between the two sub-pulses of the burst. NPM is reported as a reference. The solid lines represent guides to the eye.

In conclusion, the only burst configuration which resulted more advantageous than NPM in the low sub-pulse fluence regime was $n = 2, \Delta t = 1.5 \text{ ps}$.

The observed trends of the specific removal rates with burst of 238-fs sub-pulse and intra-burst time delays on the picosecond timescale resulted different from those found by Neuenschwander et al. [7] with bursts of 10 ps pulses and time delay of 12 ns. They found that for applied fluences above the NPM optimum value, the specific removal rate with bursts of 4, 6, 8 sub-pulses was higher than NPM.

They ascribed the observed reduction of the maximum specific removal rate in BM to the plasma shielding i.e. the consecutive sub-pulses in the burst were partially shielded by the plasma produced by the previous pulses. Nevertheless, the plasma shielding is stronger in nanosecond scale. In case

of time delay in picosecond scale, the shockwave (SW) is probably involved in the shielding and/or scattering of the following sub-pulses in the burst, as shown in other works [41,43]. This explains results of Fig. 62 and Fig. 63. Therefore, from the results presented in this chapter the following conclusions can be drawn: (i) incubation is strongly enhanced during BM processing compared to NPM which leads to a remarkable reduction of the threshold fluence when bursts of pulses are employed; (ii) such a reduction of the threshold fluence does not lead to higher ablation removal rates during laser milling with bursts of pulses. This is explained since threshold effects like incubation refer to the very early stage of the ablation process when the specific removal rates are extremely low. Therefore, there is no real connection between incubation effect and higher ablative regimes which occur at much higher laser fluences.

Chapter 7

Influence of burst features on LIPSS

An experimental study on laser-induced periodic surface structures (LIPSS) of steel samples using bursts of femtosecond laser pulses is presented in this chapter. By varying the burst features and adjusting the process parameters, different types of nanostructures have been observed and characterized by scanning electron microscopy and atomic force microscopy.

In the first part, the influence of the burst features on 1D-LIPSS formation has been treated. These were generated using LP bursts, i.e. linearly polarized sub-pulses with parallel polarization. The LSFL morphology has been systematically investigated as function of the number of sub-pulses and fixed intra-burst delay and also for variable time delay in case of burst of double sub-pulses.

In the following part, two-dimensional surface structures fabricated in a single-step process by irradiating the samples with bursts of cross-polarized and circularly polarized sub-pulses, will be analysed. Well-defined triangular 2D structures with hexagonal arrangement and period less than 1 micrometer were generated in narrow windows of process parameters depending on the burst features.

Finally, the wettability properties of the different surface patterns fabricated by bursts have been assessed and the findings have been supported by XPS surface chemistry analyses.

7.1 1D LIPSS

Several parameters play a key role in the LIPSS generation, as discussed in Chapter 3. In the experiments presented in this thesis work, the laser wavelength and the angle of incident were kept fixed at 1030 nm and 0° (normal incident), respectively. The employed ultrashort pulse duration of 238 fs was not varied. Both LSFL and HSFL were generated by irradiation with bursts of ultrashort laser pulses. However, the latter were only marginally investigated. As already observed in literature, linear LIPSS (1D-LIPSS) have been produced by LP pulses. During the experiments the polarization was oriented perpendicularly to the laser scanning line direction. In fact, the orientation of the laser polarization (P) with respect to the scan direction (v) represents a crucial parameter, as can be observed in Fig. 64.

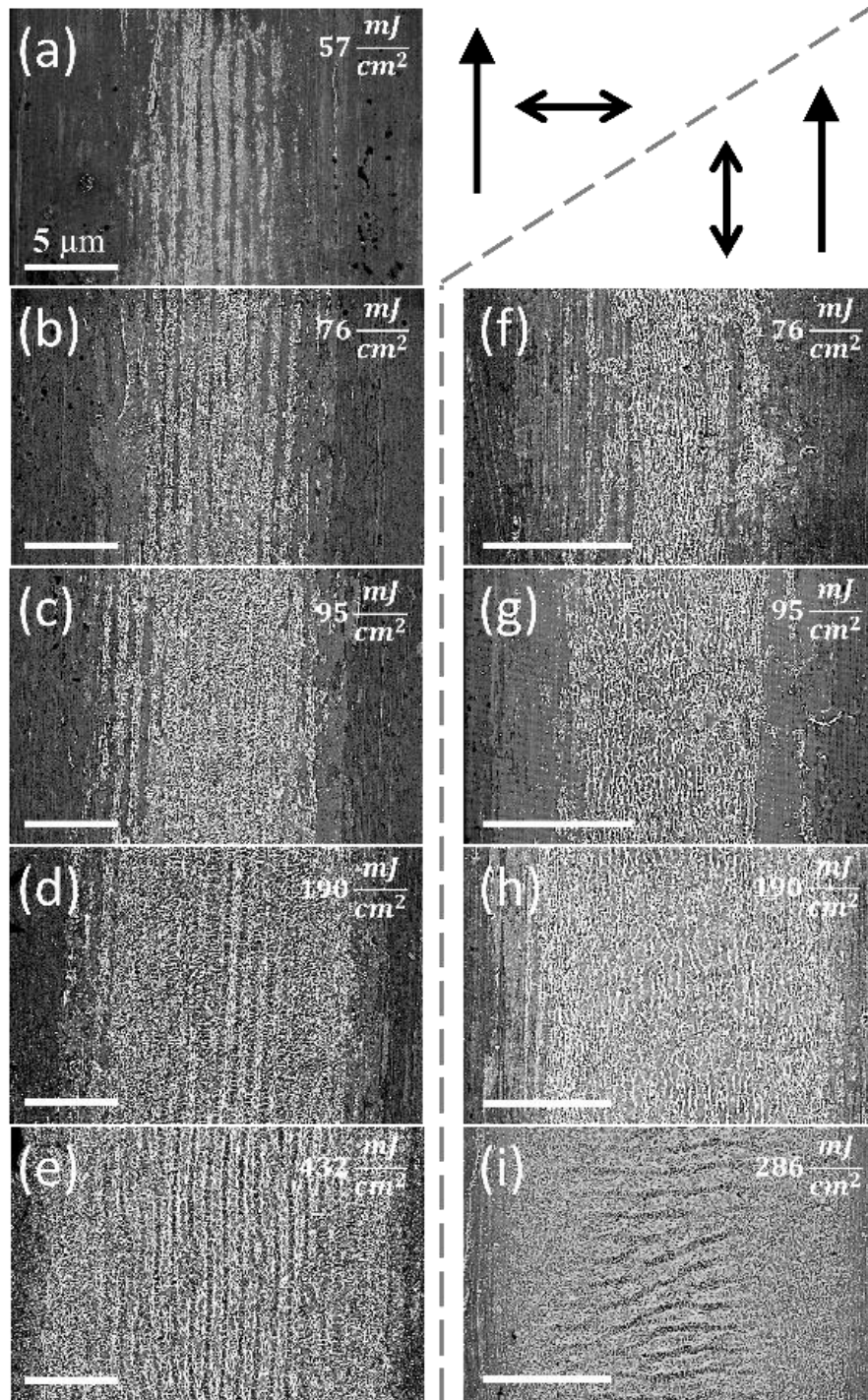


Fig. 64 SEM micrographs of single scan lines on the stainless steel surface irradiated in NPM. Effect of the orientation of the laser polarization and of the laser fluence on the nanostructures generation. The pulses linear polarization was aligned along (a-e) the orthogonal direction or (f-i) parallel to the scan lines. Scan speed and laser repetition rate were fixed at 1 m/s and 200 kHz, respectively. The double arrow indicates the direction of LP. The white bars represent a length of 5 μm .

The nanoripples obtained in NPM changing the polarization direction from orthogonal (Fig. 64a-e) to parallel (Fig. 64f-i) were always perpendicularly oriented to the laser polarization direction. As expected [122], the LSFL appeared at relatively low fluence. The most homogeneous and regular ripples, exhibiting less interruptions, were obtained for polarization and laser writing direction perpendicular between them (Fig. 64a-e). Therefore, the latter strategy ($P \perp v$) was employed for texturing samples over larger surface areas. From Fig. 64 it can be noticed that as a consequence of the Gaussian intensity profile of the incident beam the LIPSS started to form in the central part of the line and extended towards the tails only when the laser fluence was increased. Therefore, the combination of the laser fluence and the pulses overlap along the scan line need to be optimized to produce homogeneous LIPSS.

The experiments for LIPSS formation with bursts were addressed to study whether the LIPSS morphology was affected from burst features, i.e. number of sub-pulses and intra-burst time delay. Therefore, experiments were conducted with bursts of double sub-pulses ($n = 2$) and variable delays from 1.5 ps to 24 ps but also with bursts of sub-pulses from $n = 2$ to 32, delayed of 1.5 ps. LIPSSs were observed on stainless steel with any LP burst feature. Fig. 65 shows the laser-induced structures by single scanning line when bursts with different n were used. All the samples exhibited the same type of ripples with spatial period close to the laser wavelength, i.e. LSFL oriented perpendicular to the laser beam polarization.

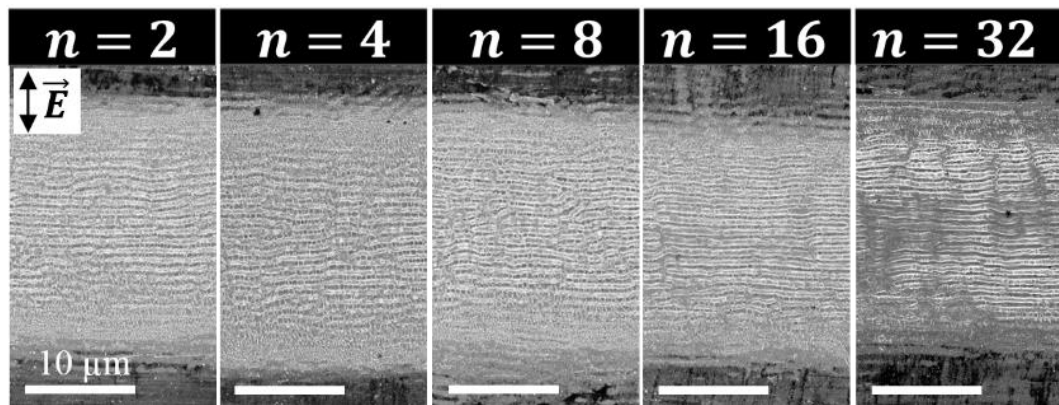


Fig. 65 SEM micrographs of the stainless steel surface irradiated by LP bursts. The images are relative to the single scan line with increasing number of sub-pulses, from $n = 2$ (on the left) to $n = 32$ (on the right) delayed of 1.5 ps. Scan speed and laser fluence were fixed at 1 m/s and 0.85 J/cm^2 , respectively. The double arrow indicates the direction of LP. The white bars represent a length of $10 \mu\text{m}$.

The laser fluence and the pulses overlap along the scanning line were optimized for all burst configurations to produce uniform LIPSS. In detail, $F = 0.85 \text{ J/cm}^2$ and $P^H = 79.2\%$, calculated from Eq. 5.4 (repetition rate $f = 200 \text{ kHz}$, scan speed $v = 1 \text{ m/s}$, laser spot diameter $d = 24 \text{ }\mu\text{m}$). It is worth mentioning that for the given scan speed and intra-burst delay, the spatial distance between consecutive sub-pulses in the burst is in the picometers range. Therefore, it can be assumed that the whole burst hits the same laser spot area as for NPM.

After optimizing the hatch distance between successive scanning lines LIPSS distributed over large areas have been produced. The optimum hatch distance value was $10 \text{ }\mu\text{m}$. Fig. 66 and Fig. 67a show representative SEM images of laser structured areas. The qualitative analysis of the acquired images revealed that LIPSS morphology changes with the burst features.

In particular, for $n = 2$, $\Delta t = 24 \text{ ps}$ (Fig. 66a) and $n = 32$, $\Delta t = 1.5 \text{ ps}$ (Fig. 66i), some defects, such as interruptions and/or bifurcations of ripples, can be noted. On the other hand, for shorter time delays and lower number of sub-pulses, LIPSS with sharper edges and few defects were obtained. HSFL are also observed along the LSFL valleys, especially when bursts with high number of sub-pulses have been used ($n > 8$), as shown by the zoomed inset of Fig. 66h-i. The HSFL are parallel to the laser polarization and orthogonal to the LSFL.

To quantify the morphology changes of the LSFL related to different bursts configurations, the structures were characterized by further processing the SEM images to evaluate the LIPSS spatial period Λ and by using an atomic force microscope (AFM) to measure their depth Δz . Several SEM micrographs were acquired on diverse areas for each sample generated by different burst configurations. Then, each image was processed by Gwyddion software that performed the 2-dimensional fast Fourier transform (2D-FFT) to determine the LSFL spatial period.

As an example, Fig. 67 shows the SEM image of the LSFL generated by bursts of $n = 16$ sub-pulses with intra-burst delay of $\Delta t = 1.5 \text{ ps}$, while Fig. 67b reports the related 2D-Fourier Transform spectrogram. For each spatially periodic structure present in the image, the Fourier transform highlights a set of peaks (bright dots) in the secondary reciprocal space.

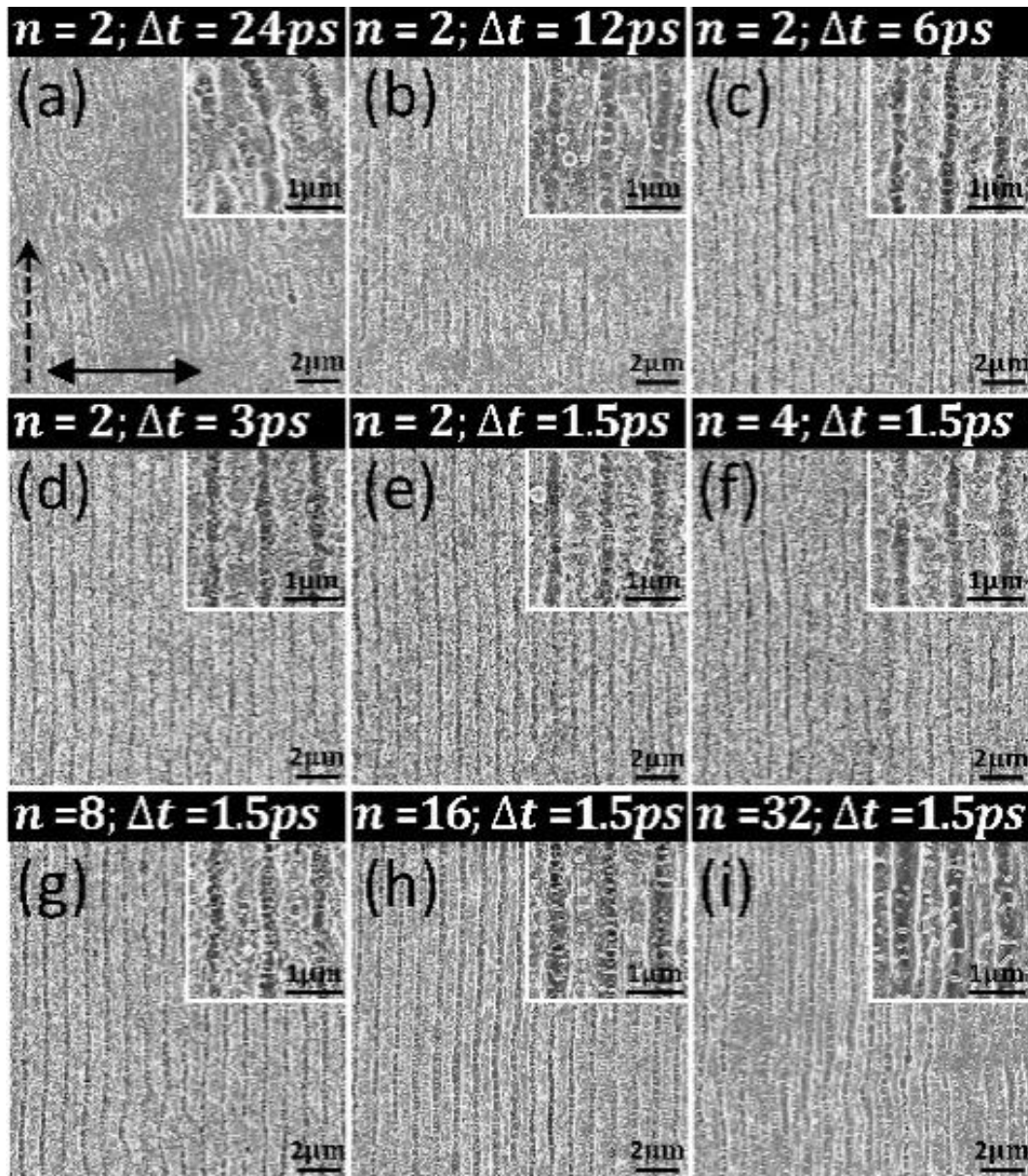


Fig. 66 SEM micrographs of the stainless steel surface irradiated by bursts with a fluence of 0.85 J/cm^2 , scan speed of 1 m/s and line scan distance of $10 \text{ } \mu\text{m}$. The images (a-e) are relative to bursts of double sub-pulses and decreasing time separation: (a) $\Delta t = 24 \text{ ps}$, (b) $\Delta t = 12 \text{ ps}$, (c) $\Delta t = 6 \text{ ps}$, (d) $\Delta t = 3 \text{ ps}$ and (e) $\Delta t = 1.5 \text{ ps}$. From (e) to (i) the time delay is fixed at 1.5 ps while increases the number of sub-pulses inside the burst: (e) $n = 2$, (f) $n = 4$, (g) $n = 8$, (h) $n = 16$ and (i) $n = 32$. The inset pictures show a zoomed view of the ripples. HSFLs are clearly observed for the texturized surface by bursts with $n > 4$. The double arrow indicates the direction of pulses polarization while the dotted arrow the laser scanning direction. [123]

The distance of the circled bright dots in Fig. 67b to the zero spatial frequency lets to evaluate the spatial period of the ripples in the SEM image of Fig. 67a. In Fig. 67b, the other bright dots (not circled) in the FFT at higher frequencies are only artefacts of the FFT algorithm which are originated by deviations of LIPSS frequency from the harmonic function, as also reported in [71,80].

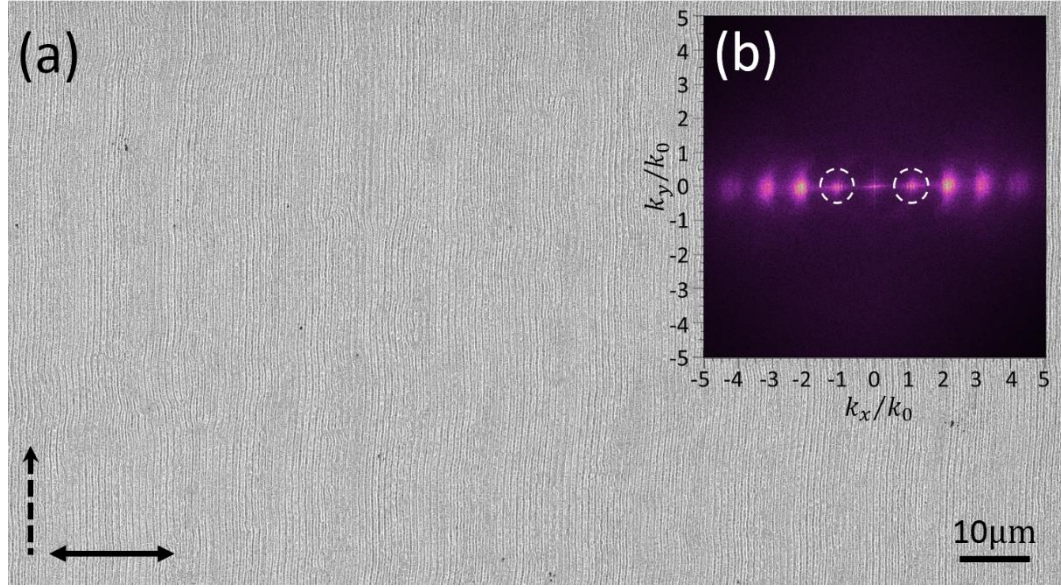


Fig. 67 (a) SEM micrograph of the stainless steel surface irradiated by burst of $n = 16$ sub-pulses delayed of $\Delta t = 1.5 \text{ ps}$. The double arrow indicates the polarization axis of the impinging sub-pulses, while the dotted arrow shows the beam scanning direction. (b) 2D-Fourier Transform of the SEM image. The k_x and k_y axis are normalized to the wave number $k_0 = 2\pi/\lambda = 6.1 \mu\text{m}^{-1}$, where $\lambda = 1.030 \mu\text{m}$ is the laser wavelength. [123]

The Δz values were estimated by AFM characterization of the samples surface AFM profiles of areas on the target of $4 \times 30 \mu\text{m}^2$ were acquired and imported in MATLAB as data matrix. An appositively developed algorithm allowed estimating the average depth of the ripples. Fig. 68 reports the case of LIPSS generated by bursts with $n = 16, \Delta t = 1.5 \text{ ps}$. The AFM profile was acquired with a mesh grid of pitch 10 nm. The processed 3D image related to $4 \times 6 \mu\text{m}^2$ area by ImageAnalysisP9 is reported in Fig. 68a. In Fig. 68b, red and blue points correspond to the maximum and minimum intensity values that the MATLAB algorithm detected along each raw of the data matrix, orthogonally to the ripples orientation. Then, the algorithm estimated the peak-to-valley heights as the difference between consecutive maximum and minimum values over the whole examined area. All the height values were plotted in a histogram (Fig. 68c) where the Gaussian fit confidently estimated the averaged ripples depth Δz and its standard deviation.

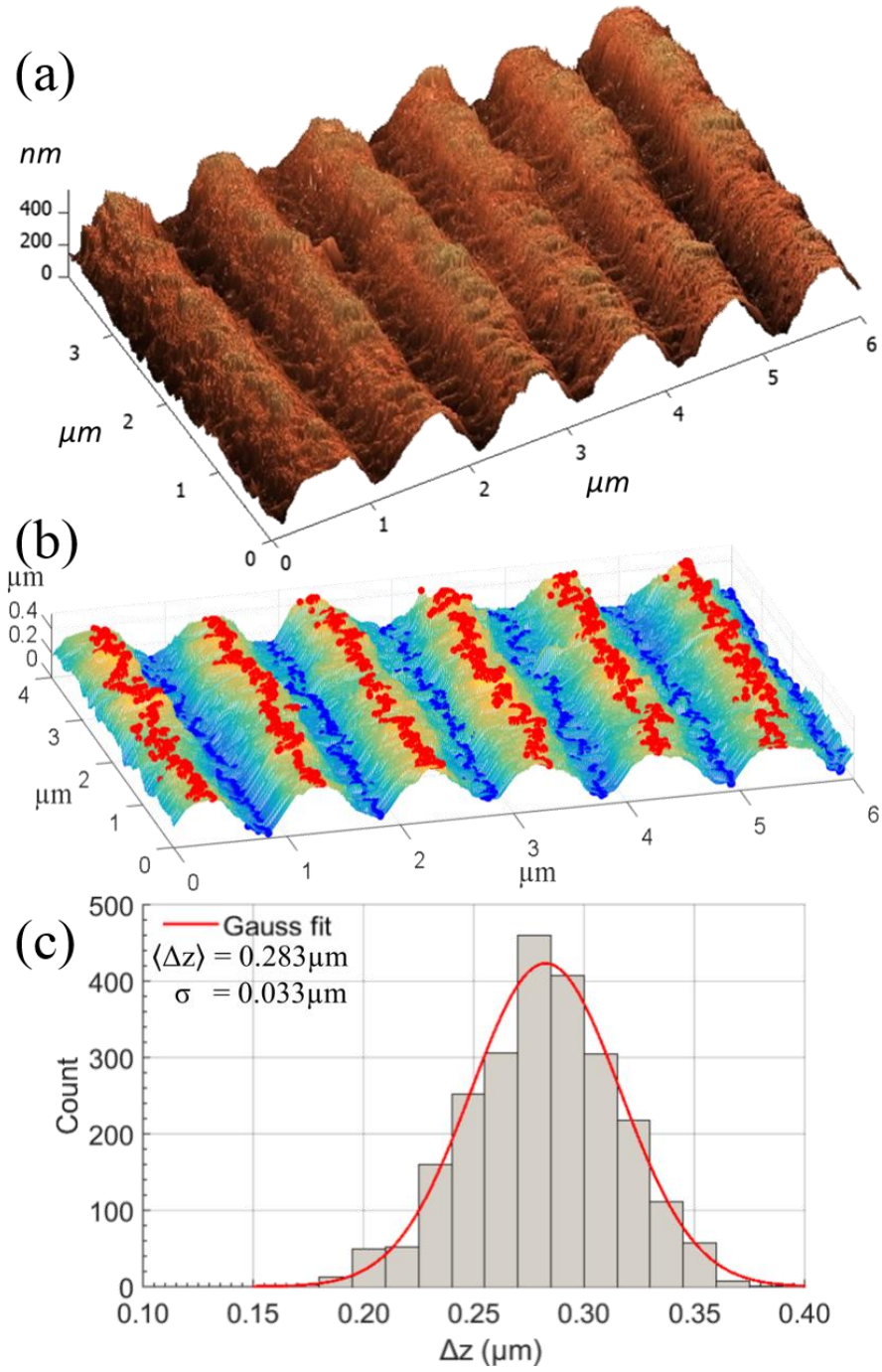


Fig. 68 (a) AFM image of a surface irradiated by bursts of 16 sub-pulses delayed of 1.5 ps. Using a simple algorithm, the peak and valley points of the ripples were located (b). The ripple depths Δz of adjacent peaks and valleys were plotted in a histogram (c) and fitted using a Gaussian function. [123]

After gathering all the data on the LSFL morphology produced under different burst irradiation conditions, these have been further analysed and compared with the case of NPM. Fig. 69 reports the spatial period Λ and depth Δz of the ripples generated by bursts of just 2 sub-pulses with variable delays Δt , ranging from 1.5 ps to 24 ps. The Λ values were evaluated as average of five SEM images. In the same plot, the period and depth of LIPSS generated in NPM are shown in correspondence of $\Delta t = 0$ ps (star points in Fig. 69). The LIPSS period of ~ 902 nm in NPM is similar to the value reported by analogous experiments conducted on stainless steel targets by other authors [87]. All LIPSS periods resulted close and slightly lower than the laser wavelength. In detail, for intra-burst delays shorter than 6 ps the ripples spatial period was close to the value found in NPM, while it increased up to 944 nm for longer delays, namely $\Delta t = 24$ ps. On the contrary, the depth of the ripples was always smaller than the NPM case (~ 265 nm), although for Δt shorter than 6 ps it stayed almost constant around 240 nm, very close to the value measured with unsplit pulses.

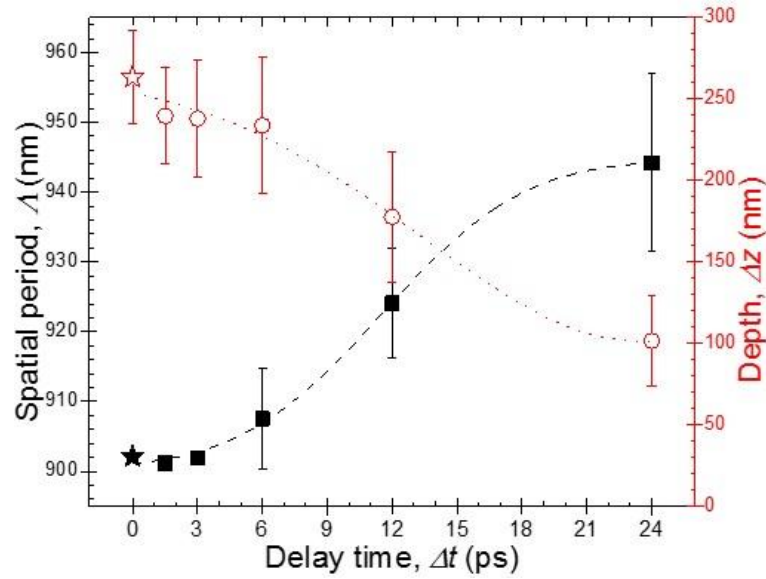


Fig. 69 Variation of the LSFL period (Λ , ■) and depth (Δz , ○) as a function of the time delay Δt between two sub-pulses. The points (★, ★) at $\Delta t = 0$ ps represent the normal pulse mode case. [123]

For longer time separations between the two sub-pulses the depth progressively decreases, being more than halved for $\Delta t = 24$ ps. This behavior can be ascribed to a shielding effect, described in Chapter 2.2. Indeed, different shielding regimes depending on the pulse-to-pulse delay have been reported during double-pulse laser irradiation [37,124]. Results shown in Fig. 69 are in fairly good agreement with those results confirming

that for very short delays (below 6 ps) the shielding effect is negligible and thus the ripples depth is substantially the same of NPM. While, for longer Δt , shallow ripples were found, thus indicating an increasing contribution of the shielding effect originated by the first sub-pulse.

Fig. 70 shows the results on the periodicity and depth of the LSFL as a function of the numbers of sub-pulses inside the burst at fixed intra-burst delay $\Delta t = 1.5$ ps. Concerning the LIPSS depth, following the previous interpretation based on shielding effect, even shallower structures were expected in case of bursts of longer duration obtained by increasing the number of sub-pulses in the bursts. Nevertheless, in Fig. 70, the ripples depth does not substantially change with the pulse splitting. A plausible physical explanation is the mutual compensation between two counteracting mechanisms, i.e. shielding and incubation. The shielding effect is expected to lead to a reduction of the ripples depth with n . On the other hand, the incubation effect, is responsible for a lowering of the ablation threshold fluence in case of irradiation with bursts of increasing number of sub-pulses [121,125]. Therefore, higher ablation and deeper structures are expected with increasing number of sub-pulses owing to incubation.

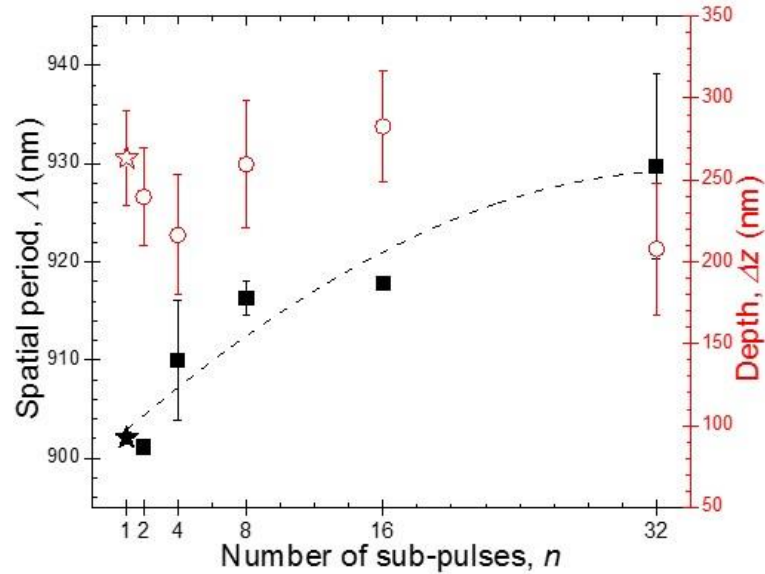


Fig. 70 Variation of the LSFL period (Λ , ■) and depth (Δz , ○) as a function of the number of sub-pulses n in the burst at fixed time delay ($\Delta t = 1.5$ ps). The points (★, ☆) at $n = 1$ represent the normal pulse mode case. [123]

Fig. 70 also shows a steady increase of the LSFL spatial period with the number of sub-pulses in the burst. In a previous study it has been proposed that in case of multi-pulse irradiation the structure generated by the first few laser pulses may influence the coupling of the laser radiation with the surface

plasmon polariton, leading to a decrease in the LSFL period [126]. If this is true, then this mechanism should be even more pronounced in case of sub-pulses with picoseconds delays, since this timeframe is shorter than the electron-phonon coupling time in metals.

7.2 2D-LIPSS

Surfaces texturing with bursts of ultra-short laser pulses with crossed and circular polarization, indicated respectively as XP and CP bursts, are presented in this section. Areas of $1 \times 1 \text{ mm}^2$ were textured in a single-step process (one laser scan) on stainless steel targets.

Fig. 71 reports two SEM images related to different surface structures obtained by irradiation of a scan line with overlap of $P^H = 98\%$ (50 bps^H , in term of burst per spot). The structures of Fig. 71a and Fig. 71c were induced by CP bursts of 2 sub-pulses ($F = 0.4 \text{ J/cm}^2$) and XP bursts of 8 sub-pulses ($F = 0.2 \text{ J/cm}^2$), respectively, with fixed intra-burst time delay of 1.5 ps .

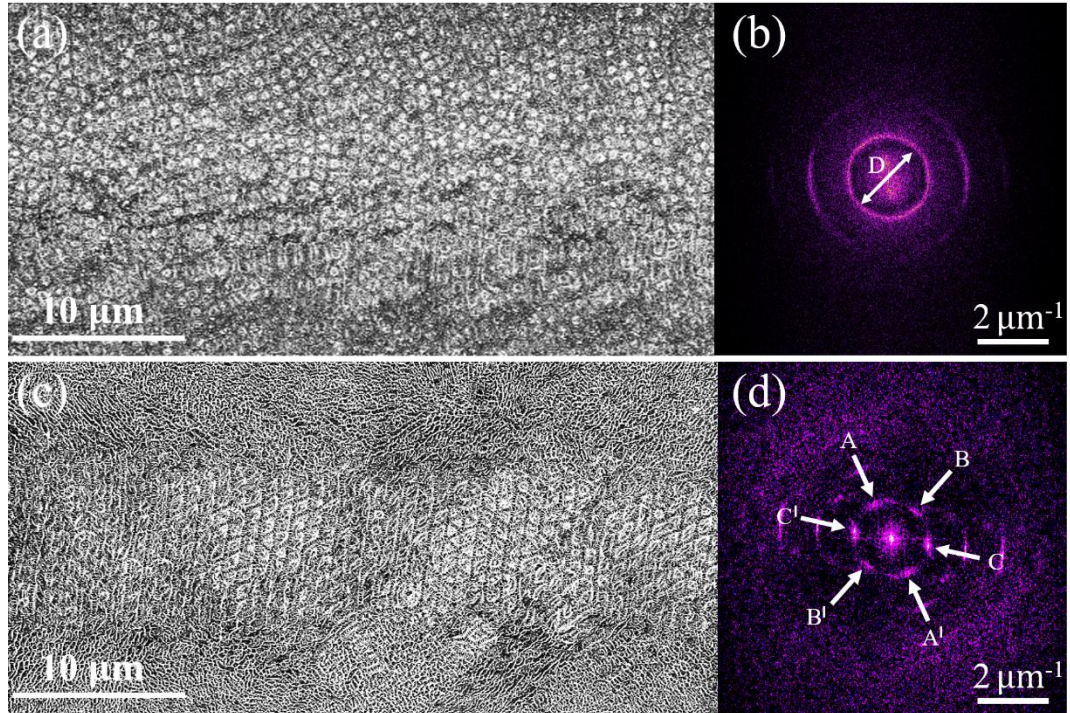


Fig. 71 (a, c) SEM images of the laser-induced surface structures by means of a laser scanning line with overlap $P^H = 98\%$ for (a) CP bursts of $n = 2$ sub-pulses, $\Delta t = 1.5 \text{ ps}$ ($F = 0.4 \text{ J/cm}^2$) and (c) XP bursts of $n = 8$ sub-pulses, $\Delta t = 1.5 \text{ ps}$ ($F = 0.2 \text{ J/cm}^2$). The 2D-FFT of the SEM images (a) and (c) are shown in images (b) and (d) respectively.

In detail, Fig. 71a shows pillar-like structures and its 2D-FFT, reported in Fig. 71b, highlights a ring which means that the pillars have a periodicity related to the ring radius ($D/2$) without any preferential direction. Therefore, such pillars are classified as quasi-periodic structures. On the other hand, from Fig. 71c, triangular-like shape structures can be observed in the center of the scan line where the laser fluence was higher due to the Gaussian beam profile. The 2D-FFT (Fig. 71d) of the SEM image reports six bright dots close to the zero spatial frequency, indicated by white arrows in Fig. 71d, which identify the three directions of periodicity along AA^I , BB^I and CC^I , oriented at 60° from each other. Hence, such triangular structures are classified as 2D-LIPSS, in particular LSFL because the average period of $\sim 900 \text{ nm}$ is close to the laser wavelength of 1030 nm .

In the following the experimental results on the laser-induced surface structures obtained with variable overlap and fluence are presented. Changes of the structures morphology with the number of sub-pulses and intra-burst time delay for both XP and CP bursts are analysed and discussed.

The influence of the laser spot spatial overlap along the scan line or between adjacent lines has been investigated and the results relating to CP bursts of double pulse with 1.5 ps time delay at constant laser fluence $F = 0.1 \text{ J/cm}^2$ are reported in Fig. 72. The spatial overlap, expressed in terms of burst per spot, is indicated as bps^H along the same scan line and bps^V between adjacent lines. The formation of the 2D-LIPSS was observed in a narrow window of scanning parameters, see Fig. 72a,e,h. A more careful analysis revealed that the triangular structures were generated for a given total number of burst per spot, $bps^T = bps^H \cdot bps^V = 240$, as reported in the label above each SEM image of Fig. 72. At lower overlaps, $bps^T \leq 120$ (Fig. 72d,g,i,l) LIPSS formation was not observed. Increasing the burst accumulation, periodic structures emerge and evolves progressively toward well-ordered triangular structures in hexagonal arrangement (Fig. 72a,e,h) with more defined ripples period. A further increase of bps^T led to gradually erase the triangular-LIPSS into disordered spikes (from Fig. 72b,f to Fig. 72c).

In Fig. 73 results obtained by varying the laser fluence from $F = 0.1 \text{ J/cm}^2$ to $F = 0.2 \text{ J/cm}^2$ and keeping the other parameters constant, are shown. It is evident that the triangular structures were formed at lower bps^T .

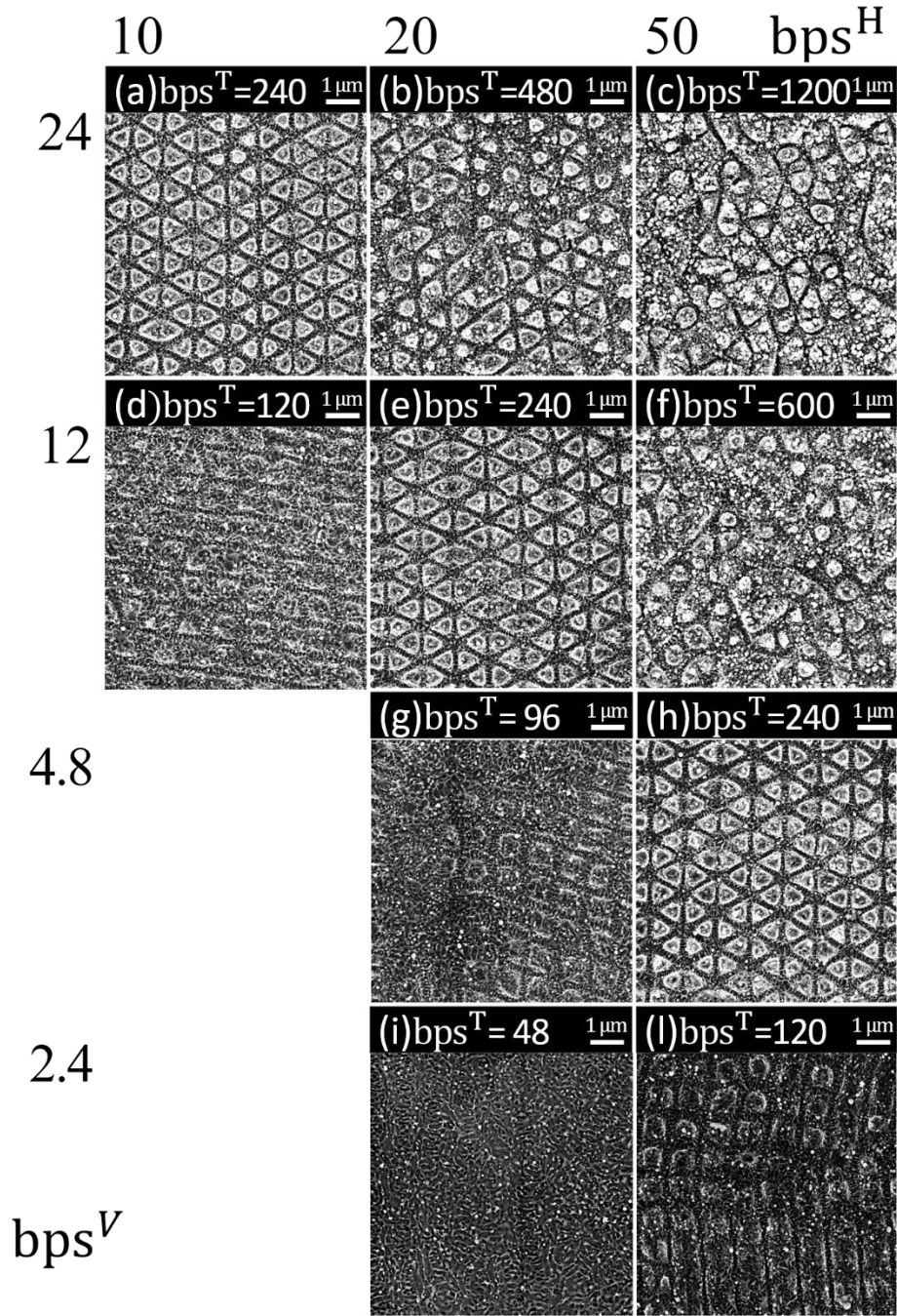


Fig. 72 SEM micrographs of stainless steel irradiated by circularly polarized (CP) burst of double pulse with time delay of 1.5 ps. The morphologies were generated keeping the laser parameters constant, i.e. laser fluence of $0.1 J/cm^2$, while varying the scanning strategy defined by burst per spot along the scan line, bps^H , or between subsequent lines, bps^V . The label above each graph reports the total burst per spot, bps^T .

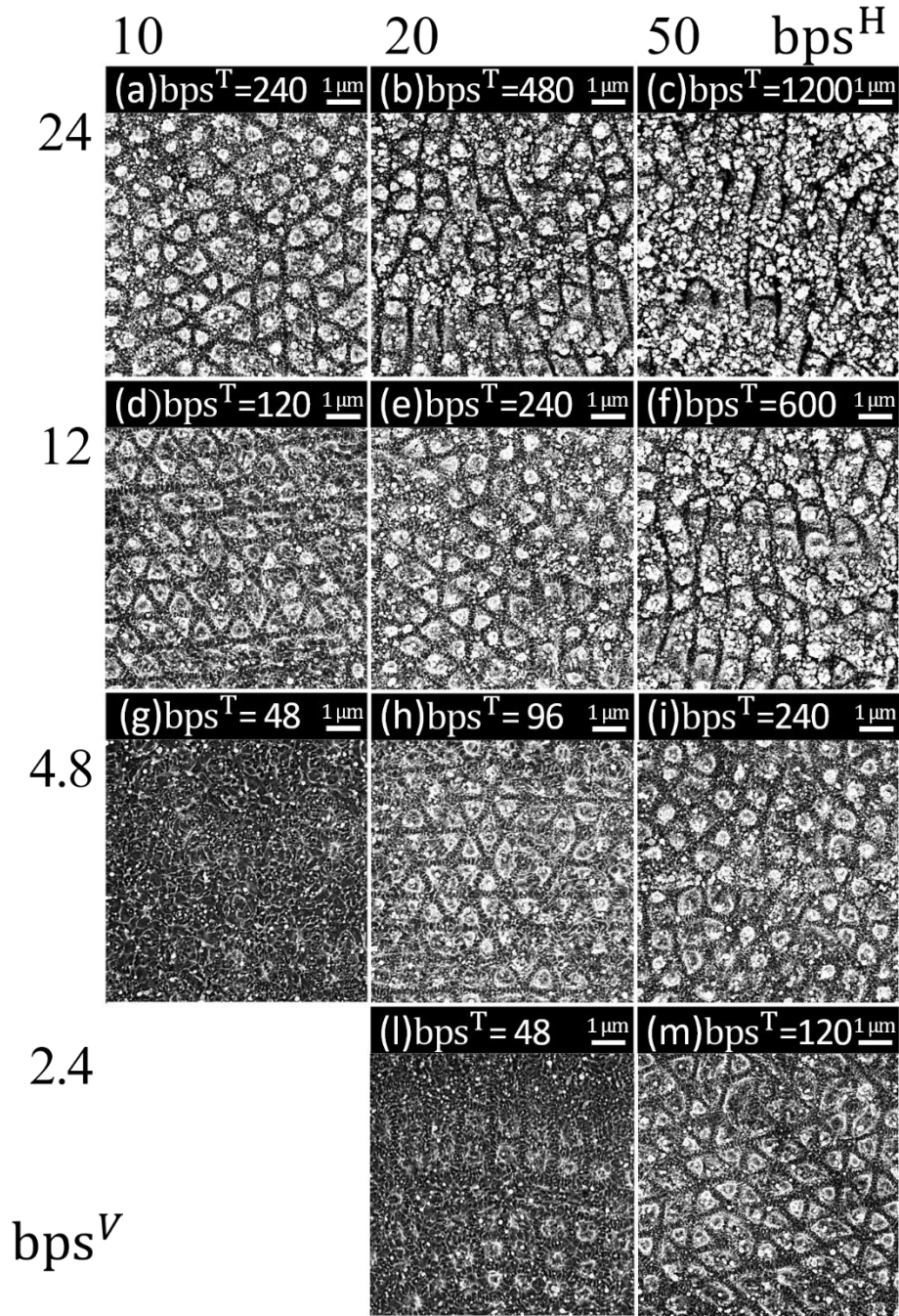


Fig. 73 SEM micrographs of stainless steel irradiated by circularly polarized (CP) burst of double pulse with time delay of 1.5 ps. The morphologies were generated keeping the laser parameters constant, i.e. laser fluence of $0.2 J/cm^2$, while varying the scanning strategy defined by burst per spot along the scan line, bps^H , or between subsequent lines, bps^V . The label above each graph reports the total burst per spot, bps^T .

It follows that the crucial parameter for the 2D-LIPSS formation is the accumulated burst fluence defined as $F^T = F \cdot bps^T$, rather than the burst per spot [99]. In fact, the triangular structures were observed for same accumulated fluence of $F^T = 24.0 \text{ J/cm}^2$ in Fig. 72a,e,h and in Fig. 73d,m. In the following, the surface patterns morphologies obtained by changing the number of sub-pulses and the intra-burst time delay are discussed, while keeping the overlap at $bps^T = 240$ ($bps^H = 20$ and $bps^V = 12$) and the laser fluence at two different values, i.e. $F_{low} = 0.1 \text{ J/cm}^2$ and $F_{high} = 0.2 \text{ J/cm}^2$, respectively, which in terms of accumulated fluence, correspond to $F_{low}^T = 24.0 \text{ J/cm}^2$ and $F_{high}^T = 48.0 \text{ J/cm}^2$.

In Fig. 74 the surface morphologies obtained with CP burst of double sub-pulse when the inter-pulse time delay Δt was changed from 1.5 ps to 24 ps are shown. In the same figure the case of NPM (referred as $\Delta t = 0 \text{ ps}$) is reported for comparison. Triangular structures formation can be observed in CP-NPM only for low fluence (Fig. 74a), as also found by [99]. In burst mode at low fluence and in the range $0 \text{ ps} < \Delta t \leq 3 \text{ ps}$ (Fig. 74b,c), the same triangular structures appear more definite and evenly distributed in perfect honeycomb arrangement. However, for longer delays $\Delta t > 3 \text{ ps}$ (Fig. 74d,e,f), the triangular LIPSS disappeared and only high spatial frequency LIPSS were generated with a period of few hundreds of nanometres and orientation following the steel metallographic grain structure [57,127]. For higher fluence, at $\Delta t = 1.5 \text{ ps}$ the triangular-LIPSSs were erased and replaced by spikes (Fig. 74h). On the other hand, the high fluence favoured the 2D structures formation in the range $3 \text{ ps} \leq \Delta t \leq 12 \text{ ps}$ (Fig. 74i,l,m). These results evidence the influence of the time delay in determining the final structure morphology as a function of the accumulated fluence. The latter carries out a crucial role in the formation of the triangular-LIPSS. In fact, the process window for 2D-LIPSS formation of $0 \text{ ps} < \Delta t \leq 3 \text{ ps}$ shifts toward longer time delays, $3 \text{ ps} \leq \Delta t \leq 12 \text{ ps}$, when increasing the accumulated fluence from 24 J/cm^2 to 48 J/cm^2 .

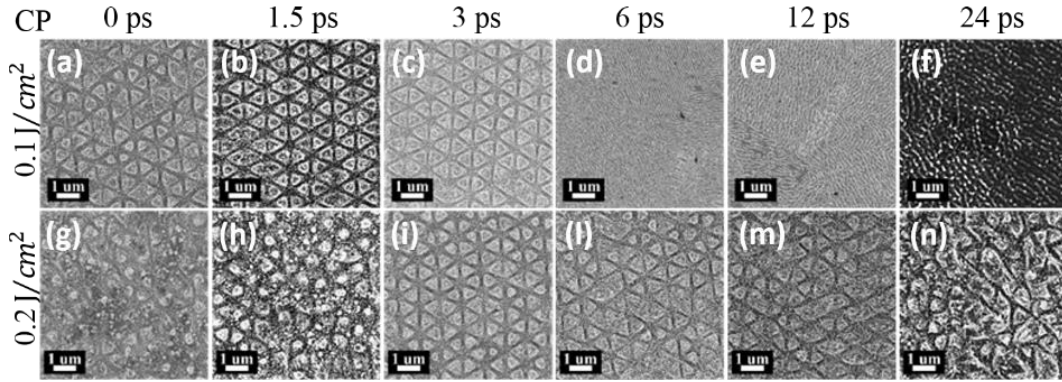


Fig. 74 SEM images of stainless steel surface processed with double circularly polarized (CP) sub-pulses for different inter-pulse time delays, from 1.5 ps (a,g) to 24 ps (n) and for two laser fluences, $F_{low} = 0.1 J/cm^2$ and $F_{high} = 0.2 J/cm^2$. The scanning strategy was fixed at $bps^T = 240$ with $bps^H = 20$ and $bps^V = 12$ for all the compared morphologies.

Fig. 75 shows results obtained when changing the polarization of the bursts of double sub-pulses from CP to XP. For $\Delta t = 0$ ps (i.e. NPM), ripples HSFL-like oriented perpendicular the laser wavelength were obtained for both values of laser fluence (Fig. 75a,g). In fact, in NPM there wasn't any splitting of the pristine pulses which remained in their linear polarization state LP which gave rise to HSFL by multiple irradiation ($pps^T = 240$), as discussed in chapter 3.2.4. When the burst generator was activated, barely triangular structures were visible in the range $1.5 ps \leq \Delta t \leq 6 ps$ at low fluence (Fig. 75b,c,d) and for $\Delta t = 6 ps$ at high fluence (Fig. 75l). At higher delays no-periodic structures were observed (Fig. 75e,m,n).

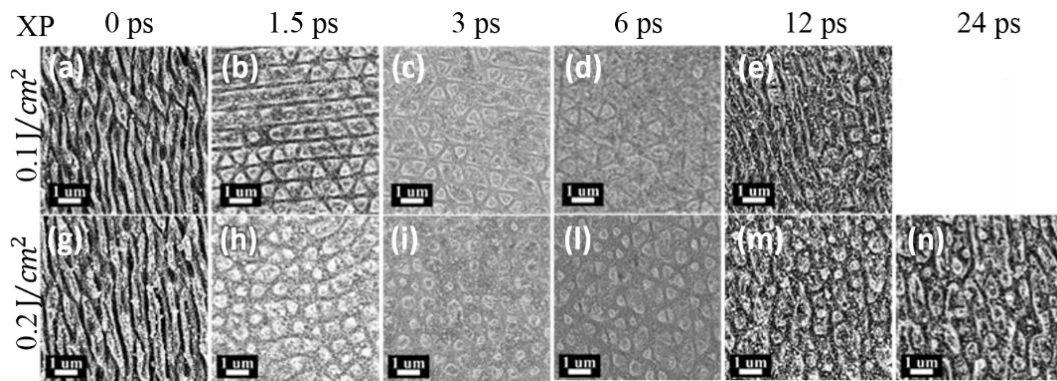


Fig. 75 SEM images of stainless steel surface irradiated by double cross polarized (XP) sub-pulses for different inter-pulse time delays, from 1.5 ps (a,g) to 24 ps (n) and for two laser fluences, $F_{low} = 0.1 J/cm^2$ and $F_{high} = 0.2 J/cm^2$. The scanning strategy was fixed at $bps^T = 240$ with $bps^H = 20$ and $bps^V = 12$ for all the compared morphologies.

These results highlight similarities and differences between the morphologies of the structures induced by CP and XP bursts. For both, CP and XP, the periodic structures at 1.5 ps were erased passing from low to high fluence. Delays of 12 ps between sub-pulses induced triangular-LIPSS only for CP (Fig. 74m) while disordered structures for XP (Fig. 75m). Anyway, the process windows for 2D-LIPSS formation are quite similar and limited at lower delay. The reason can be ascribed to shielding effect. Hence, when the intra-burst time delay increases, smaller fraction of the second sub-pulse energy effectively reaches the surface. This means that only a fraction of the effective accumulated fluence F^T hits the surface, which results not enough for triangular structures formation.

Fixing the intra-burst time delay at 1.5 ps and the experimental conditions of Fig. 74b and Fig. 75b where triangular LIPSS were found, experiments with bursts of increasing number of sub-pulses were carried out. Fig. 76 reports the results of the texturing with CP bursts, using the same process parameters of the double sub-pulses experiments, i.e. two accumulated fluence of $F_{low}^T = 24 \text{ J/cm}^2$ and $F_{high}^T = 48 \text{ J/cm}^2$ and 240 bps^T ($\text{bps}^H = 20$, $\text{bps}^V = 12$) as scanning strategy. Triangular structures were produced also for $n = 4$ sub-pulses (Fig. 76b) but not for $n \geq 8$ (Fig. 76c,d,e) at low fluence. In the latter case, HSFL were generated with orientation along the metallographic grains. Considering the total burst duration $\Delta T = \Delta t(n - 1)$, bursts with 4 sub-pulses with 1.5 ps delay have a total duration $\Delta T = 4.5 \text{ ps}$ while burst with 8 sub-pulses have $\Delta T = 10.5 \text{ ps}$. Therefore, the results of Fig. 76 are in line with those obtained with bursts of double sub-pulse discussed above. Moreover, in analogy with Fig. 74, for $n \leq 4$ the high fluence erased the 2D-LIPSS replacing them with pillar-like structures (Fig. 76f,g) while for $n = 8$, same triangular structures emerged, mixed with pillars (Fig. 76h). Finally, 16 and 32 sub-pulses (Fig. 76i,l) generated non-periodic structures.

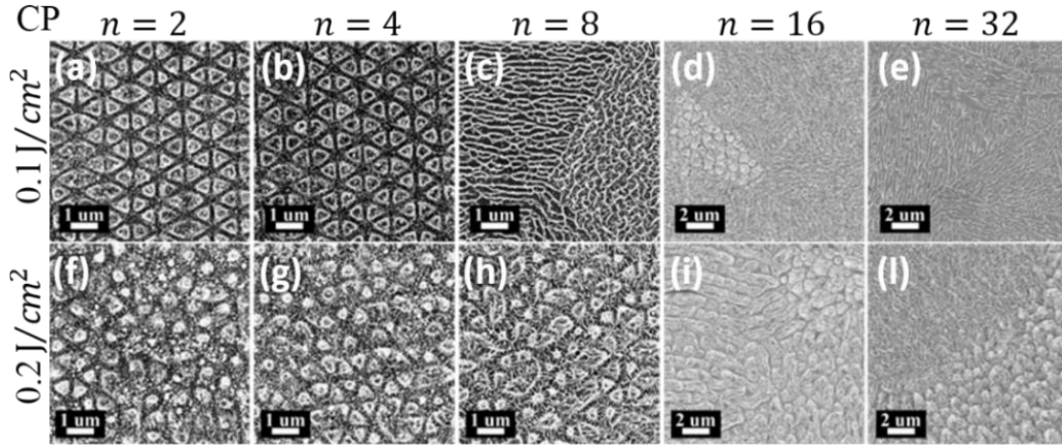


Fig. 76 SEM images of stainless steel surface irradiated by circularly polarized (CP) bursts with sub-pulses variable from 2 (a,f) up to 32 (e,l) at fixed intra-burst delay of 1.5 ps for two laser fluence, $F_{low} = 0.1 \text{ J/cm}^2$ and $F_{high} = 0.2 \text{ J/cm}^2$. The scanning strategy was fixed at $bps^T = 240$ with $bps^H = 20$ and $bps^V = 12$ for all the compared morphologies.

When XP bursts were used rather than CP ones, no substantial differences were observed in the microstructure morphology, as can be seen by comparing Fig. 76 with Fig. 77. The 2D-LIPSS with triangular shape were always found in a very narrow window of process parameters, such as low accumulated fluence for low pulse splitting ($n \leq 4$), while at high fluence values the triangular-LIPSSs were erased.

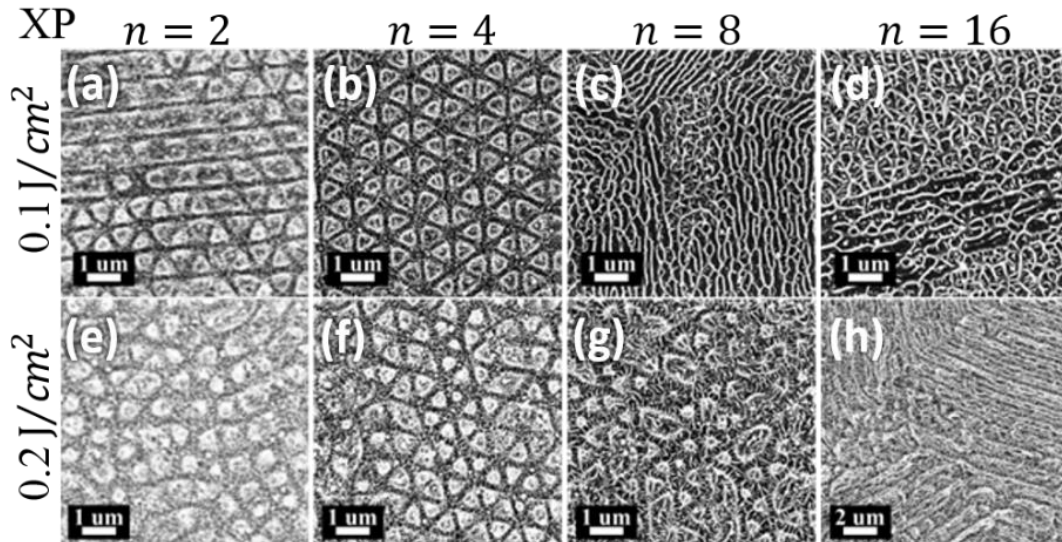


Fig. 77 SEM images of stainless steel surface irradiated by cross polarized (XP) bursts with sub-pulses variable from 2 (a,e) up to 16 (d,h) at fixed intra-burst delay of 1.5 ps for two laser fluence, $F_{low} = 0.1 \text{ J/cm}^2$ and $F_{high} = 0.2 \text{ J/cm}^2$. The scanning strategy was fixed at $bps^T = 240$ with $bps^H = 20$ and $bps^V = 12$ for all the compared morphologies.

Finally, by finely adjusting all the process parameters, i.e. laser fluence and scanning strategy in terms of total number of bursts per spot, highly regular and uniform triangular 2D-LIPSS were consistently produced with XP and CP bursts with $n \leq 8$ and $\Delta t \leq 16$ ps. The FFT analysis of the SEM images allowed precisely evaluating the periodicity and directionality of the obtained structures. In Fig. 78 a representative analysis of the SEM image (see Fig. 77b) of the triangular structures generated by XP burst with 4 sub-pulses delayed 1.5 ps is shown. The related 2D-Fourier transform is depicted in Fig. 78b. Here, the three directions of periodicity are well highlighted by dashed lines and present an angular shift of around 60° . For each of the three preferential directions, the spatial period Λ is evaluated from the 1D-FFT profile, plotted in Fig. 78c. The average period among the three direction is 934 ± 13 nm. In Fig. 78c, the frequency peaks intensity is about two orders of magnitude greater than background noise. Such intensity are reached only with periodic structures at higher uniformity (few defects).

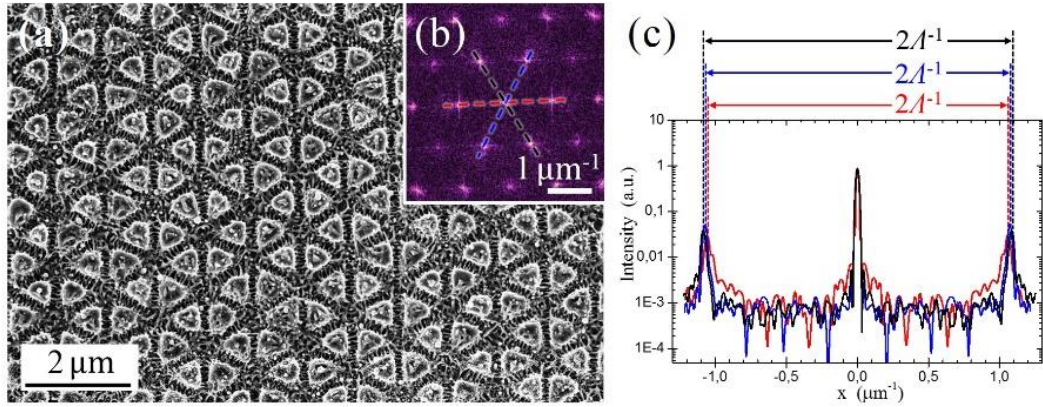


Fig. 78 (a) SEM image of high regularity triangular-like LIPSS obtained optimizing the texturing process for CP $n = 4$ sub-pulses ($\Delta t = 1.5$ ps). (b) 2D-FFT of the surface structures obtained in (a). (c) Period measurement from 1D-FFT profiles of the dotted cross-section lines of the 2D-FFT image in (b).

In addition, the triangular structures were analysed by AFM. Fig. 79a reports the AFM profile of triangular structures with definite and uniform morphology induced by bursts of double sub-pulse with time delay of 3 ps for an accumulated fluence of $F^T = 24.0$ J/cm² and a scanning strategy of $bps^T = 240$ ($bps^H = 10$, $bps^V = 24$). In particular, the cross-section profile along the red segment is shown in Fig. 79b. The structures reveal two different types of depth, one in correspondence of the centre of the hexagons Δz_1 and the other along the adjacent triangle sides Δz_2 . The average depths from 10 random profiles were $\Delta z_1 = 313 \pm 46$ nm and $\Delta z_2 = 191 \pm$

35 nm, respectively. Similar profiles and results were found by Liu et al. [102] as shown in Fig. 38.

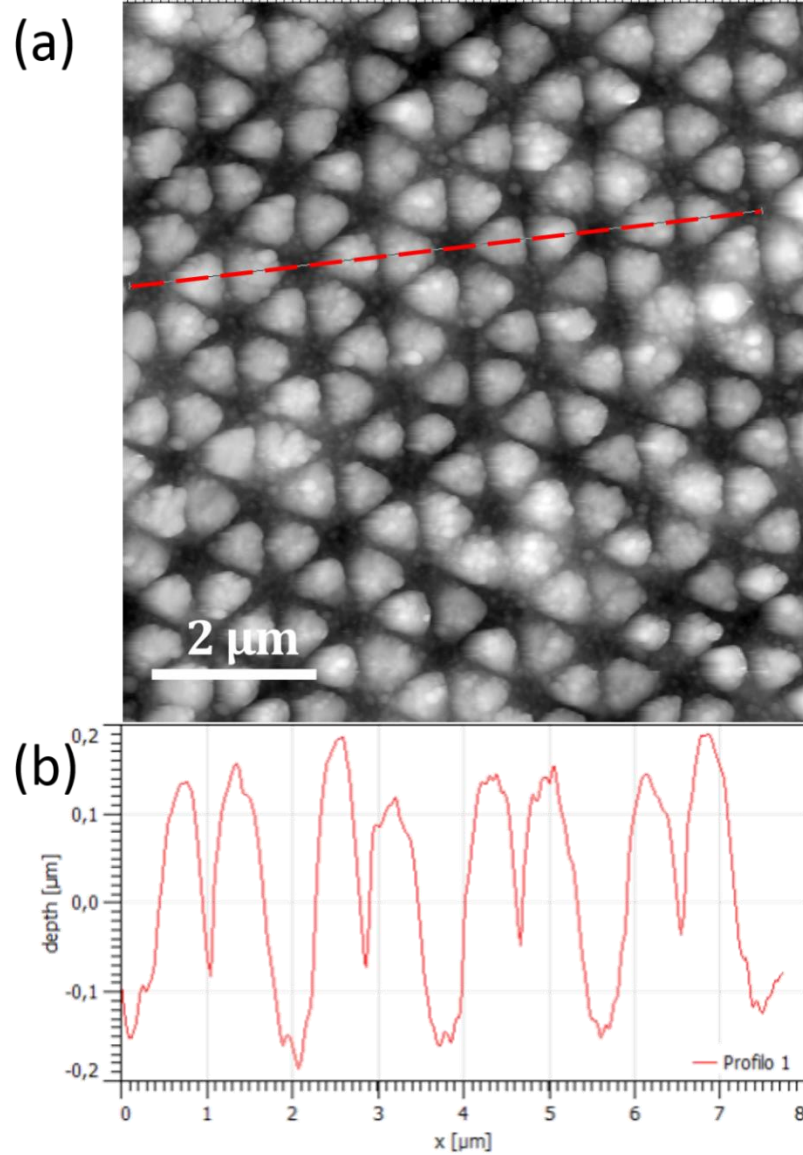


Fig. 79 (a) AFM image of a stainless steel surface irradiated by XP bursts of double sub-pulse with time delay of 3 ps and accumulated fluence of $F^T = 24.0 \text{ J/cm}^2$. The scanning strategy was fixed at $bps^T = 240$ with $bps^H = 10$ and $bps^V = 24$. (b) Profile of the structures obtained by AFM analysis carried out along the red segment in (a).

In conclusion, LIPSSs were generated with both XP and CP bursts. Structures with different morphologies were found depending on the process parameters and the characteristics of the bursts used. Crucial parameters were the overlap between consecutive bursts irradiation, laser fluence, number of sub-pulses in the burst and their time delay.

7.3 Wettability

The nano and microstructures induced by laser texturing have been shown to functionalise the surfaces modifying their wettability [128,129], cells/bacteria adhesion [130,131], frictional [132] and optical properties [55,133]. In this section the wettability properties of selected surface texture patterns with quite different morphologies have been assessed. The eight investigated structures are summarized in Fig. 80 and for simplicity, each of them is labelled with a short name shown in *italic*. Three samples with linear-type LSFL (1D-LIPSS) have been selected, i.e. the morphologies produced by LP bursts with 16 and 32 sub-pulses with 1.5 ps delay (here called *LSFL-n16* and *LSFL-n32* sample) and LP pristine pulses (*LSFL-NPM*), widely treated in Chapter 7.1. *LSFL-NPM* and *LSFL-n32* were chosen because they were characterized by the maximum and minimum ripples profile aspect ratio, defined as the ratio between the spatial period and the depth of the ripples, from Fig. 70. Beyond these, the *LSFL-n16* morphology was included in this study since it exhibited the maximum depth of the structures. Such morphological parameter is known by literature [120] to be correlated to the water contact angles (WCA). The wettability of the triangular structures was investigated through just one representative morphology (labelled with *Triangular 2D-LIPSS* and shown in Fig. 77b) with well-defined triangles over a large area, induced by XP burst of 4 sub-pulses with 1.5 ps delay, and accumulated fluence of 24 J/cm^2 . Two additional surfaces characterized by high spatial frequency LIPSS with different morphology were also selected. In detail, the HSFL generated in NPM (*HSFL-NPM*, see Fig. 75a) with high number of pulses per spot and those induced by XP burst (pointed as *HSFL-BM*, see Fig. 77d) of 16 sub-pulses and intra-burst delay of 1.5 ps. In addition, one sample with quasi-periodic pillar-like structure (named as *pillars*) and another with non-periodic ripples on micrometer sizes (called *micro-ripples*) were included in this study. In particular, the *pillar* and *micro-ripples* structures were induced by XP burst with 2 and 16 sub-pulses, respectively, and 1.5 ps in time delay at the higher value of laser fluence of 0.4 J/cm^2 . A stainless steel sample untreated flat sample (named *untreated*) was analysed as reference. Fig. 80 reports the SEM images of each of the investigated surface summarized in Table 7-1.

Table 7-1 Description of the chosen surfaces for wettability analysis, in term of their morphology and employed process parameters.

Sample label	Structures	Irradiation mode + features	Irradiation parameters		Fig.
			Laser fluence	pps ^T /bps ^T	
<i>LSFL – NPM</i>	1D-LSFL	LP-NPM	0.85 J/cm ²	11.5	Fig. 80a
<i>LSFL - n16</i>	1D-LSFL	LP-BM, n=16, $\Delta t=1.5$ ps	0.85 J/cm ²	11.5	Fig. 80b
<i>LSFL - n32</i>	1D-LSFL	LP-BM, n=32, $\Delta t=1.5$ ps	0.85 J/cm ²	11.5	Fig. 80c
<i>HSFL – NPM</i>	HSFL	LP-NPM	0.1 J/cm ²	240	Fig. 80d
<i>HSFL – BM</i>	HSFL	XP-BM, n=16, $\Delta t=1.5$ ps	0.1 J/cm ²	240	Fig. 80e
<i>Triangular 2D-LIPSS</i>	2D-LSFL	XP-BM, n=4, $\Delta t=1.5$ ps	0.1 J/cm ²	240	Fig. 80f
<i>Pillars</i>	quasi-periodic	XP-BM, n=2, $\Delta t=1.5$ ps	0.4 J/cm ²	240	Fig. 80g
<i>Micro-ripples</i>	non-periodic	XP-BM, n=16, $\Delta t=1.5$ ps	0.4 J/cm ²	240	Fig. 80h
<i>Untreated</i>	None	/	/	/	Fig. 80i

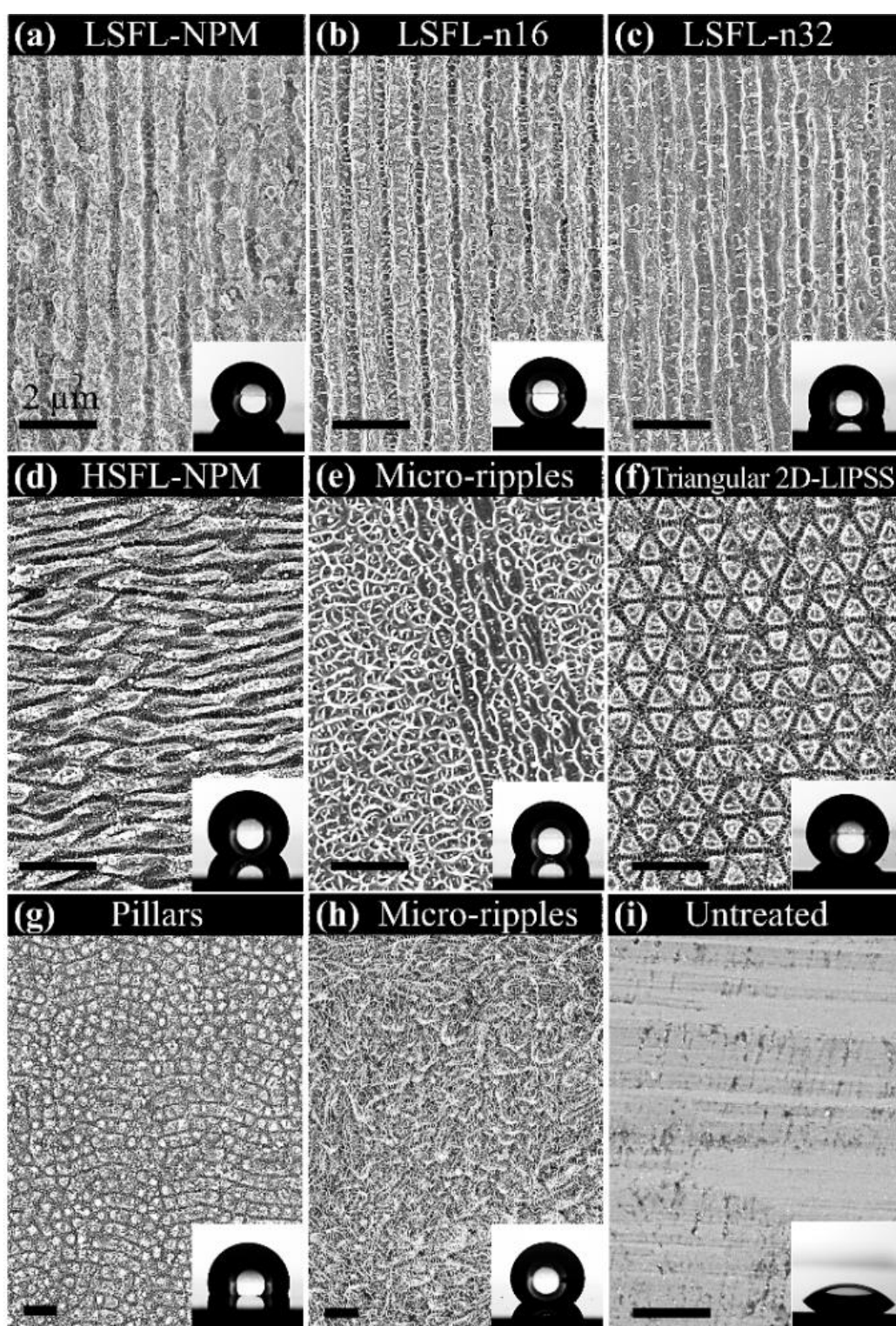


Fig. 80 SEM images of the different surface morphologies laser-induced described in Table 7-1. The black bars represent a length of 2 μm . The insert of each image reports the picture of the water drop (5 μl) 55 days after the laser process.

7.3.1 WCA: static and dynamic measurements

The wettability measurements were carried out on large texturized areas of 200 mm^2 both in static and in dynamic with droplets of $5\text{ }\mu\text{l}$ of distillate water. No chemical products or ultrasonic bath were used to clean the laser textured samples. After laser irradiation the samples have been blown by a dry air flow just to roughly remove any ablation debris. Storage of the samples took place in ambient air at room temperature.

The static WCA for each surface of Table 7-1 was averaged over a minimum of 3 droplets placed in different locations on the sample. Table 7-2 shows the obtained results by measuring the WCA 55 days after the laser processing, for stabilized surface, i.e. without significant change in WCA the following days, as verified by aging analysis (Fig. 81). In the inset of each SEM image of the surfaces shown in Fig. 80, a picture acquired by the camera of the water droplet placed on it is reported.

Table 7-2 Static water contact angle with drops of $5\text{ }\mu\text{l}$ for the surfaces of Table 7-1.

Sample	WCA
<i>LSFL - NPM</i>	$150.2^\circ \pm 1.6^\circ$
<i>LSFL - n16</i>	$160.1^\circ \pm 1.5^\circ$
<i>LSFL - n32</i>	$138.7^\circ \pm 1.3^\circ$
<i>HSFL - NPM</i>	$160.6^\circ \pm 1.2^\circ$
<i>HSFL - BM</i>	$145^\circ \pm 2^\circ$
<i>Triangular 2D-LIPSS</i>	$155.6^\circ \pm 1.3^\circ$
<i>Pillars</i>	$123.7^\circ \pm 1.8^\circ$
<i>Micro-ripples</i>	$157.1^\circ \pm 1.4^\circ$
<i>Untreated</i>	$55^\circ \pm 2^\circ$

Starting with a static contact angle of 55° prior to laser texturing (see results of untreated sample), the largest part of the fabricated surfaces achieved the super-hydrophobic behaviour ($WCA > 150^\circ$) except for *LSFL-n32*, *HSFL-BM* and *Pillars* which became only hydrophobic. The three LSFL structures showed greater WCA for deeper ripples [134]. WCA of 155.6° was achieved for triangular-LIPSS. In addition to static measurements, the dynamic wettability was evaluated, i.e. the so-called hysteresis (H) which is difference between the advancing (θ_{adv}) and the receding (θ_{rec}) CA. The experimental results are reported in Table 7-3.

Table 7-3 Hysteresis CA evaluated with drops of 5 μl for the surfaces of Table 7-1.

Sample	θ_{adv}	θ_{rec}	H
<i>LSFL - NPM</i>	$158^\circ \pm 2^\circ$	$14.6^\circ \pm 1.1^\circ$	$144^\circ \pm 3^\circ$
<i>LSFL - n16</i>	$165^\circ \pm 2^\circ$	$27^\circ \pm 7^\circ$	$138^\circ \pm 9^\circ$
<i>LSFL - n32</i>	$150.5^\circ \pm 1.2^\circ$	$20^\circ \pm 4^\circ$	$131^\circ \pm 5^\circ$
<i>HSFL - NPM</i>	$161.4^\circ \pm 1.3^\circ$	$15^\circ \pm 2^\circ$	$146^\circ \pm 3^\circ$
<i>HSFL - BM</i>	$150.6^\circ \pm 1.2^\circ$	$14.1^\circ \pm 1.2^\circ$	$137^\circ \pm 2^\circ$
<i>Triangular 2D-LIPSS</i>	$156.8^\circ \pm 1.5^\circ$	$29^\circ \pm 6^\circ$	$128^\circ \pm 7^\circ$
<i>Pillars</i>	$132^\circ \pm 3^\circ$	$25.2^\circ \pm 1.1^\circ$	$107^\circ \pm 4^\circ$
<i>Micro-ripples</i>	$158^\circ \pm 2^\circ$	$14^\circ \pm 3^\circ$	$144^\circ \pm 5^\circ$
<i>Untreated</i>	$66.6^\circ \pm 1.7^\circ$	$11^\circ \pm 3^\circ$	$55^\circ \pm 5^\circ$

All the morphologies highlighted a high hysteresis ($H > 100^\circ$), which excludes a super-hydrophobic water-repellent behaviour despite the high static WCA. Therefore, a Wenzel state wet contact, has been achieved due to the concurring effects of surface morphology and chemistry. Indeed, after placing the droplet and tilting the sample, it did not roll down or slide even when the tilting angle reached 90° (vertical plane) meaning that the adhesion force overcame the gravity force. In other words, the investigated surfaces were super-hydrophobic adhesive, with a sticky behaviour.

7.3.2 Aging: from hydrophilicity to super-hydrophobicity

Fig. 81 shows the evolution of the static water contact angle with to the aging time for two different samples characterized by 1D and 2D laser-induced periodic surface structures, i.e. *LSFL-n16* and *Triangular 2D-LIPSS*, respectively. Directly after the laser processing, both the surfaces became more hydrophilic with respect to the pristine untreated state with a contact angle of $\sim 3^\circ$ and $\sim 26^\circ$ for 1D and 2D-LIPSS, respectively. Aging, the LIPSS structures gradually reached values above 150° , i.e. super-hydrophobic behaviour. Beyond a period of eight weeks, this evolution stopped and the WCA stabilised without further significant change in the following days. In detail, WCA of $\sim 160^\circ$ and $\sim 155^\circ$ for linear and triangular LIPSS, respectively, were achieved. Fig. 82 reports the pictures of four water drops of 5 μl on the two aged surfaces illuminated by the camera flash.

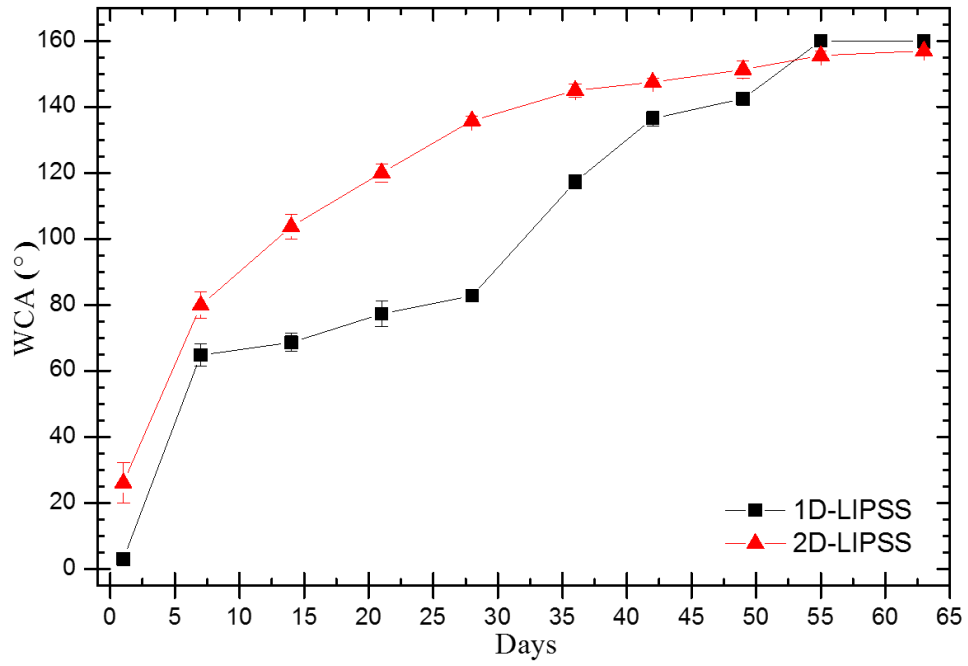


Fig. 81 Evolution of the static WCA over time for two different morphological structures on stainless steel surface, 1D-LIPSS and 2D-LIPSS. That one 1D corresponds to *LSFL-n16* while the other to *Triangular 2D-LIPSS*. The samples were stored in the ambient condition.

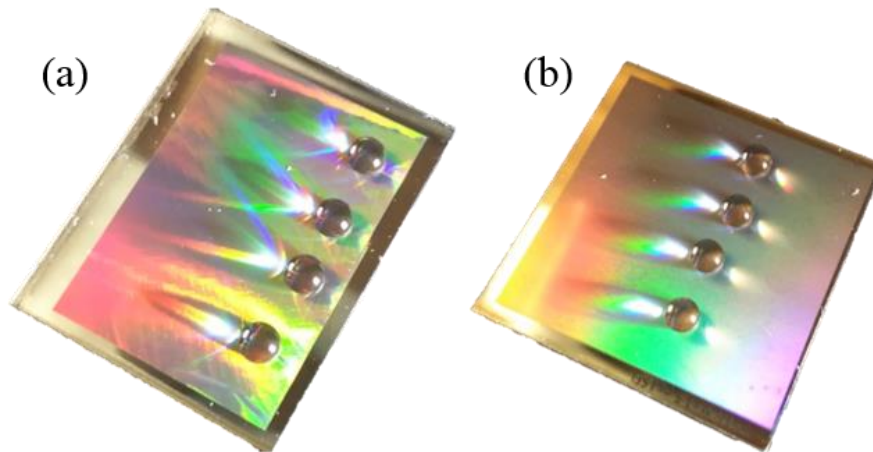


Fig. 82 Pictures of a four drops of distillate water on the texturized surfaces with triangular 2D-LIPSS structures (a) and with 1D-LIPSS (b) irradiated by XP bursts ($n=4$, $\Delta t=1.5$ ps) and LP bursts ($n=16$, $\Delta t=1.5$ ps), respectively.

Such a change of the wettability properties, from hydrophilic to hydrophobic, of laser textured surfaces with the aging is a well-known behaviour in literature [135,136]. It has been observed on various metallic substrates. It has been further demonstrated that the storage conditions play also an important role in the aging process [137]. Therefore, the transition from hydrophilicity to hydrophobicity or super-hydrophobicity cannot be explained based only on the surface topography, since it does not change with time after the laser treatment. Modification of the surface chemistry seems more likely to explain such a change. Kietzig et al. [138,139] ascribed the increase of the WCA to an accumulation and/or adsorption of non-polar carbon during the days following the laser treatment. Their assumption was supported by XPS analyses.

Therefore, XPS analyses have been carried out on the two samples of fig. 43 aiming to assess the surface chemistry. In particular, the chemical percentage of carbon, oxygen, iron, chromium and nickel (always less than 1%) was evaluated from the XPS spectra. In Fig. 83, the chemical compositions of each surface acquired both one day and 55 days after the laser treatment is reported. In addition, XPS analysis of untreated samples were carried out as a reference. Before the treatment, the surfaces exhibit a carbon content of ~75%, while immediately after the femtosecond laser irradiation the carbon decreases to an amount less than 22% for both linear and triangular LIPSS. Such decrease in carbon content is ascribed to the removal via laser ablation of surface contaminants. Moreover, the laser process induces iron oxide formation that justify the increase of the oxygen and iron content one day after the treatment. In detail, the oxygen content passes from 22.5% for untreated sample to 47.8% and 46.5% for linear and triangular LIPSS, respectively, while iron content grows from 2.1% up to 21.8% and 27.2%. The further variations in the surface chemistry during the samples aging are due to the exposure to the air. In particular the adsorption of hydrocarbon molecules [140] and/or chemical interaction with the ambient CO₂ [138,141] justifies the increase of the carbon content with time. After 55 days, carbon content increased up to 55.7% and 50.8% for the 1D- and 2D-LIPSS, respectively. Adsorption of hydrocarbon molecules on the sample surface which cover the metal oxide, would explain the strong reduction of oxygen and iron percentages registered after 55 days. Indeed, oxygen content in 1D-LIPSS sample decreases from 47.8% to 31.9%, while iron decreases from 21.8% to 8.5%. Similarly, for 2D-LIPSS sample, oxygen content decreases from 46.4% to 34.6%, while iron from 27.2% to 9.8% after 55 days.

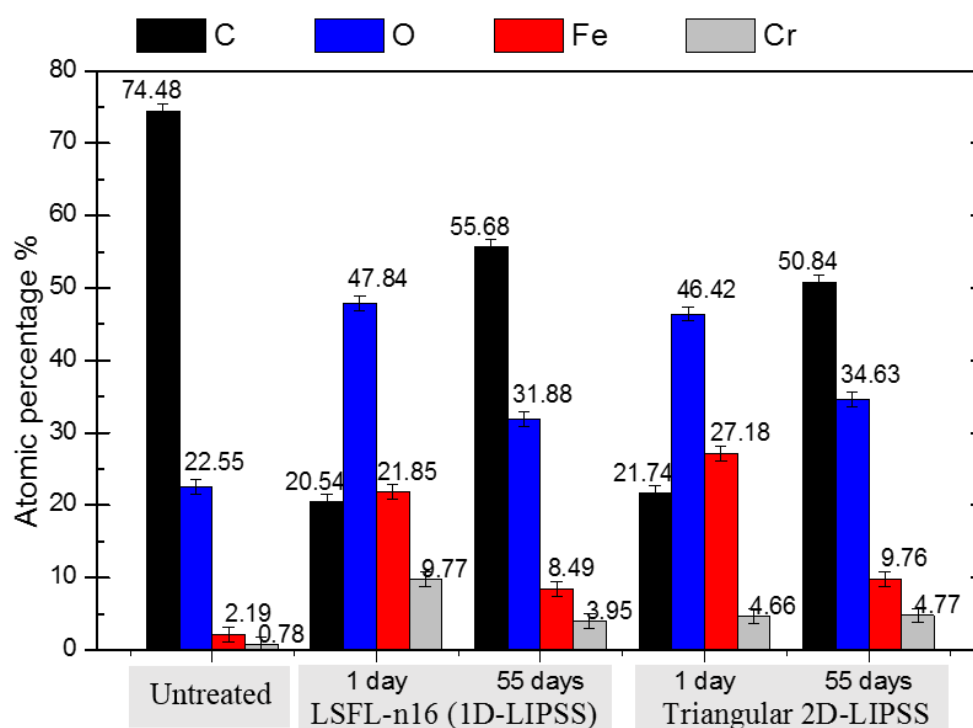


Fig. 83 Hystogram of the atomic percentages measured by XPS analysis on 3 samples of stainless steel: untreated surface, LSFL-n16 (1D-LIPSS) and triangular 2D-LIPSS. The last two were analysed 1 day and 55 days after the laser irradiation. The samples were stored in air.

Conclusions

In this thesis, investigations on laser ablation and surface texturing with bursts of ultrashort pulses were presented.

Recently, bursts mode processing has attracted growing interest from the scientific community as a possible way to overcome the thermal issues that degrade the quality and precision of laser-based micro-processes when using ultrafast laser sources with relatively high repetition rates and average powers. The burst mode was proposed as a tool to better tailor and manage the energy transfer from the laser source to the target material avoiding or reducing the amount of energy which is not used for material removal process but is rather transformed into heat that induces thermal-stresses or damages to the material. With bursts, the energy of the laser pulses is split into several sub-pulses which are time delayed each other of time distances that are typically much shorter than the laser repetition rate.

In this work, the bursts were produced by a burst generator plugged in the experimental setup, which allowed the production of different burst configurations by varying the number of sub-pulses between 2 and 32 and their time delay between 1.5 ps and 46.5 ps. These time delays are of the same order of the electron-phonon coupling time in metals. Therefore, during the laser process, the material excited by the first sub-pulse is still in a non-equilibrium state when the following sub-pulses arrive. This leads to interesting and new ablation dynamics that have been presently investigated. The first part of this work was devoted to the study of the laser ablation using bursts of 750 fs (FWHM) ultrashort pulses at a wavelength of 1030 nm. In detail, the influence of the burst features, such as the number of sub-pulses and the intra-burst time delays, on the laser ablation threshold fluence of stainless steel target has been studied. The number n of sub-pulses in the bursts was varied from 2 up to 32 while the intra-burst time delay was 1.5 ps or 3 ps. Varying the number of applied bursts in the range from 50 to 1600 at fixed repetition rate of 100 kHz, a variation of the ablation threshold was found due to the incubation mechanism. It was found that the threshold fluence decreases when increasing the total number of impinging sub-pulses N_{tot} . For comparison, analogous experiments were carried out with sequences of 50-1600 single pulses, named as normal pulses mode (NPM), in the same experimental conditions. Differently from the case of NPM, in case of BM processing, different values of the threshold fluence $F_{th}(N_{tot})$ were found for fixed $N_{tot} = N \cdot n$, the combination of number of bursts N and number of sub-pulses n per burst. None of the existing incubation models developed for NPM could explain the BM results. Therefore, the

existing NPM model was extended also to BM by introducing an incubation factor S_n which takes into account the burst features, i.e. the number of sub-pulses in the burst. Such a model was found to fit the experimental data for all the investigated BM, returning the incubation factors S_n that were found always lower than the corresponding factor S obtained in NPM. Moreover, such S_n decreased with the number of sub-pulses n in the burst, independently of the intra-burst time delay, thus indicating an enhancement of incubation with the pulse splitting. This behaviour has been ascribed to different concurring mechanisms, like e.g. damage accumulation or change in surface chemistry and topography, contributing to a more efficient deposition of the laser energy into the material when bursts with a high number of sub-pulses are applied. Next to experimental data, numerical simulations based on the solution of the Two-Temperature Model in case of NPM and BM have been performed. The temporal and spatial evolution of the electron and lattice temperature during ultrafast laser irradiation in both operating modes were calculated. The simulations showed that the amount of absorbed laser energy needed for the lattice to reach the melting temperature decreased when n increased. In addition, for longer time delays within the burst, more energy is required to reach the melting threshold.

Such results explain to some extent the experimental findings, confirming that the energy transfer from the laser beam to the material is affected by the burst characteristics.

Laser milling experiments were carried out on stainless steel to evaluate the specific removal rate in case of BM and NPM with ultrashort pulses of 238 fs at 1030 nm wavelength. The experiments in BM were performed both with burst of two sub-pulses with time delay varied between 1.5 ps and 24 ps and also with bursts from 2 to 32 delayed sub-pulses of 1.5 ps. The BM specific removal rate was always lower than the maximum specific removal rate obtained in NPM at the optimum laser fluence. Indeed, the laser-matter interaction of first sub-pulses in the burst probably induced shielding or scattering of subsequent ones. However, for laser fluence lower than the optimal value, bursts of two delayed sub-pulses of 1.5 ps led a higher removal rate than NPM in a narrow window of process conditions.

The second part of this research work has been focused on the experimental investigation of the LIPSS formation on steel samples induced by different bursts configuration of ultrashort 238 fs pulses. Bursts differed for number of sub-pulses, intra-burst time delay and polarization. Indeed, by linearly polarized (LP) bursts, i.e. sub-pulses with parallel polarization among them, structures with only one periodic direction, so-called one-dimensional LIPSS (1D-LIPSS) were obtained. The generation of low spatial frequency LIPSS (LSFL) on steel samples irradiated by LP bursts with same fluence and

variable number of sub-pulses, from 2 to 32, and intra-burst delays, from 1.5 ps to 24 ps, has been systematically investigated. It was found that the LSFL morphology, i.e. ripples period and depth, changed with the burst features. For bursts consisting of two sub-pulses, the spatial period increased with the intra-burst delay, while the ripples depth decreased due to the shielding effect. On the other hand, for burst with fixed intra-bursts delay of 1.5 ps, the spatial period increased with the pulse splitting, while the ripples had nearly the same depth. The trend on the depth was explained in terms of plasma shielding and incubation effect which compete each other. Nonetheless, this study suggested that periodic patterns of nano-ripples distributed over large surface areas can be produced using burst of ultrashort laser pulses and that the spatial period and depth of such surface nanostructures can be tuned by adjusting the burst characteristics. This opens up new possibilities in many application fields where it is crucial to precisely tailor the optical, wettability, adhesion and frictional properties of metal surfaces. This can be done using a robust and flexible burst generator based on birefringent crystals that is very appealing from the industrial point of view.

Finally, the employment of bursts of sub-pulses with circular polarization (CP) or with crossed linear-polarization (XP) enabled the 2D-LIPSS generation, notably triangular-shaped ones with hexagonal arrangement, in a narrow window of laser and process parameters. Fine optimization of the main process parameters, like e.g. accumulated laser fluence and burst features, allowed producing highly ordered and homogeneous 2D triangular LIPSS over an extended textured area both with CP or XP bursts. The wettability of these surfaces was also investigated, revealing a sticky super-hydrophobic behaviour.

In conclusion, the novel approach proposed in this work for fabricating uniform sub-wavelength textures on stainless steel surfaces by using bursts of ultrashort laser pulses, opens new possibilities in many application fields where it is crucial to precisely tailor the optical, wettability, adhesion and frictional properties of metal surfaces. The setup, based on a cheap and flexible burst generator and consisting of an array of birefringent crystals, can be easily adapted to any ultrafast laser source. In principle, it is much more robust and convenient than other setups used for the same purpose, which are less suitable for industrial applications since they are more complicated or based on expensive equipment.

The obtained results in this research work can help to achieve a comprehensive and deeper understanding of the physical mechanisms of the ultrashort laser pulses-material interactions, especially when bursts of fs-pulses with ps delays are employed. Further investigations could be carried out refining the numerical model based on TTM for burst, e.g. by taking into

account changes of the optical properties of the material with a phase close or in the melting region.

It is expected that further studies on burst will help elucidate the fundamental mechanisms of incubation effects on the ablation threshold. These will help forecast the feasibility of using ultrafast laser processing for relatively precise and fast machining while avoiding shielding effects and multi-pulse heat accumulation.

Bibliography

1. E. Mottay, X. Liu, H. Zhang, E. Mazur, R. Sanatinia, and W. Pfleging, "Industrial applications of ultrafast laser processing," *MRS Bull.* **41**(12), 984–992 (2016).
2. M. Müller, M. Kienel, A. Klenke, T. Gottschall, E. Shestaev, M. Plötner, J. Limpert, and A. Tünnermann, "1 kW 1 mJ eight-channel ultrafast fiber laser," *Opt. Lett.* **41**(15), 3439–3442 (2016).
3. R. Jung, J. Tümmler, T. Nubbemeyer, and I. Will, "Thin-disk ring amplifier for high pulse energy," *Opt. Express* **24**(5), 4375–4381 (2016).
4. R. R. Gattass, L. R. Cerami, and E. Mazur, "Micromachining of bulk glass with bursts of femtosecond laser pulses at variable repetition rates," *Opt. Express* **14**(12), 5279–5284 (2006).
5. J. Schille, L. Schneider, S. Kraft, L. Hartwig, and U. Loeschner, "Experimental study on double-pulse laser ablation of steel upon multiple parallel-polarized ultrashort-pulse irradiations," *Appl. Phys. A Mater. Sci. Process.* **122**(7), (2016).
6. M. Sailer, F. Bauer, J. Kleiner, and M. Kaiser, "Scaling of Ablation Rates. Ablation Efficiency and Quality Aspects of Burst- Mode Micromachining of Metals.," *Lasers Manuf. Conf.* 1–8 (2015).
7. B. Neuenschwander, T. Kramer, B. Lauer, and B. Jaeggi, "Burst mode with ps- and fs-pulses: Influence on the removal rate, surface quality, and heat accumulation," *Proc. SPIE - Int. Soc. Opt. Eng.* **9350**, (2015).
8. R. Knappe, H. Haloui, A. Seifert, A. Weis, and A. Nebel, "Scaling ablation rates for picosecond lasers using burst micromachining," in (2010), **7585**, p. 75850H–7585–6.
9. B. N. Chichkov, C. Momma, S. Nolte, F. Alvensleben, and A. Tünnermann, "Applied Physics A = o " ° o Femtosecond , picosecond and nanosecond laser ablation of solids," **115**, 1996 (1996).
10. K. H. Leitz, B. Redlingshöer, Y. Reg, A. Otto, and M. Schmidt, "Metal ablation with short and ultrashort laser pulses," *Phys. Procedia* **12**(PART 2), 230–238 (2011).
11. P. T. Mannion, J. Magee, E. Coyne, G. M. O'Connor, and T. J. Glynn, "The effect of damage accumulation behaviour on ablation thresholds and damage morphology in ultrafast laser micro-machining of common metals in air," *Appl. Surf. Sci.* **233**(1–4), 275–287 (2004).

12. A. Lakhtakia, "Would Brewster recognize today's Brewster angle?," *Opt. News* **15**(6), 14–18 (1989).
13. D. Perez and L. J. Lewis, "Molecular-dynamics study of ablation of solids under femtosecond laser pulses," *Phys. Rev. B - Condens. Matter Mater. Phys.* **67**(18), 1–15 (2003).
14. B. Rethfeld, D. S. Ivanov, M. E. Garcia, and S. I. Anisimov, "Modelling ultrafast laser ablation," *J. Phys. D. Appl. Phys.* **50**(19), 193001 (2017).
15. B. Y. Mueller and B. Rethfeld, "Relaxation dynamics in laser-excited metals under nonequilibrium conditions," *Phys. Rev. B - Condens. Matter Mater. Phys.* **87**(3), 1–12 (2013).
16. P. Balling, "Ultrashort-pulse laser excitation of materials," (July), (2014).
17. M. D. Shirk and P. A. Molian, "A review of ultrashort pulsed laser ablation of materials," *J. Laser Appl.* **10**(1), 18–28 (1998).
18. B. Rethfeld, A. Kaiser, M. Vicanek, and G. Simon, "Ultrafast dynamics of nonequilibrium electrons in metals under femtosecond laser irradiation," *Phys. Rev. B - Condens. Matter Mater. Phys.* **65**(21), 2143031–21430311 (2002).
19. S. Döring Dr. rer.nat., "Analysis of the hole shape evolution in ultrashort pulse laser drilling," (2015).
20. S. I. Anisimov, B. L. Kapeliovich, and T. L. Perel'man, "Electron emission from the metal surfaces induced by ultrashort lasers pulses," *Zhurnal Eksperimental'noj i Teor. Fiz.* **66**(2), 776–781 (1974).
21. Y. Jee, M. F. Becker, and R. M. Walser, "Laser-induced damage on single-crystal metal surfaces," *J. Opt. Soc. Am. B* **5**(3), 648 (1988).
22. R. E. Samad and N. D. Vieira, "Geometrical method for determining the surface damage threshold for femtosecond laser pulses," *Laser Phys.* **16**(2), 336–339 (2006).
23. J. M. Liu, "Simple technique for measurements of pulsed Gaussian-beam spot sizes," *Opt. Lett.* **7**(5), 196 (1982).
24. J. Byskov-Nielsen, J. M. Savolainen, M. S. Christensen, and P. Balling, "Ultra-short pulse laser ablation of metals: Threshold fluence, incubation coefficient and ablation rates," *Appl. Phys. A Mater. Sci. Process.* **101**(1), 97–101 (2010).
25. Z. Sun, M. Lenzner, and W. Rudolph, "Generic incubation law for laser damage and ablation thresholds," *J. Appl. Phys.* **117**(7), (2015).

26. J. Bonse, S. Baudach, J. Krüger, W. Kautek, and M. Lenzner, "Femtosecond laser ablation of silicon-modification thresholds and morphology," *Appl. Phys. A Mater. Sci. Process.* **74**(1), 19–25 (2002).
27. S. Baudach, J. Bonse, J. Krüger, and W. Kautek, "Ultrashort pulse laser ablation of polycarbonate and polymethylmethacrylate," *Appl. Surf. Sci.* **154**, 555–560 (2000).
28. D. Gómez and I. Goenaga, "On the incubation effect on two thermoplastics when irradiated with ultrashort laser pulses: Broadening effects when machining microchannels," *Appl. Surf. Sci.* **253**(4), 2230–2236 (2006).
29. L. M. Machado, R. E. Samad, W. de Rossi, and N. D. V. Junior, "D-Scan measurement of ablation threshold incubation effects for ultrashort laser pulses," *Opt. Express* **20**(4), 4114 (2012).
30. B. Neuenschwander, B. Jaeggi, M. Schmid, A. Dommann, A. Neels, T. Bandi, and G. Hennig, "Factors controlling the incubation in the application of ps laser pulses on copper and iron surfaces," **8607**, 86070D (2013).
31. F. Di Niso, C. Gaudiuso, T. Sibillano, F. P. Mezzapesa, A. Ancona, and P. M. Lugarà, "Role of heat accumulation on the incubation effect in multi-shot laser ablation of stainless steel at high repetition rates," *Opt. Express* **22**(10), 12200 (2014).
32. D. Ashkenasi, M. Lorenz, R. Stoian, and A. Rosenfeld, "Surface damage threshold and structuring of dielectrics using femtosecond laser pulses: the role of incubation," *Appl. Surf. Sci.* **150**(1), 101–106 (1999).
33. W. Hu, Y. C. Shin, and G. King, "Modeling of multi-burst mode pico-second laser ablation for improved material removal rate," *Appl. Phys. A* **98**(2), 407 (2009).
34. O. Andrusyak, M. Bubelnik, J. Mares, T. A. McGovern, and C. W. Siders, "Single-pulse and burst-mode ablation of gold films measured by quartz crystal microbalance," *Laser-Induced Damage Opt. Mater.* 2004 **5647**(1), 61–71 (2005).
35. B. Dromey, M. Zepf, M. Landreman, K. O'keeffe, T. Robinson, and S. M. Hooker, "Generation of a train of ultrashort pulses from a compact birefringent crystal array.," *Appl. Opt.* **46**(22), 5142–5146 (2007).
36. S. Zhou, D. Ouzounov, H. Li, I. Bazarov, B. Dunham, C. Sinclair, and F. W. Wise, "Efficient temporal shaping of ultrashort pulses with birefringent crystals," *Appl. Opt.* **46**(35), 8488–8492 (2007).

37. A. Semerok and C. Dutouquet, "Ultrashort double pulse laser ablation of metals," *Thin Solid Films* **453–454**, 501–505 (2004).
38. E. Axente, I. N. Mihailescu, J. Hermann, and T. E. Itina, "Probing electron-phonon coupling in metals via observations of ablation plumes produced by two delayed short laser pulses," *Appl. Phys. Lett.* **99**(8), (2011).
39. S. Noël and J. Hermann, "Reducing nanoparticles in metal ablation plumes produced by two delayed short laser pulses," *Appl. Phys. Lett.* **94**(5), 25–28 (2009).
40. M. E. Povarnitsyn, T. E. Itina, P. R. Levashov, and K. V. Khishchenko, "Simulation of ultrashort double-pulse laser ablation," *Appl. Surf. Sci.* **257**(12), 5168–5171 (2011).
41. M. E. Povarnitsyn, V. B. Fokin, P. R. Levashov, and T. E. Itina, "Molecular dynamics simulation of subpicosecond double-pulse laser ablation of metals," *Phys. Rev. B - Condens. Matter Mater. Phys.* **92**(17), 1–10 (2015).
42. J. Mildner, C. Sarpe, N. Götte, M. Wollenhaupt, and T. Baumert, "Emission signal enhancement of laser ablation of metals (aluminum and titanium) by time delayed femtosecond double pulses from femtoseconds to nanoseconds," *Appl. Surf. Sci.* **302**, 291–298 (2014).
43. K. Pangovski, M. Sparkes, and W. O'Neill, "A holographic method for optimisation of laser-based production processes," *Adv. Opt. Technol.* **5**(2), 129–136 (2016).
44. A. Ancona, F. Röser, K. Rademaker, J. Limpert, S. Nolte, and A. Tünnermann, "High speed laser drilling of metals using a high repetition rate, high average power ultrafast fiber CPA system," *Opt. Express* **16**(12), 8958–8968 (2008).
45. C. Kerse, H. Kalaycıoğlu, P. Elahi, B. Çetin, D. K. Kesim, Ö. Akçaalan, S. Yavaş, M. D. Aşık, B. Öktem, H. Hoogland, R. Holzwarth, and F. Ö. Ilday, "Ablation-cooled material removal with ultrafast bursts of pulses," *Nature* **537**(7618), 84–88 (2016).
46. D. J. Förster, S. Faas, S. Gröninger, F. Bauer, A. Michalowski, R. Weber, and T. Graf, "Shielding effects and re-deposition of material during processing of metals with bursts of ultra-short laser pulses," *Appl. Surf. Sci.* **440**, 926–931 (2018).
47. Y. Zhang, *Modeling of Ultrafast Phase Change Processes in a Thin Metal Film Irradiated by Femtosecond Laser Pulse Trains* (2011), **133**.

48. K. M. Tanvir Ahmmed, C. Grambow, and A. M. Kietzig, "Fabrication of micro/nano structures on metals by femtosecond laser micromachining," *Micromachines* **5**(4), 1219–1253 (2014).
49. J. Bonse, S. Höhm, S. V. Kirner, A. Rosenfeld, and J. Krüger, "Laser-induced periodic surface structures – a scientific evergreen," *IEEE J. Sel. Top. Quantum Electron.* **23**(3), 9000615 (2017).
50. M. Birnbaum, "Semiconductor surface damage produced by Ruby lasers," *J. Appl. Phys.* **36**(11), 3688–3689 (1965).
51. A. Y. Vorobyev and C. Guo, "Metal colorization with femtosecond laser pulses," **041914**(2008), 70051T (2008).
52. Z. Fang, Y. Zhao, and J. Shao, "Femtosecond laser-induced periodic surface structure on fused silica surface," *Optik (Stuttg.)* **127**(3), 1171–1175 (2016).
53. E. Skoulas, A. Manousaki, C. Fotakis, and E. Stratakis, "Biomimetic surface structuring using cylindrical vector femtosecond laser beams," *Sci. Rep.* **7**(March), 1–11 (2017).
54. A. M. Bonch-Bruevich, M. N. Libenson, and V. S. Makin, "Surface electromagnetic waves in optics," *Opt. Eng.* **31**(4), 718–725 (1992).
55. G. Li, J. Li, Y. Hu, C. Zhang, X. Li, J. Chu, and W. Huang, "Femtosecond laser color marking stainless steel surface with different wavelengths," *Appl. Phys. A Mater. Sci. Process.* **118**(4), 1189–1196 (2014).
56. J. E. Sipe, J. F. Young, and J. S. Preston, "Laser-induced periodic surface structure I. Theory," *Phys. Rev. B* **27**(2), (1983).
57. P. Nürnberger, H. Reinhardt, H. C. Kim, F. Yang, K. Peppler, J. Janek, and N. Hampp, "Influence of substrate microcrystallinity on the orientation of laser-induced periodic surface structures," *J. Appl. Phys.* **118**(13), (2015).
58. T. Y. Hwang and C. Guo, "Femtosecond laser-induced blazed periodic grooves on metals," *Opt. Lett.* **36**(13), 2575 (2011).
59. J. Bonse, S. Höhm, A. Rosenfeld, and J. Krüger, "Sub-100-nm laser-induced periodic surface structures upon irradiation of titanium by Ti:sapphire femtosecond laser pulses in air," *Appl. Phys. A Mater. Sci. Process.* **110**(3), 547–551 (2013).
60. K. Okamuro, M. Hashida, Y. Miyasaka, Y. Ikuta, S. Tokita, and S. Sakabe, "Laser fluence dependence of periodic grating structures formed on metal surfaces under femtosecond laser pulse irradiation,"

- Phys. Rev. B - Condens. Matter Mater. Phys. **82**(16), 1–5 (2010).
61. S. Sakabe, M. Hashida, S. Tokita, S. Namba, and K. Okamuro, "Mechanism for self-formation of periodic grating structures on a metal surface by a femtosecond laser pulse," Phys. Rev. B - Condens. Matter Mater. Phys. **79**(3), 1–4 (2009).
 62. Q. Z. Zhao, S. Malzer, and L. J. Wang, "Formation of subwavelength periodic structures on tungsten induced by ultrashort laser pulses," Opt. Lett. **32**(13), 1932 (2007).
 63. A. Y. Vorobyev and C. Guo, "Femtosecond Laser-Induced Periodic Surface Structures on Tungsten," in *Conference on Lasers and Electro-Optics/International Quantum Electronics Conference* (Optical Society of America, 2009), p. CThEE6.
 64. A. Y. Vorobyev, V. S. Makin, and C. Guo, "Periodic ordering of random surface nanostructures induced by femtosecond laser pulses on metals," J. Appl. Phys. **101**(3), (2007).
 65. U. Hermens, S. V. Kirner, C. Emonts, P. Comanns, E. Skoulas, A. Mimidis, H. Mescheder, K. Winands, J. Krüger, E. Stratakis, and J. Bonse, "Mimicking lizard-like surface structures upon ultrashort laser pulse irradiation of inorganic materials," Appl. Surf. Sci. **418**, 499–507 (2017).
 66. S. Hou, Y. Huo, P. Xiong, Y. Zhang, S. Zhang, T. Jia, Z. Sun, J. Qiu, and Z. Xu, "Formation of long- and short-periodic nanoripples on stainless steel irradiated by femtosecond laser pulses," J. Phys. D. Appl. Phys. **44**(50), (2011).
 67. L. Qi, K. Nishii, and Y. Namba, "Regular subwavelength surface structures induced by femtosecond laser pulses on stainless steel.," Opt. Lett. **34**(12), 1846–8 (2009).
 68. Y. C. Guan, W. Zhou, Z. L. Li, and H. Y. Zheng, "Femtosecond laser-induced iridescent effect on AZ31B magnesium alloy surface," J. Phys. D. Appl. Phys. **46**(42), 425305 (2013).
 69. G. R. B. E. Römer, A. J. Huis in't Veld, J. Meijer, and M. N. W. Groenendijk, "On the formation of laser induced self-organizing nanostructures," CIRP Ann. - Manuf. Technol. **58**(1), 201–204 (2009).
 70. X. Sedao, C. Maurice, F. Garrelie, J. P. Colombier, S. Reynaud, R. Quey, and F. Pigeon, "Influence of crystal orientation on the formation of femtosecond laser-induced periodic surface structures and lattice defects accumulation," Appl. Phys. Lett. **104**(17), (2014).
 71. P. Gregorčič, M. Sedlaček, B. Podgornik, and J. Reif, "Formation of

- laser-induced periodic surface structures (LIPSS) on tool steel by multiple picosecond laser pulses of different polarizations," *Appl. Surf. Sci.* **387**, 698–706 (2016).
72. M. Hashida, T. Nishii, Y. Miyasaka, H. Sakagami, M. Shimizu, S. Inoue, and S. Sakabe, "Orientation of periodic grating structures controlled by double-pulse irradiation," *Appl. Phys. A Mater. Sci. Process.* **122**(4), 1–5 (2016).
 73. D. Breitling, A. Ruf, and F. Dausinger, "Fundamental aspects in machining of metals with short and ultrashort laser pulses," **5339**, 49 (2004).
 74. Y. Furukawa, R. Sakata, K. Konishi, K. Ono, S. Matsuoka, K. Watanabe, S. Inoue, M. Hashida, and S. Sakabe, "Demonstration of periodic nanostructure formation with less ablation by double-pulse laser irradiation on titanium," *Appl. Phys. Lett.* **108**(26), 1–5 (2016).
 75. F. Fraggelakis, E. Stratakis, and P. A. Loukakos, "Control of periodic surface structures on silicon by combined temporal and polarization shaping of femtosecond laser pulses," *Appl. Surf. Sci.* **444**, 154–160 (2018).
 76. G. D. Tsibidis, E. Stratakis, P. A. Loukakos, and C. Fotakis, "Controlled ultrashort-pulse laser-induced ripple formation on semiconductors," *Appl. Phys. A Mater. Sci. Process.* **114**(1), 57–68 (2014).
 77. A. Rosenfeld, M. Rohloff, S. Höhm, J. Krüger, and J. Bonse, "Formation of laser-induced periodic surface structures on fused silica upon multiple parallel polarized double-femtosecond-laser-pulse irradiation sequences," *Appl. Surf. Sci.* **258**(23), 9233–9236 (2012).
 78. J. JJ Nivas, F. Gesuele, E. Allahyari, S. L. Oscurato, R. Fittipaldi, A. Vecchione, R. Bruzzese, and S. Amoroso, "Effects of ambient air pressure on surface structures produced by ultrashort laser pulse irradiation," *Opt. Lett.* **42**(14), 2710 (2017).
 79. J. Bonse, A. Rosenfeld, and J. Krüger, "On the role of surface plasmon polaritons in the formation of laser-induced periodic surface structures upon irradiation of silicon by femtosecond-laser pulses," *J. Appl. Phys.* **106**(10), (2009).
 80. D. Dufft, A. Rosenfeld, S. K. Das, R. Grunwald, and J. Bonse, "Femtosecond laser-induced periodic surface structures revisited: A comparative study on ZnO," *J. Appl. Phys.* **105**(3), (2009).
 81. A. Borowiec and H. K. Haugen, "Subwavelength ripple formation on

- the surfaces of compound semiconductors irradiated with femtosecond laser pulses," *Appl. Phys. Lett.* **82**(25), 4462–4464 (2003).
82. J. Reif, O. Varlamova, S. Varlamov, and M. Bestehorn, "The role of asymmetric excitation in self-organized nanostructure formation upon femtosecond laser ablation," *AIP Conf. Proc.* **1464**, 428–441 (2012).
 83. X. Sedao, A. Abou Saleh, A. Rudenko, T. Douillard, C. Esnouf, S. Reynaud, C. Maurice, F. Pigeon, F. Garrelie, and J. P. Colombier, "Self-Arranged Periodic Nanovoids by Ultrafast Laser-Induced Near-Field Enhancement," *ACS Photonics* **5**(4), 1418–1426 (2018).
 84. J. F. Sipe, J. E.; van Driel, H. M.; Young, "Surface electrodynamics: radiation fields, surface polaritons, and radiation remnants," *Can. J. Phys.* **63**(1), 104 (1985).
 85. H. Zhanghua and S. Bozhevolnyi, *Plasmonic, Nanoguides and Circuits* (2009).
 86. Z. Han and S. I. Bozhevolnyi, "Waveguiding with surface plasmon polaritons," *Handb. Surf. Sci.* **4**, 137–187 (2014).
 87. I. Gnilitzki, T. J. Y. Derrien, Y. Levy, N. M. Bulgakova, T. Mocek, and L. Orazi, "High-speed manufacturing of highly regular femtosecond laser-induced periodic surface structures: Physical origin of regularity," *Sci. Rep.* **7**(1), 1–11 (2017).
 88. H. L. Lord, W. Zhan, and J. Pawliszyn, *Fundamentals and Applications* (2010), **677**(1).
 89. A. V Zayats, I. I. Smolyaninov, and A. A. Maradudin, "Nano-optics of surface plasmon polaritons," *Phys. Rep.* **408**(3), 131–314 (2005).
 90. O. Varlamova, J. Reif, S. Varlamov, and M. Bestehorn, "Chapter 1 Self-organized Surface Patterns Originating from Laser-Induced Instability," 3–30 (2015).
 91. S. Maragkaki, "Control of period and orientation of laser-induced ripples," Ruhr-Universität Bochum, Universitätsbibliothek (2018).
 92. G. D. Tsibidis, M. Barberoglou, P. A. Loukakos, E. Stratakis, and C. Fotakis, "Dynamics of ripple formation on silicon surfaces by ultrashort laser pulses in subablation conditions," *Phys. Rev. B - Condens. Matter Mater. Phys.* **86**(11), 1–14 (2012).
 93. E. L. Gurevich, "Mechanisms of femtosecond LIPSS formation induced by periodic surface temperature modulation," *Appl. Surf. Sci.* **374**, 56–60 (2016).
 94. Garrett Birkhoff, *Hydrodynamics*, second edi (2015).

95. J. Liu, T. Jia, K. Zhou, D. Feng, S. Zhang, H. Zhang, X. Jia, Z. Sun, and J. Qiu, "Direct writing of 150 nm gratings and squares on ZnO crystal in water by using 800 nm femtosecond laser," *Opt. Express* **22**(26), 32361 (2014).
96. M. Huang, F. L. Zhao, T. Q. Jia, Y. Cheng, N. S. Xu, and Z. Z. Xu, "A uniform 290 nm periodic square structure on ZnO fabricated by two-beam femtosecond laser ablation," *Nanotechnology* **18**(50), (2007).
97. J. Ouyang, W. Perrie, O. J. Allegre, T. Heil, Y. Jin, E. Fearon, D. Eckford, S. P. Edwardson, and G. Dearden, "Tailored optical vector fields for ultrashort-pulse laser induced complex surface plasmon structuring," *Opt. Express* **23**(10), 12562 (2015).
98. J. J. J. Nivas, S. He, A. Rubano, A. Vecchione, D. Paparo, L. Marrucci, R. Bruzzese, and S. Amoruso, "Direct Femtosecond Laser Surface Structuring with Optical Vortex Beams Generated by a q-plate," *Sci. Rep.* **5**(December), 1–12 (2015).
99. J. M. Romano, A. Garcia-Giron, P. Penchev, and S. Dimov, "Triangular laser-induced submicron textures for functionalising stainless steel surfaces," *Appl. Surf. Sci.* **440**, 162–169 (2018).
100. F. Fraggelakis, G. Mincuzzi, J. Lopez, I. Manek-Hönniger, and R. Kling, "2D laser induced periodic surface structures with double cross-polarized pulses," in (2018), **10520**, p. 105200L–10520–8.
101. F. Fraggelakis, G. Mincuzzi, J. Lopez, I. Manek-Hönniger, and R. Kling, "Controlling micron and submicron scale laser induced surface structures on stainless steel with industrial femtosecond lasers," (Accepted Publ. in) *J. Laser Micro / Nanoeng.* Oct. (2018).
102. Q. Liu, N. Zhang, J. Yang, H. Qiao, and C. Guo, "Direct fabricating large-area nanotriangle structure arrays on tungsten surface by nonlinear lithography of two femtosecond laser beams," *Opt. Express* **26**(9), 11718–11727 (2018).
103. R. S. Graves, T. G. Kollie, D. L. McElroy, and K. E. Gilchrist, "The thermal conductivity of AISI 304L stainless steel," *Int. J. Thermophys.* **12**(2), 409–415 (1991).
104. M. Spittel and T. Spittel, *Advanced Materials and Technologies Volume 2 Materials Subvolume C Metal Forming Data* (2009).
105. E. Bévilion, J. P. Colombier, B. Dutta, and R. Stoian, "Ab Initio Nonequilibrium Thermodynamic and Transport Properties of Ultrafast Laser Irradiated 316L Stainless Steel," *J. Phys. Chem. C* **119**(21), 11438–11446 (2015).

106. K. Salonitis, A. Stournaras, G. Tsoukantas, P. Stavropoulos, and G. Chryssolouris, "A theoretical and experimental investigation on limitations of pulsed laser drilling," *J. Mater. Process. Technol.* **183**(1), 96–103 (2007).
107. R. Le Harzic, D. Breitling, M. Weikert, S. Sommer, C. Föhl, S. Valette, C. Donnet, E. Audouard, and F. Dausinger, "Pulse width and energy influence on laser micromachining of metals in a range of 100 fs to 5 ps," *Appl. Surf. Sci.* **249**(1–4), 322–331 (2005).
108. S. Backus, C. G. Durfee, M. M. Murnane, and H. C. Kapteyn, "High power ultrafast lasers," *Rev. Sci. Instrum.* **69**(3), 1207–1223 (1998).
109. F. Röser, T. Eidam, J. Rothhardt, O. Schmidt, D. N. Schimpf, J. Limpert, and A. Tünnermann, "Millijoule pulse energy high repetition rate femtosecond fiber chirped-pulse amplification system.pdf," **32**(24), 3495–3497 (2007).
110. D. Nodop, J. Limpert, R. Hohmuth, W. Richter, M. Guina, and A. Tünnermann, "High-pulse-energy passively Q-switched quasi-monolithic microchip lasers operating in the sub-100-ps pulse regime," *Opt. Lett.* **32**(15), 2115–7 (2007).
111. S. Nolte, C. Momma, G. Kamlage, A. Ostendorf, C. Fallnich, F. Von Alvensleben, and H. Welling, "Polarization effects in ultrashort-pulse laser drilling," *Appl. Phys. A Mater. Sci. Process.* **68**(5), 563–567 (1999).
112. P. Tournois, "Acousto-optic programmable dispersive filter for adaptive compensation of group delay time dispersion in laser systems," *Opt. Commun.* **140**(4–6), 245–249 (1997).
113. Demtröder Wolfgang, *Laser Spectroscopy, Vol. 1: Basic Principles* (2008).
114. J. Limpert, F. Röser, D. N. Schimpf, E. Seise, T. Eidam, S. Hdrich, J. Rothhardt, C. J. Misas, and A. Tünnermann, "High repetition rate gigawatt peak power fiber laser systems: Challenges, design, and experiment," *IEEE J. Sel. Top. Quantum Electron.* **15**(1), 159–169 (2009).
115. J. R. Davis, *Metals Handbook*, Desk editi (ASM International, 1998).
116. L. C. Tshabalala and S. Pityana, "Surface texturing of Si₃N₄-SiC ceramic tool components by pulsed laser machining," *Surf. Coatings Technol.* **289**, 52–60 (2016).
117. H. D. Vora and N. B. Dahotre, "Surface topography in three-dimensional laser machining of structural alumina," *J. Manuf. Process.*

- 19**, 49–58 (2015).
118. F. Fraggelakis, G. Mincuzzi, J. Lopez, I. Manek-Hönniger, and R. Kling, "Texturing metal surface with MHz ultra-short laser pulses," *Opt. Express* **25**(15), 18131 (2017).
 119. F. Schelle, S. Polz, H. Haloui, A. Braun, C. Dehn, M. Frentzen, and J. Meister, "Ultrashort pulsed laser (USPL) application in dentistry: basic investigations of ablation rates and thresholds on oral hard tissue and restorative materials," *Lasers Med. Sci.* **29**(6), 1775–1783 (2014).
 120. F. Palumbo and R. Di Mundo, *Wettability: Significance and Measurement* (2014).
 121. C. Gaudio, G. Giannuzzi, A. Volpe, P. M. Lugarà, I. Choquet, and A. Ancona, "Incubation during laser ablation with bursts of femtosecond pulses with picosecond delays," *Opt. Express* **26**(4), 3801 (2018).
 122. A. Ruiz de la Cruz, R. Lahoz, J. Siegel, G. F. de la Fuente, and J. Solis, "High speed inscription of uniform, large-area laser-induced periodic surface structures in Cr films using a high repetition rate fs laser," *Opt. Lett.* **39**(8), 2491 (2014).
 123. G. Giannuzzi, C. Gaudio, C. Di Franco, G. Scamarcio, P. M. Lugarà, and A. Ancona, "Large area laser-induced periodic surface structures on steel by bursts of femtosecond pulses with picosecond delays," *Opt. Lasers Eng.* **114**, 15–21 (2019).
 124. M. E. Povarnitsyn, T. E. Itina, K. V. Khishchenko, and P. R. Levashov, "Suppression of ablation in femtosecond double-pulse experiments," *Phys. Rev. Lett.* **103**(19), (2009).
 125. Y. Rong, P. Ji, M. He, Y. Zhang, and Y. Tang, "Multiscale Investigation of Femtosecond Laser Pulses Processing Aluminum in Burst Mode," *Nanoscale Microscale Thermophys. Eng.* **00**(00), 1–24 (2018).
 126. M. Huang, F. Zhao, Y. Cheng, N. Xu, and Z. Xu, "Origin of laser-induced near-subwavelength ripples: Interference between surface plasmons and incident laser," *ACS Nano* **3**(12), 4062–4070 (2009).
 127. L. Jiang, W. Han, X. Li, Q. Wang, F. Meng, and Y. Lu, "Crystal orientation dependence of femtosecond laser-induced periodic surface structure on (100) silicon," *Opt. Lett.* **39**(11), 3114–7 (2014).
 128. M. Martínez-Calderon, A. Rodríguez, A. Dias-Ponte, M. C. Morant-Miñana, M. Gómez-Aranzadi, and S. M. Olaizola, "Femtosecond laser manufacturing of highly hydrophobic hierarchical structures fabricated

- by combining surface microstructures and LIPSS," *Appl. Surf. Sci.* **374**, 81–89 (2016).
129. L. Gemini, M. Faucon, L. Romoli, and R. Kling, "High throughput laser texturing of super-hydrophobic surfaces on steel," **10092**, 100921G (2017).
 130. E. Rebollar, I. Frischauf, M. Olbrich, T. Peterbauer, S. Hering, J. Preiner, P. Hinterdorfer, C. Romanin, and J. Heitz, "Proliferation of aligned mammalian cells on laser-nanostructured polystyrene," *Biomaterials* **29**(12), 1796–1806 (2008).
 131. M. Martínez-Calderon, M. Manso-Silván, A. Rodríguez, M. Gómez-Aranzadi, J. P. García-Ruiz, S. M. Olaizola, and R. J. Martín-Palma, "Surface micro- and nano-texturing of stainless steel by femtosecond laser for the control of cell migration," *Sci. Rep.* **6**(July), 1–10 (2016).
 132. Z. Wang, Q. Zhao, and C. Wang, "Reduction of friction of metals using laser-induced periodic surface nanostructures," *Micromachines* **6**(11), 1606–1616 (2015).
 133. Z. Ou, M. Huang, and F. Zhao, "The fluence threshold of femtosecond laser blackening of metals: The effect of laser-induced ripples," *Opt. Laser Technol.* **79**, 79–87 (2016).
 134. X. Dai, B. B. Stogin, S. Yang, and T. S. Wong, "Slippery Wenzel State," *ACS Nano* **9**(9), 9260–9267 (2015).
 135. P. Bizi-bandoki, S. Valette, E. Audouard, and S. Benayoun, "Applied Surface Science Time dependency of the hydrophilicity and hydrophobicity of metallic alloys subjected to femtosecond laser irradiations," *Appl. Surf. Sci.* **273**, 399–407 (2013).
 136. Y. Zhang, G. Zou, L. Liu, Y. Zhao, Q. Liang, A. Wu, and Y. N. Zhou, "Applied Surface Science Time-dependent wettability of nano-patterned surfaces fabricated by femtosecond laser with high efficiency," *Appl. Surf. Sci.* **389**, 554–559 (2016).
 137. J. T. Cardoso, A. Garcia-Girón, J. M. Romano, D. Huerta-Murillo, R. Jagdheesh, M. Walker, S. S. Dimov, and J. L. Ocaña, "Influence of ambient conditions on the evolution of wettability properties of an IR-, ns-laser textured aluminium alloy," *RSC Adv.* **7**(63), 39617–39627 (2017).
 138. A. Kietzig, S. G. Hatzikiriakos, and P. Englezos, "Patterned Superhydrophobic Metallic Surfaces," **25**(30), 4821–4827 (2009).
 139. A. Kietzig and M. N. Mirvakili, "Journal of Adhesion Science and Laser-Patterned Super- Hydrophobic Pure Metallic Substrates : Cassie

- to Wenzel Wetting Transitions," (July 2013), 2789–2809 (2012).
140. N. Yasumaru, E. Sentoku, and J. Kiuchi, "Formation of organic layer on femtosecond laser-induced periodic surface structures," *Appl. Surf. Sci.* **405**, 267–272 (2017).
 141. A. M. Kietzig, M. N. Mirvakili, S. Kamal, P. Englezos, and S. G. Hatzikiriakos, "Laser-patterned super-hydrophobic pure metallic substrates: Cassie to Wenzel wetting transitions," *J. Adhes. Sci. Technol.* **25**(20), 2789–2809 (2012).

Publications and conferences attendance

Publications

G. Giannuzzi, C. Gaudio, C. Di Franco, G. Scamarcio, P. M. Lugarà and A. Ancona, “Large area laser-induced periodic surface structures on steel by bursts of femtosecond pulses with picosecond delays”, *Opt Lasers Eng*, vol. 114, p. 15–21 (2019)

C. Gaudio, G. Giannuzzi, A. Volpe, P. M. Lugarà, I. Choquet and A. Ancona, “Incubation during laser ablation with bursts of femtosecond pulses with picosecond delays”, *Opt. Express*, vol. 26, p. 3801 (2018)

“High versatile LIPSS generation on stainless steel with bursts of ultrashort pulses”, under preparation

“Double-pulse femtosecond laser setup for sub-wavelength two-dimensional LIPSS on large area stainless steel surfaces”, under preparation

Proceeding

G. Giannuzzi, F. Fraggelakis, C. Gaudio, C. Di Franco, G. Scamarcio, G. Mincuzzi, R. Kling, A. Ancona “Surface texturing of steel with bursts of femtosecond laser pulses”, *LPM2018* (2018)

C. Gaudio, G. Giannuzzi, I. Choquet, P. M. Lugarà, A. Ancona, “Incubation effect in burst mode fs-laser ablation of stainless steel samples”, *Proc. SPIE 10520* (2018)

Conferences and schools

International School - “Laser Micro/Nanostructuring and Surface Tribology”, Bari, 1-5 October 2018 (contribution: talk)

LPM 2018 – “Laser precision microfabrication”, 19th International Symposium on Laser Precision Microfabrication, Edinburgh, 25-28 June 2018 (contribution: talk)

LiM 2017 - Lasers in Manufacturing, 26-29 giugno, 2017, Monaco di Baviera - Germany (contribution: talk)

IFN-DAY 2017, Istituto di Fotonica e Nanotecnologia, 10-11 gennaio, 2017,
Bari (contribution: poster)

Awards

Outstanding student's oral presentation award – 19th International Symposium on Laser Precision Microfabrication, LPM2018, 25-28 June 2018, Edinburgh, UK, “Surface texturing of steel with bursts of femtosecond laser pulses”

Acknowledgements

I would like to thank:

- my tutor Dr. Antonio Ancona for the supervision during the years of my PhD;
- the research group for the team working;
- Prof. G. Scamarcio and Dr. C. Di Franco of IFN-CNR in Bari for providing the AFM measurements of 1D-LIPSS;
- Dr. F. Fraggelakis of ALPhANOV Technological Centre, Talence, France for useful collaboration;
- Dr. R. Di Mundo of Bari Polytech for support in wettability measurements;
- Prof. I. Choquet of Univ. West, Sweden, for supporting in TTM code;
- Dr. G. Pecastaings of Univ. Bordeaux, France, for providing the AFM measurements of 2D-LIPSS;
- Tecno Acciai S.r.l. for the provision of the high quality steel samples;
- ENEA research centre for providing the XPS measurements;
- IFN-CNR in Bari for use of laboratories and facilities;